UC Berkeley
UC Berkeley Electronic Theses and Dissertations

Title
Pressure-Driven Wrinkling of Supported Elastic Tubes

Permalink
https://escholarship.org/uc/item/5gs821fd

Author
Foster, Benjamin Lee

Publication Date
2023

Supplemental Material
https://escholarship.org/uc/item/5gs821fd#supplemental

Peer reviewed|Thesis/dissertation

Pressure-Driven Wrinkling of Supported Elastic Tubes

By

Benjamin Lee Foster

A dissertation submitted in partial satisfaction of the

requirements for the degree of

Doctor of Philosophy

in

Physics

in the

Graduate Division

of the

University of California, Berkeley

Committee in charge:

Professor Edgar Knobloch, Chair
Professor Jonathan Wurtele
Professor Stephen Morris

Summer 2023

Pressure-Driven Wrinkling of Supported Elastic Tubes

Abstract

Pressure-Driven Wrinkling of Supported Elastic Tubes

by

Benjamin Lee Foster

Doctor of Philosophy in Physics

University of California, Berkeley

Professor Edgar Knobloch, Chair

Closed circular elastica under external forcing deform into a wide variety of patterned and localized states, with different physical systems producing strikingly similar shapes. To explore this phenomenon, in this dissertation, a closed elastic membrane subject to an imposed pressure difference between its interior and exterior and coupled to either solid or liquid substrate supports is considered, and a simple governing equation is derived. Specifically, a system in which the substrate is a soft, elastic material with a preferred natural extension is considered and a system where the membrane surrounds and is surrounded by fluids of different densities in a rotating Hele-Shaw cell is considered. In the former system, intended to provide a model of a cross-section of biological arteries, the membrane is taken to be inextensible, while in the latter system the membrane is separately considered in the inextensible and highly extensible limits. In both systems, although the physical interpretations and viable parameter values differ, the resulting governing equation is the same or similar.

A natural length scale is identified from system parameters, and the ratio of system scale to this natural length scale is identified as a key parameter found to set the onset order of primary wrinkle branch bifurcations from the unperturbed circle state as well as the secondary bifurcation onset and solution form. The results of this thesis explain how the wrinkle wavelength is selected as a function of the parameters in compressed wrinkling systems and show how localized folds and mixed mode states form in secondary bifurcations from wrinkled states. In the case of a solid substrate, this key parameter expresses the balance of membrane bending modulus, substrate stiffness, and system scale. In the case of a fluid substrate, the key parameter is a function of the difference in fluid densities, the rotation rate, and the system scale.

Steady state solutions are obtained via asymptotic expansions, numerical continua-

tion, and other analytical and numerical approaches, all with good mutual agreement. Numerical continuation is applied to organize solutions in bifurcation diagrams using system-response metrics such as the baseline tension, compression, energy, or maximum curvature, all as a function of the pressure difference. Solutions are found to come in the classes of wrinkling or buckling primary states with a single wavenumber, mixed mode secondary solutions with two wavenumbers, and folding secondary solutions. This discussion is primarily focused on the solution subset of reflection symmetric states but is augmented by a brief study of symmetry-broken chiral states, computed using numerical continuation and shooting and identified as secondary states.

The governing equation is found to be part of a family of exactly solvable equations describing the wrinkling response of a membrane subject to a variety of substrate forces. The resulting wrinkle profiles are shown to be related to the buckled states of an unsupported ring and are therefore universal. Closed analytical expressions for the resulting universal shapes are provided, including the one-to-one relations between the pressure and tension at which these emerge. The relationship between wrinkling states which have nontrivial onset ordering and buckling states which occur in the absence of a substrate and destabilize monotonically is explored and explained, a previously poorly understood connection.

Finally, the stability of the system is considered from a global energy based perspective and a local temporal linear stability analysis.

Contents

List of Figures

iv

List of Tables

Acknowledgments

I would like to thank my advisor Professor Edgar Knobloch. I have learned a great deal from Edgar about the process of doing good, careful scientific research as well as the process of communicating the results and teaching. He has been an excellent advisor, and I feel very fortunate to have consistently received such detailed, thoughtful, and helpful feedback from him. I am deeply grateful for his guidance during my time at Berkeley.

I would also like to acknowledge Doctor Nicolás Verschueren van Rees and Professor Leonardo Gordillo, coauthors on two of the papers we published. I learned a great deal from both of them and enjoyed collaborating with them very much. I am particularly grateful to Nicolás for his didactic approach to collaboration and his enthusiasm for diving into the details of challenging problems.

I am additionally grateful to the members of the Knobloch Group: Doctors Chang Liu and Adrian van Kan and undergraduates Mathi Raja and Troy Tsubota. I enjoyed collaborating on separate projects with them all very much.

I would also like to thank my teachers over the years for everything they taught me. I would particularly like to thank the members of my thesis committee, Professors Edgar Knobloch, Jonathan Wurtele, and Stephen Morris, for their thoughtful feedback on this work.

I would like to thank my friend and colleague Jaewon Kim for always having time to chat over lunch, tea, or a walk. I am very grateful.

Lastly, I would like to thank my family.

Chapter 1

Introduction

The wrinkling of elastic materials in response to applied force occurs across a rich array of systems in physics and biology. While the study of this phenomenon has roots hundreds of years ago [2, 3, 4], many features remain to be explored today. One has only to look at the human body to see the rich zoo of complicating aspects of wrinkling: wrinkling membranes may possess varying properties such as flexibility or intrinsic shape, be stretched across structures of spatially or temporally varying curvature, be coupled to materials with varying properties such as stiffness or size, or be subjected to varying forms of external forces. In the human body, wrinkling occurs in the skin [5], ocular surfaces [6, 7], gastrointestinal tract [8, 9], esophagus and broader airways [9, 10, 11, 12], and arteries [13]. Several of these examples are shown in Fig. 1.1. These forms of wrinkling may be quasistatic or time-dependent processes.

Beyond the human body, in geometrically simpler flat systems, wrinkling occurs in beams [14], biofilms [15], bunched carpets [16, 17], vertically loaded floating sheets [18, 19, 20], or, a particularly elegant wrinkling testbed, laterally compressed floating thin sheets [21, 22, 23]. In this latter example, the wavelength with which the sheet wrinkles results from a competition between elastic forces and the restoring weight of the entrained liquid. Beyond wrinkles, spatially localized states may set in upon parameter variation. For example, further compression of the floating sheet can cause the sheet to transition from a wrinkled state to one characterised by a single fold, shown in Fig. 1.2(a) [24]. This system demonstrates both time-independent global periodic solutions and spatially localized solutions depending on the choice of external parameters, common features of the systems we will focus on in this thesis.

Wrinkling can also occur in higher dimensions; for example two-dimensional circular and three-dimensional spherical geometries display wrinkling responses. Specific examples including laterally compressed [25] or curved bilayer materials [26], growing or decaying produce [5, 27], three-dimensional deformations of water droplets under rotation [28], and the wrinkling and puckering of spring-loaded growing interfaces [29, 30].
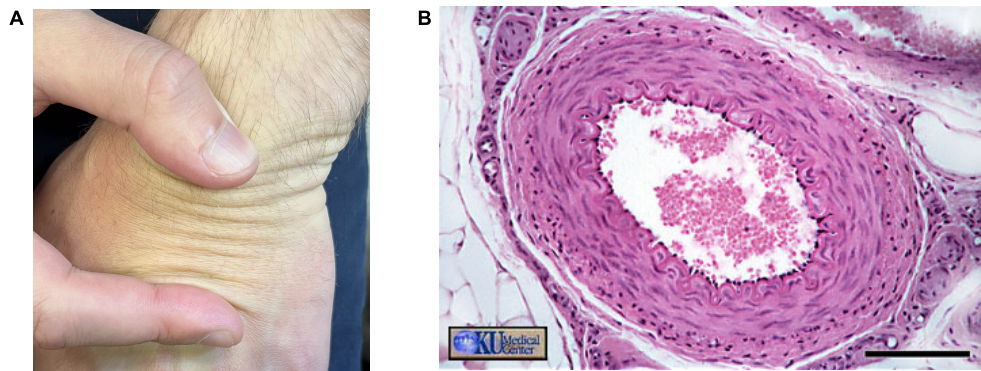
Figure 1.1: (A) Wrinkling in human skin due to uniaxial loading on the back of a hand. (B) Wrinkling of the endothelium (inner lining) of an arterial cross section due to interior pressure changes and tunica media (outer layer) stiffness. This panel is adapted from [1].
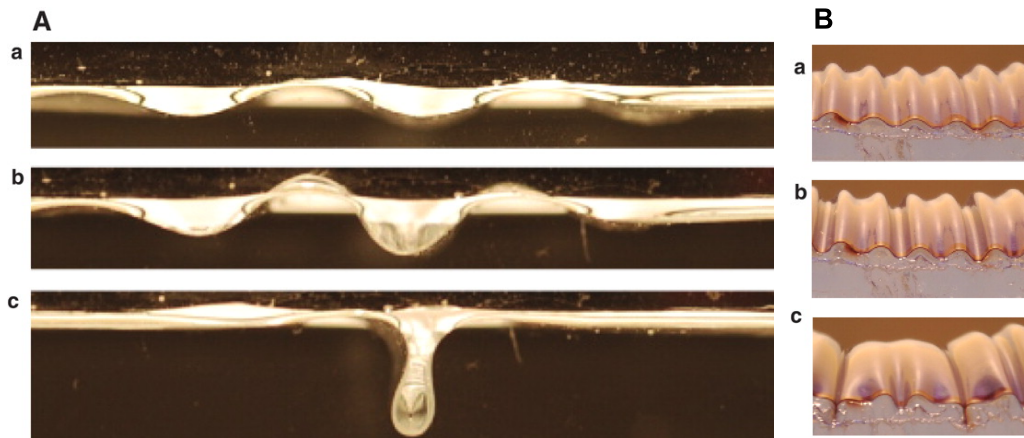
Figure 1.2: (A) A polyester film floating on the surface of water and subjected to a uniaxial horizontal load. Initially, when the load is sufficiently small, the film is periodically globally deformed, a *wrinkled* state (top). Progressive loading leads to the development of a single localized structure, a *fold* state (bottom). (B) A polyester film on the surface of a solid gel substrate transitioning from a wrinkled state to a spatially localized fold state via spatial period-doubling. This figure is adapted from [24].
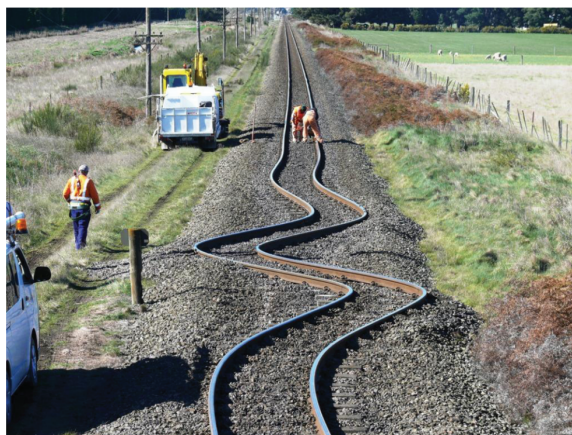
Figure 1.3: Compression induced buckling due to an earthquake in a formerly straight railway in New Zealand. This figure is taken from [38].

In contrast to wrinkling, when the system does not possess a preferred length scale, buckling can occur. Examples of this include patterns in compressed or deflated spherical shells [31, 32], elastic rings bounding a soap film [33, 34, 35, 36], constrained buckling of elastic rings [37], and compressed train tracks (shown in Fig. 1.3) due to earthquakes or extreme heating [38, 39].

Wrinkling is often a phenomenon of interfaces separating two media. For example, the Saffman-Taylor instability, also known as the viscous fingering instability, occurs at the interface of two fluids in a Hele-Shaw cell when a lower viscosity fluid is injected into a more viscous fluid. This leads to a dynamic process of finger-like pattern formation (often referred to as wrinkles) at the fluid-fluid interface [40, 41, 42, 43, 44]. Several examples of this process are shown in Fig. 1.4. When a higher viscosity fluid invades a lower viscosity fluid instead, the interface is stable and forms a uniformly spreading front. Many variations of this instability have been constructed such as those which destabilize conventionally stable Hele-Shaw flows via variable Hele-Shaw cell geometry [45, 46, 47], surfactant introduction [48, 49, 50, 51, 52, 53, 54], or the presence of $A + B \rightarrow C$–type chemical reactions at the fluid-fluid interface [55, 56, 57].

One variation this thesis will take particular interest in is the introduction of a global rotation of the Hele-Shaw cell about a perpendicular axis through the center at a prescribed frequency [58, 59, 60, 61, 62]. In this case, if the density of the inner fluid exceeds that of the outer, the two fluid system is susceptible to a Rayleigh-Taylor-like centrifugal instability as the denser fluid in the center is now unstable to outward displacement. In general the two fluids may have different viscosities such that the instability is mediated by competing centrifugal and viscous effects, or the viscosities may be taken to be the same so that only inertial effects drive the instability. In the case in which steady state solutions are sought, the viscosity has limited impact, only rescaling the parameter values at which solutions occur, but not impacting the overall form of the governing equation. More recently, this instability has been considered in
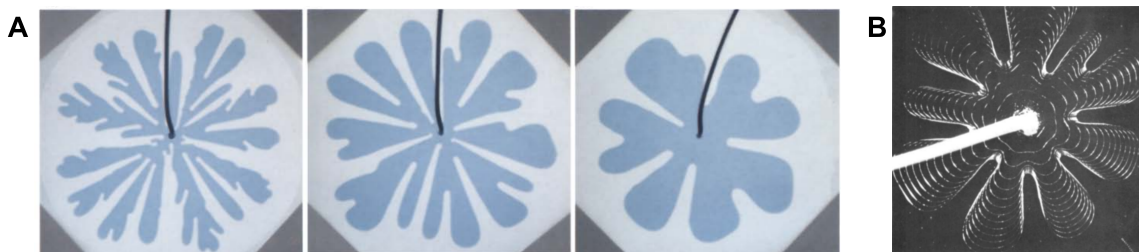
Figure 1.4: (A) Viscous fingering of dyed water dynamically invading a Hele-Shaw cell filled with glycerine. Snapshots taken 40, 90, and 460 seconds after injection begins. Figure adapted from [44]. (B) Overlaid snapshots taken of air injected into a glycerine filled Hele-Shaw cell. Figure adapted from [42].

systems where the interface has additional properties such as a curvature-dependent bending modulus due to a chemical reaction between the two fluids or an added membrane of constrained length composed of a separate material placed between the fluids [63, 64, 59, 65, 66]. If the interface is taken to have nonzero bending modulus, the length scale of the emerging fingering patterns is set by the competition between the bending of the elastica and the centrifugal driving [24] as in the floating elastic sheet example. As in this simpler example, the fingering structures which emerge can take the form of a periodic finger pattern commonly referred to as wrinkles, or isolated single or multiple localized structure(s) called folds. These states represent steady states of the system characterized by force and torque balance.

For many of the systems described above, understanding how surfaces wrinkle and then fold typically requires solving complicated systems of partial differential equations for different geometries governed by complex forces. The thin floating sheet in one dimension is a notable exception. This system possesses a simple ordinary differential equation for steady state solutions which is completely integrable in the limit of infinite spatial extent [67, 21, 22, 68, 23]. The shapes of both wrinkles and folds on thin floating sheets can be described exactly using simple mathematical expressions [21, 22], which naturally entails closed formulas for the wrinkling/folding thresholds in parameter space. Similarly, in-plane buckling of inextensible elastic rings under pressure has been studied over many years [2, 69, 70, 71] and exact expressions for the buckled profiles are known [72, 73, 74]. When compressed, a substrate-supported ring wrinkles with a critical wavelength which can differ from the maximal wavelength onset which occurs in buckling phenomena [21, 24, 25, 22, 75, 23]. In contrast to the fluid supported sheet problem, exact solutions are not known when such a closed elastica is coupled to a solid substrate.

Periodic buckled and wrinkled states of supported rings may emerge quasistatically, for example, in externally confined rings [37, 76] or crumpled spherical shells [31], in centrifugally or magnetically driven interfacial fingering in a Hele-Shaw cell [64, 59, 65, 77, 58] and in the swelling of water-lecithin vesicles [78, 79], but may also

arise dynamically, for example, during the dynamic collapse of an elastic ring around a popped soap film [34, 35], the dynamic wrinkling of compressed floating elastica under drop impact [80], the dynamic buckling of pressurized circular rings [33], the dynamic buckling of a thin spherical shell impacting a plane [81], or in blood vessels [82].

Many of the systems listed above are physically very different, yet the resulting spatial profiles of their wrinkling responses are often strikingly similar. This similarity is not fully explained by existing literature, and this thesis will attempt to explore the foundations of this phenomenon. Continuing the approach taken with the exact solutions of model equations in the case of the fluid supported sheet [21], recent models have opened the possibility of constructing exact solutions for the substrate supported ring [66], a feature which would be crucial for understanding the similarities in wrinkling profiles and controlling the onset of different wrinkling modes across a wide range of systems.

1.1   Outline

The rest of this thesis is organized as follows. In chapter 2, relevant background results on bifurcation theory, numerical techniques, and buckling phenomena are provided to situate the work. In chapter 3, the model is outlined for a generalized system, and in chapters 4 and 5 it is specified to the cases of solid and fluid substrate support and analyzed in each context using analytical and numerical techniques. In chapter 6, exact solutions are constructed for a family of substrate supported problems and relations to prior results on buckling of unsupported tubes are established. In chapter 7, properties of the wrinkling bifurcation are studied. In chapter 8, temporal stability is considered. Finally, in chapter 9, we conclude by summarizing the results and discussing future avenues of exploration enabled by the work as well as potential applications. The material underpinning the results discussed in this thesis is published in [66, 83, 84]. The primary contribution of this thesis is the organization of branches of supported tube profiles into bifurcation diagrams (Fig. 4.2 on page 33) and the mapping of the problem to a simpler well-understood problem (Eqs. 6.16 and Fig. 6.1 on page 61).

Chapter 2

Background

2.1 Elements of bifurcation theory

We will analyze systems from the framework of dynamical systems. Dynamical systems may be defined in terms of a set of ordinary differential equations (ODE's)

$$\dot{\boldsymbol{u}} \equiv \frac{d\boldsymbol{u}}{dt} = \boldsymbol{G}(\boldsymbol{u}, t; \boldsymbol{\lambda}) \tag{2.1}$$

with $\boldsymbol{u} \in U \subset \mathbb{R}^n$ defining the n dimensional solution state of the system, $\boldsymbol{\lambda} \in V \subset \mathbb{R}^p$ defining the p parameters, and $\boldsymbol{G}$ is $\mathbb{C}^r$, $r \geq 1$. When the vector field $\boldsymbol{G}$ depends explicitly on time (i.e. $\boldsymbol{G} = \boldsymbol{G}(\boldsymbol{u}, t; \boldsymbol{\lambda})$), then the system is referred to as *nonautonomous*; when $\boldsymbol{G} = \boldsymbol{G}(\boldsymbol{u}; \boldsymbol{\lambda})$ does not depend explicitly on time it is called *autonomous*.

A *trajectory* $\boldsymbol{u}(t; \boldsymbol{u_0}, t_0)$ of this system is a specific solution to (2.1) determined by the condition that it passes through $\boldsymbol{u_0}$ at time $t = t_0$. The *orbit* through $\boldsymbol{u_0}$ is the set of points in the phase space of the problem which fall on the trajectory defined by $\boldsymbol{u}(t_0) = \boldsymbol{u_0}$. Finally, the *flow* $\phi(\boldsymbol{u}, t)$ of (2.1) is defined as the set of all trajectories generated by $\boldsymbol{G}$ [85].

Dynamical systems may contain *equilibrium solutions*, also called *fixed points*, $\bar{\boldsymbol{u}}$ which satisfy $\boldsymbol{G}(\bar{\boldsymbol{u}}; \boldsymbol{\lambda}) = 0$ such that the solution is time-independent.

For $(\boldsymbol{u_0}, t_0) \in U$, a solution of (2.1) through $\boldsymbol{u_0}$ at t_0 exists for sufficiently small $|t - t_0|$, which we call $\boldsymbol{u}(t, t_0, \boldsymbol{u_0})$. This solution is unique in the sense that any other solution of (2.1) passing through $\boldsymbol{u_0}$ at $t = t_0$ must be the same as $\boldsymbol{u}(t, t_0, \boldsymbol{u_0})$ along their common interval of existence, provided $\boldsymbol{u}$ is Lipschitz continuous in the neighborhood of $\boldsymbol{u_0}$, i.e. that $|\boldsymbol{G}(\boldsymbol{u_1}, t) - \boldsymbol{G}(\boldsymbol{u_2}, t)| \leq K|\boldsymbol{u_1} - \boldsymbol{u_2}|$ for some constant K [85]. When the Lipschitz continuity condition is violated, uniqueness is no longer guaranteed. For example, the system $\dot{u} = \sqrt{u}$, $u(0) = 0$, $u \in [0, \infty)$ is not Lipschitz continuous at the origin, and $u(0) = 0$ admits both $u(t) = 0$ and $u(t) = t^2/4$ as solutions for $t \geq 0$. Note that this corresponds to a system in which the fixed point is reachable in finite reversed time.

The linear stability of a fixed point may be determined from the Jacobian of $\boldsymbol{G}$ evaluated at $\bar{\boldsymbol{u}}$ via

$$\boldsymbol{G}(\bar{\boldsymbol{u}} + \delta\boldsymbol{u}) = \boldsymbol{G}(\bar{\boldsymbol{u}}) + \boldsymbol{G_u}(\bar{\boldsymbol{u}})\delta\boldsymbol{u} + \mathcal{O}(\delta u^2) = \boldsymbol{G_u}(\bar{\boldsymbol{u}})\delta\boldsymbol{u} + \mathcal{O}(\delta u^2) \qquad (2.2)$$

where we are considering the growth of a perturbation $\delta\boldsymbol{u}$ from our fixed point. This perturbation may be written in terms of the eigenvalues and eigenvectors $(\mu_i, \boldsymbol{v}_i)$ of the Jacobian matrix $\boldsymbol{G_u}$:

$$\delta\boldsymbol{u} = \sum_{i=1}^{n} c_i \boldsymbol{v}_i e^{\mu_i t} \qquad (2.3)$$

where the prefactors c_i are determined by initial conditions. For real vector fields $\boldsymbol{G}$, the eigenvalues may be complex but come in pairs $(\mu, \bar{\mu})$ when this is the case.

A fixed point is said to be *hyperbolic* when the Jacobian matrix evaluated at this equilibrium has no eigenvalues with zero real component ($\mathrm{Re}(\mu_i) \neq 0$). The Jacobian matrix is necessarily nonsingular at such points. It is *nonhyperbolic* when at least one eigenvalue has a vanishing real component. In this case, the Jacobian matrix can still be nonsingular such as for Poincare-Andronov-Hopf bifurcations in which the eigenvalues have nonzero imaginary component (discussed below). For hyperbolic fixed points, the linear stability is determined by the signs of the eigenvalues. If all the eigenvalues have a negative real component, the equilibrium is a locally stable hyperbolic fixed point. If any eigenvalue has a real component greater than zero, the state will experience exponential growth along the dimension defined by the corresponding eigenvector upon being infinitesimally perturbed. This growth will eventually be saturated by the (currently ignored) nonlinear terms. Provided the fixed point is hyperbolic, the Hartman-Grobman theorem ensures that the flow generated by $\boldsymbol{G}$ is $\mathbb{C}^0$ conjugate to the flow generated by the linearized vector field $\boldsymbol{G_u}(\boldsymbol{u_0})$ in a sufficiently small neighborhood of the fixed point [86]. This ensures that $\boldsymbol{G}$ can be locally approximated by its linearization such that linear stability results apply. The stable eigenspace is spanned by the $\boldsymbol{v}_i$ with associated $\mathrm{Re}(\mu_i) < 0$, while the unstable eigenspace is spanned by the $\boldsymbol{v}_i$ with associated $\mathrm{Re}(\mu_i) > 0$. These spaces are respectively tangent to the stable invariant manifold $W^s(\boldsymbol{u_0})$ (the set of points $\boldsymbol{u}'$ which evolve to $\boldsymbol{u_0}$ in the limit $t \to \infty$) and the unstable invariant manifold $W^u(\boldsymbol{u_0})$ (the set of points $\boldsymbol{u}'$ which evolve to $\boldsymbol{u_0}$ in the limit $t \to -\infty$). If the fixed point is *nonhyperbolic*, then there is a third nonempty eigenspace spanned by eigenvectors $\boldsymbol{v_i}$ corresponding to eigenvalues along the imaginary axis which is tangent to the center invariant manifold $W^c(\boldsymbol{u_0})$. In this case, the Hartman-Grobman theorem no longer guarantees the nonlinear system is qualitatively the same around the fixed point. A simple example is given by $\dot{x} = x^2$, in which $\bar{x} = 0$ is a nonhyperbolic fixed point. The linearization about the origin ($\dot{x} = 0$) implies that a suitably small perturbation about the origin does not evolve away, but the nonlinear dynamics of the system reveal that the orbit of a negative perturbation returns to the origin while that of a

positive perturbation diverges. Clearly, no $\mathbb{C}^0$ conjugate transformation connects the dynamics of the linearization to the complete nonlinear system in this case.

Under quasistatic variation of one or more parameters, the fixed points of a system may experience changes in their location, stability, and number, i.e. the locations of the fixed points in general depends on the parameters involved in the problem. In general, small perturbations to parameters do not lead to qualitative changes following the implicit function theorem, and the fixed points are considered structurally stable. The implicit function theorem, applied to (2.1), ensures that, provided $\boldsymbol{G} : \mathbb{R}^{n+m} \to \mathbb{R}^m$ is continuously differentiable and $\boldsymbol{G}(\boldsymbol{\lambda}, \boldsymbol{u}) = 0$ for $\boldsymbol{\lambda} \in \mathbb{R}^n$ and $\boldsymbol{u} \in \mathbb{R}^m$, then if $\boldsymbol{G_u}$ is invertible then there exists a unique continuously differentiable function $\boldsymbol{g} : \mathbb{R}^n \to \mathbb{R}^m$ in a suitably small neighborhood about $(\boldsymbol{\lambda}, \boldsymbol{u})$ such that $\boldsymbol{G}(\boldsymbol{\lambda}, \boldsymbol{g}(\boldsymbol{\lambda})) = 0$ [86].

However, at certain parameter values, the implicit function theorem may fail, indicated by a loss of invertibility in the Jacobian matrix for steady state bifurcations, and a bifurcation occurs in which new fixed points emerge or previous fixed points disappear. Examples will be provided in the next subsection.

Due to the Hartman-Grobman theorem, hyperbolic fixed points are structurally stable, and no qualitative changes to the dynamics may occur locally. For this reason, a local bifurcation occurs when one or more eigenvalues of the linearized system pass through the imaginary axis, at which point the implicit function theorem fails. By consideration of the spectrum of the Jacobian under parameter variation, therefore, a bifurcation diagram may be constructed for the system detailing the fixed points at each parameter value. These fixed points indicate the possible solutions for a system, and the state of a system at a parameter value may be analyzed by considerations of stability of the available states. For this reason, bifurcation diagrams are powerful tools to fully explore what can occur in a system. The simplest bifurcations are the result of variation of a single parameter, however, some bifurcations require multiple parameters to be simultaneously and independently varied in order to occur. The *codimension* of a bifurcation point is the minimal number of parameters which can be varied to induce the bifurcation to occur. For example, the buckling of a rod from a flat state to a bowed state may be accomplished by changing solely the uniaxial load, a codimension one bifurcation. We may compare this to Rayleigh-Benard convection in which a fluid is heated from below and transitions from a static and thermally vertically stratified state to a series of overturning convection rolls as the hot, lower density fluid on the bottom ascends and the colder, denser fluid on top descends. The onset of this transition depends on both the Rayleigh number, the ratio of the timescales of diffusive thermal transport to convective thermal transport in the fluid, as well as the Prandtl number, the ratio of momentum to thermal diffusivity [87, 88]. The codimension of Rayleigh-Benard convection onset is therefore two because both parameters are required to describe the transition fully.

(a) Saddle-node bifurcation: $\dot{x} = \mu - x^2$

(b) Saddle-node bifurcation: $\dot{x} = \mu + x^2$
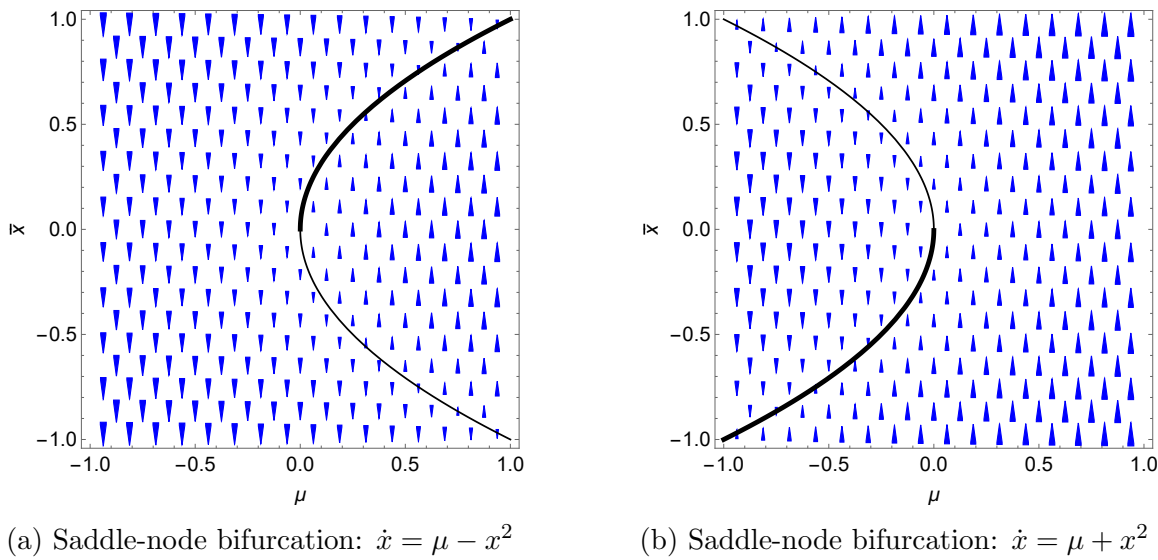
Figure 2.1: Saddle-node bifurcation with equilibrium solutions $\bar{x}$ plotted as a function of μ in black with stable (thick) and unstable (thin) lines. The underlying vector field is plotted in blue as a function of μ.

2.1.1 One-dimensional systems

The saddle-node bifurcation, also called a fold bifurcation, is the simplest mechanism for the creation or destruction of equilibrium points as a single parameter is varied, making it the generic codimension one bifurcation in a 1D system [89]. This is shown in Fig. 2.1, where, in Fig. 2.1a a pair of solutions come into existence as μ increases past zero and in Fig. 2.1b a pair of solutions collide and disappear.

The pitchfork bifurcation is the prototypical bifurcation for systems with $x \to -x$ symmetry for which $x = 0$ is always an equilibrium solution. This is shown in Fig. 2.2. In the supercritical case, as the parameter μ increases, stability is exchanged from $\bar{x} = 0$ to the bifurcating branches $\bar{x} = \pm\sqrt{\mu}$. In the subcritical case, the nonzero branches are unstable, and stability of the $\bar{x} = 0$ solution is lost as μ increases through $\mu = 0$.

The transcritical bifurcation is the prototypical bifurcation for systems where equilibrium points experience a change in stability but are not created or destroyed. This is shown in Fig. 2.3 where the zero solution branch and the $\bar{x} = \pm\mu$ branch persists (a, + case; b, − case).

The cusp (or hysteresis) bifurcation is one of the simplest codimension two bifurcations occurring in a one-dimensional system. The supercritical cusp bifurcation is shown in Fig. 2.4, resulting from the two parameter system $\dot{x} = \mu + \beta x - x^3$. We note that the particular choice $\mu = 0$ yields the familiar supercritical pitchfork bifurcation in β. The cusp bifurcation also results in the emergence of hysteresis for $\beta > 0$. Increasing μ from $\mu = -1$, the system remains on the lower branch of the equilibrium
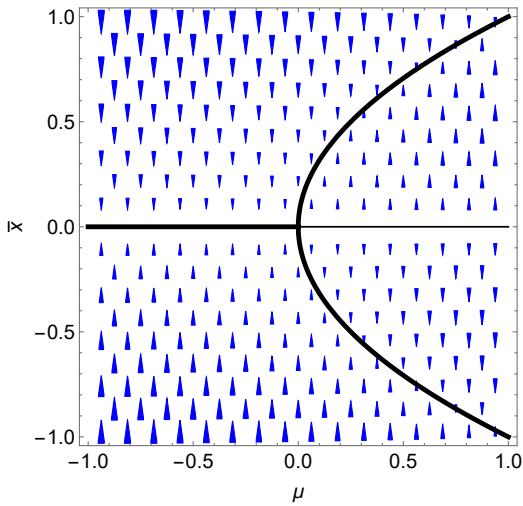
(a) Supercritical pitchfork bifurcation:
$\dot{x} = x(\mu - x^2)$
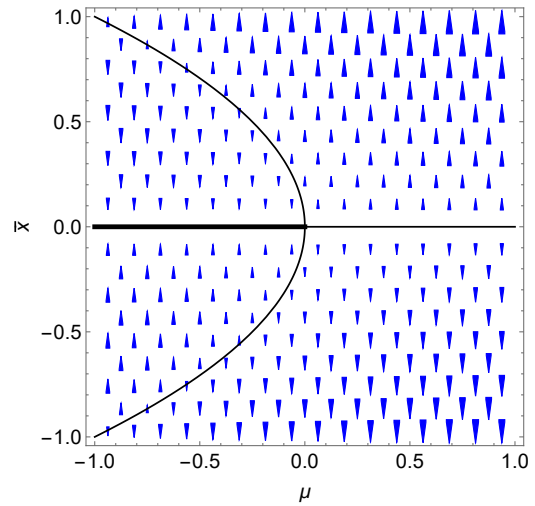
(b) Subcritical pitchfork bifurcation:
$\dot{x} = x(\mu + x^2)$

Figure 2.2: Pitchfork bifurcation with equilibrium solutions $\bar{x}$ plotted in black with stable (thick) and unstable (thin) lines as a function of μ. The underlying vector field across x is plotted in blue as a function of μ.
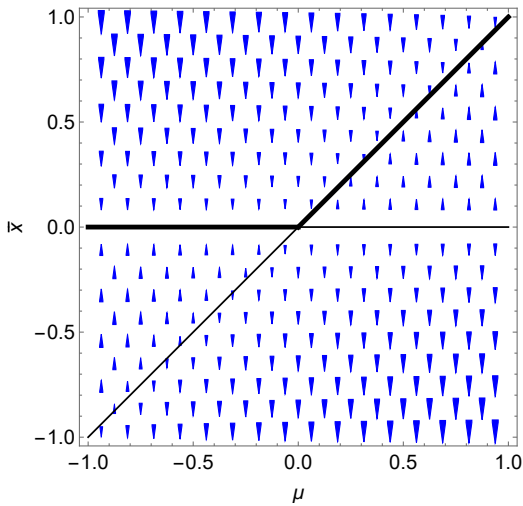
(a) Transcritical bifurcation:
$\dot{x} = x(\mu - x)$
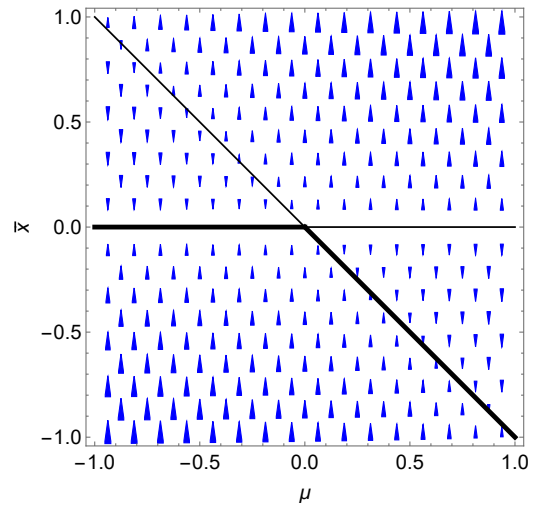
(b) Transcritical bifurcation:
$\dot{x} = x(\mu + x)$

Figure 2.3: Transcritical bifurcation with equilibrium solutions $\bar{x}$ plotted in black with stable (thick) and unstable (thin) lines as a function of μ. The underlying vector field across x is plotted in blue as a function of μ.

10
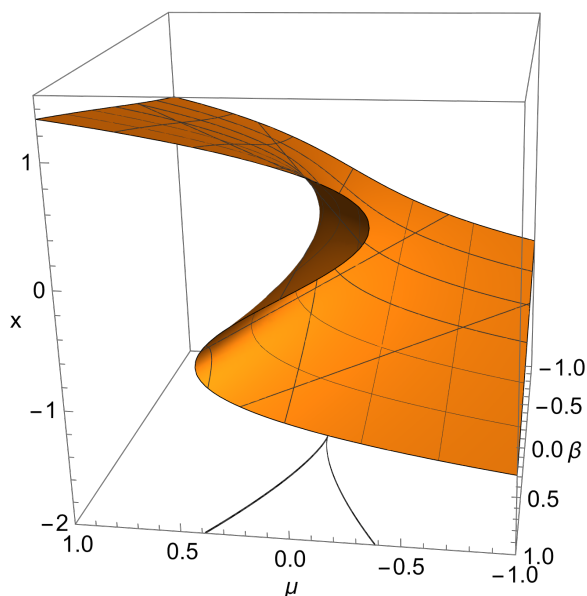
Figure 2.4: Cusp bifurcation with the equilibrium manifold $\bar{x}$ of $\dot{x} = \mu + \beta x - x^3$ plotted in orange as a function of parameters (μ, β). In the parameter regime supporting multiple solutions, the upper and lower branches are stable while the middle branch is unstable. Projecting this manifold down onto the parameter plane yields two fold bifurcation curves shown in black and the cusp singularity at the origin where they tangentially collide.

manifold until it reaches the fold bifurcation curve defined by $\mu^* = 2\beta^{3/2}/3^{3/2}$. Beyond this value, the lower branch of solutions ceases to exist, and the solution 'jumps' to the upper branch. From this point, decreasing μ does not revert the solution to the lower branch until it reaches the other fold bifurcation curve at $\mu^* = -2\beta^{3/2}/3^{3/2}$. This pathway defines a hysteresis-loop for the system, relevant to many systems in biology. For example, the cusp bifurcation provides an effective local model for the weakly connected neural network model in neuroscience [90].

2.1.2 Two-dimensional systems

For a two-dimensional system, the Jacobian Df is given by the 2 by 2 matrix:

$$\boldsymbol{A} = \begin{pmatrix} \frac{\partial f_1}{\partial x} & \frac{\partial f_1}{\partial y} \\ \frac{\partial f_2}{\partial x} & \frac{\partial f_2}{\partial y} \end{pmatrix} \tag{2.4}$$

The eigenvalues may be written in terms of the trace of the Jacobian $\tau \equiv Tr(\boldsymbol{A})$ and the determinant of the Jacobian $\Delta \equiv det(\boldsymbol{A})$ as:

$$\lambda_{1,2} = \frac{1}{2}\left(\tau \pm \sqrt{\tau^2 - 4\Delta}\right). \tag{2.5}$$

11

The kinds of vector fields observed locally around a fixed point may thus be classified by the relative size and sign of the trace and determinant. When the determinant is negative, a saddle point occurs in which points flow in towards the equilibrium along one axis and out away from the equilibrium along the other. When the determinant is positive, the equilibrium is unstable (stable) when the trace is positive (negative). This may be further subdivided into spirals when $\tau^2 < 4\Delta$ and nodes when $\tau^2 > 4\Delta$. These results are summarized in Fig. 2.5 with example vector fields for each case. In this figure, we show only fixed points, but, in two-dimensional systems, discrete periodic orbits become possible as well.
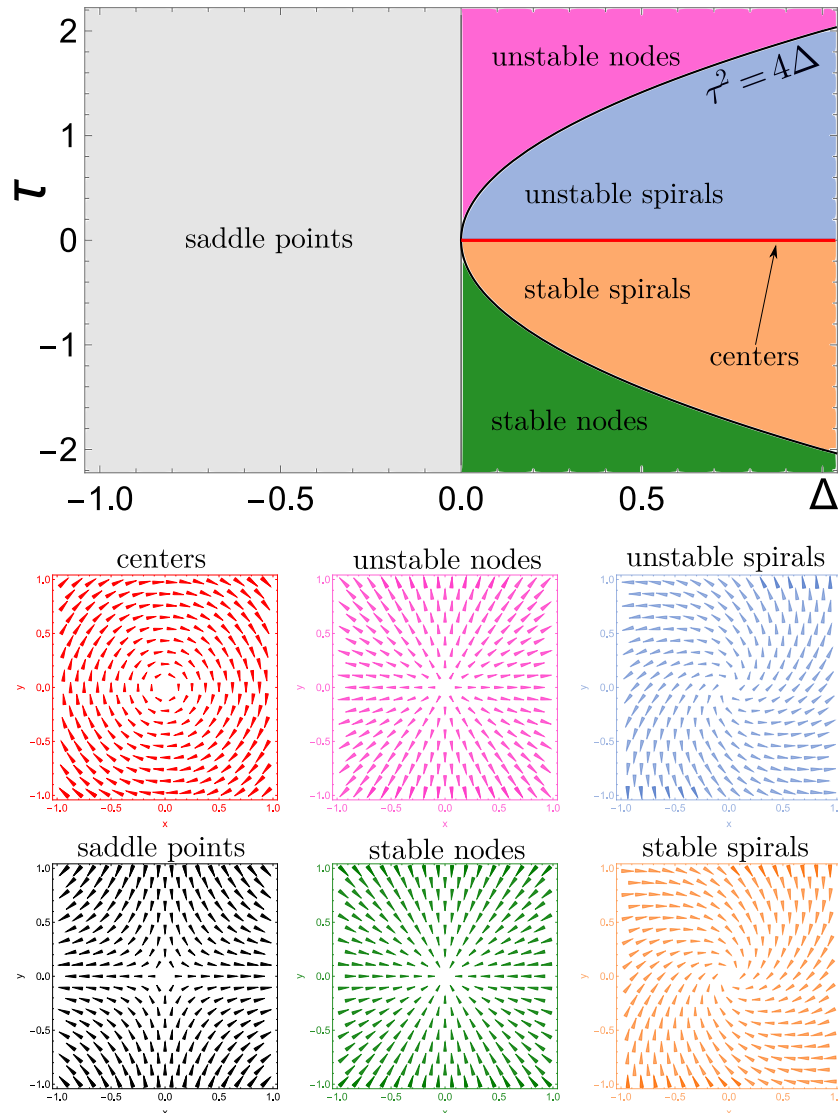
Figure 2.5: Classification of equilibrium solutions $(x, y) = (0, 0)$.

The Poincaré-Andronov-Hopf bifurcation is the generic two-dimensional codimen-
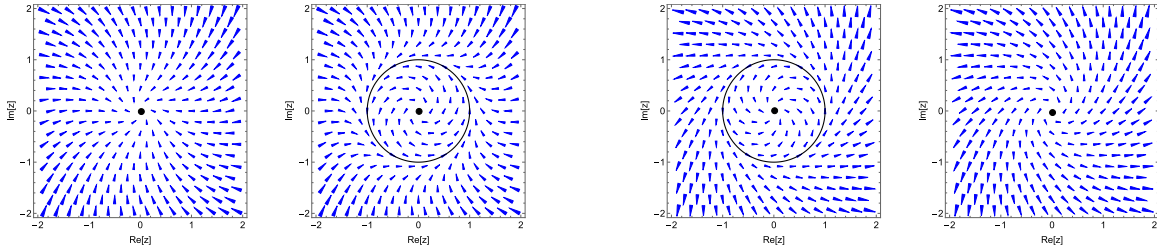
(a) Supercritical Hopf bifurcation:
$\dot{z} = (\mu + i(w + c_1\mu))z - (1 + ic_2)|z|^2 z.$

(b) Subcritical Hopf bifurcation:
$\dot{z} = (\mu + i(w + c_1\mu))z + (1 + ic_2)|z|^2 z$

Figure 2.6: The vector field of the Hopf bifurcation normal form with the equilibrium solution at the origin and the periodic orbit at radius 1, both plotted in black. The constants are $\omega = 1, c_1 = c_2 = 0.5$. In each subfigure, the left panel has $\mu = -1$ and the right panel has $\mu = 1$.

sion one bifurcation of a periodic orbit from a fixed point. This bifurcation is characterized by a pair of complex-conjugate eigenvalues crossing the imaginary axis with nonzero magnitude. The normal form is given by

$$\dot{z} = (\mu + i(w + c_1\mu))z \pm (1 + ic_2)|z|^2 z \qquad (2.6)$$

where z is a complex variable, μ is the parameter being varied, and c_1, c_2, ω are fixed parameters. Examining only the term linear in z, it is immediately apparent that the origin is a stable equilibrium solution for $\mu < 0$, an unstable equilibrium solution for $\mu > 0$, and at $\mu = 0$ the eigenvalues are the imaginary complex conjugates $\pm i\omega$. This pair of imaginary eigenvalues leads to oscillations of fixed amplitude following Eq. (2.3). Examples of the dependence of the vector field on μ are shown in Fig. 2.6. We note that the periodic orbit is stable in the supercritical case but unstable in the subcritical case.

2.2 Temporal stability

To provide an example of a temporal stability analysis, we analyze the 3-5 Swift-Hohenberg equation and compare to existing literature. We take

$$\partial_t u = ru - (1 + \partial_x^2)^2 u + b_3 u^3 - u^5 \qquad (2.7)$$

and the ansatz $u = u_0 + (u_v e^{\sigma t})$, expanding around the base state $u_0 = 0$ and linearizing. We obtain:

$$\sigma u_v = \left(r - 1 - 2\partial_x^2 - \partial_x^4\right) u_v \qquad (2.8)$$

We can solve this eigenvalue equation numerically for σ and u_v given r and using finite difference matrices for the derivatives.

In Fig. 2.7, we observe a change in the stability of the base state with respect to periodic perturbations as the primary parameter r is varied. As r increases from below 0, the eigenvalue corresponding to a 5-wavelength periodic eigenmode crosses the imaginary axis along the real line. As r continues to increase, the eigenvalues shift to the right, and the system eventually also becomes unstable to the longer wavelength eigenmodes shown.

This problem may also be treated analytically if we further specify our ansatz to seek periodic states of wavenumber q via $u = u_0 + u_p e^{\sigma t} e^{iqx}$. We find the growth rate σ_q of a wavenumber q periodic state is given via $\sigma_q = r - (q^2 - 1)$, a type-I instability which is first positive for $r = 0$ and $q = 1$ as shown in Fig. 2.8. Thus, on a periodic domain of length $L = 10\pi$, we expect a periodic state with 5 wavelengths to become unstable first. This exactly matches the numerical results shown above, discussed further in [91, 92].
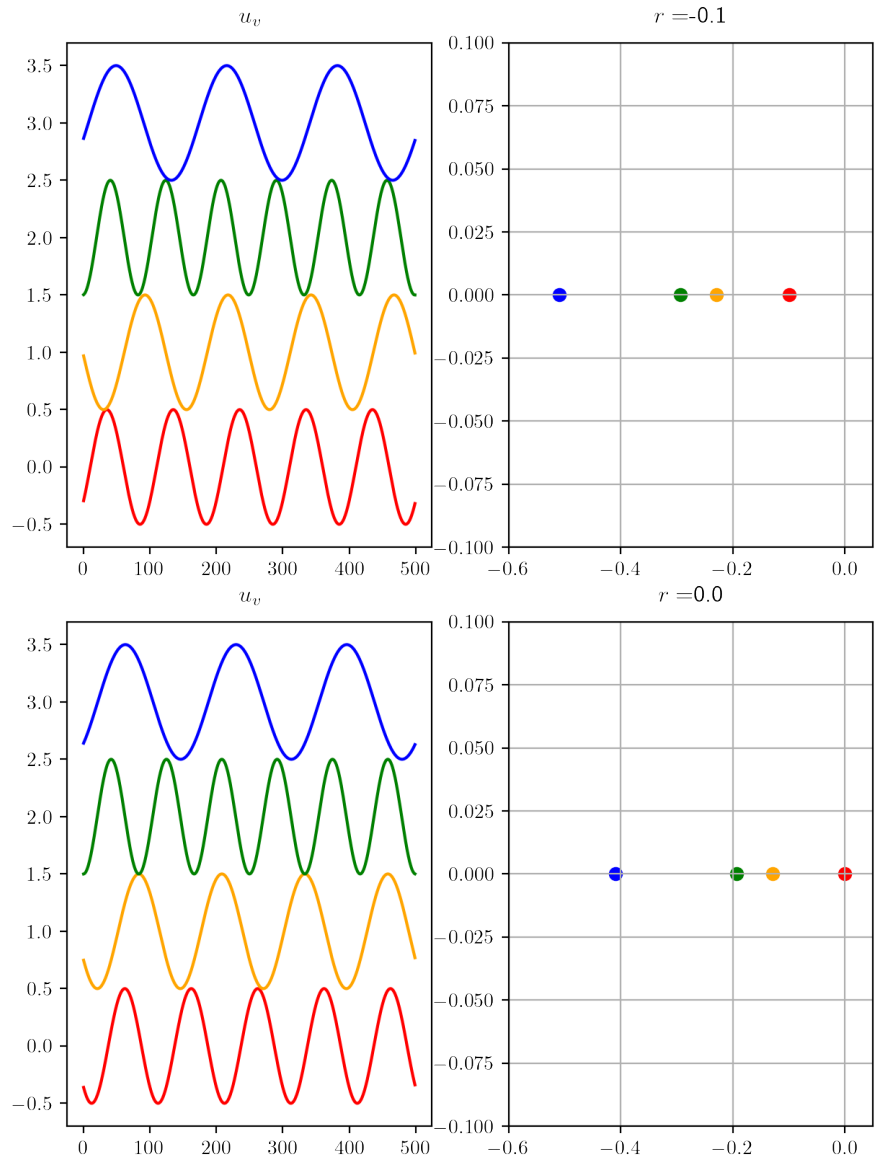
Figure 2.7: Spectrum of the four largest eigenvalues for $b_3 = 2$ and $L = 10\pi$ in the linearized 3-5 Swift-Hohenberg equation.
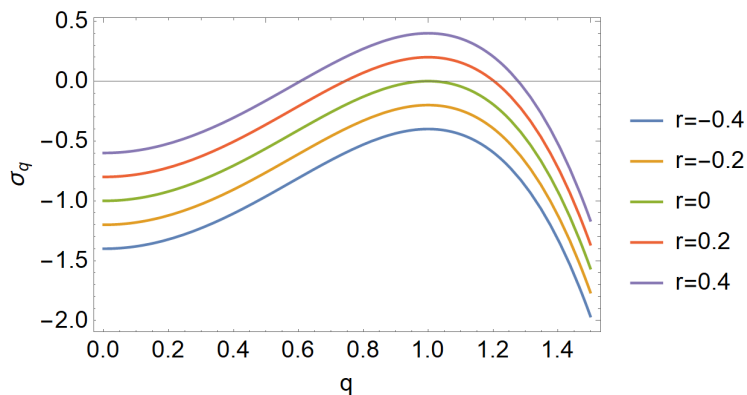
Figure 2.8: Growth rate σ_q as a function of wavenumber q across varying r.

2.3   The Fredholm Alternative theorem

The Fredholm Alternative theorem provides important solvability conditions for the process of generating an expansion-based solution via weakly nonlinear analysis of a boundary value problem (BVP). In a weakly nonlinear analysis, the (unknown) solution and system parameters are expanded in powers of a small parameter ϵ, and the resulting equation is solved order by order in the small parameter, framed as $L[u_i] = \mathcal{N}_i$ at order $\mathcal{O}(\epsilon^i)$, $i = 0, 1, 2, ...$ for a linear operator L resulting from inserting the expansion $u = \sum_0^N \epsilon^i u_i$ into the BVP. When the operator is self-adjoint and one order of the problem is homogenous (i.e. $L[v_i] = 0$) such that $L = L^*$ has a nullspace spanned by v_i, then all eigenfunctions for the inhomogenous problems at higher orders must be orthogonal to the eigenfunctions of the homogenous problem. In this way, the solutions to the homogenous problem may be used as solvability conditions for the inhomogenous problems and solutions may be obtained order by order.

Specifically, the theorem states: if L is a linear operator, and its adjoint L^* has a kernel which is spanned by v_i for $i = 1, ..., k$, then we require $< v_i, b >= 0$ for $i = 1, ..., k$ as necessary and sufficient conditions to solve $Lu = b$. In general terms, this can be seen by taking the inner product of the problem with v_i and applying the definition of the adjoint.

$$Lu = b \tag{2.9}$$

$$\langle v_i, Lu \rangle = \langle v_i, b \rangle \tag{2.10}$$

$$\langle L^* v_i, u \rangle = \langle 0, u \rangle = 0 = \langle v_i, b \rangle . \tag{2.11}$$

This can be seen more explicitly, for example, in Sturm-Liouville theory where $L = L^*$ is self-adjoint and a Sturm-Liouville operator, and we seek solutions to the BVP $L[u] = f(x)$. If the only solution to $L[u] = 0$ is $u = 0$ then there exists a unique solution to the BVP. If there exist nontrivial solutions to $L[u] = 0$ (i.e. 0 is an eigenvalue), then there are either no solutions or infinitely many. As a proof,

16

following [93], we expand $u(x)$ in terms of the eigenfunctions $\phi(x)$ of L

$$u(x) = \sum_{n=1}^{\infty} a_n \phi_n(x) \tag{2.12}$$

where these eigenfunctions are given by the eigenvalue problem

$$L[\phi_i(x)] = -\lambda_i w(x)\phi_i(x), \tag{2.13}$$

for a weight $w(x)$.

Writing $L[u] = f(x)$ and expanding $u(x)$ yields:

$$L\left[\sum_{n=1}^{\infty} a_n \phi_n(x)\right] = f(x), \tag{2.14}$$

and applying the linearity of L yields:

$$\sum_{n=1}^{\infty} (a_n L[\phi_n(x)]) = f(x). \tag{2.15}$$

This may be written as:

$$\sum_{n=1}^{\infty} (-a_n \lambda_n w(x)\phi_n(x)) = f(x). \tag{2.16}$$

The orthogonality of the eigenfunctions requires that, if we take the inner product with an eigenfunction $\phi_i(x)$, we obtain

$$-a_n \lambda_n \int \phi_n^2(x)w(x)dx = \int f(x)\phi_n(x)dx, \tag{2.17}$$

or that

$$a_n = -\frac{\int f(x)\phi_n(x)dx}{\lambda_n \int \phi_n^2(x)w(x)dx}. \tag{2.18}$$

The consequence of this equation is that the coefficients of the eigenfunction expansion for $u(x)$ are given by the above equation and $u(x)$ exists provided all eigenvalues $\lambda_i \neq 0$. If, instead, an eigenvalue $\lambda_n = 0$, then in order for $u(x)$ to be a solution, we require

$$\int \phi_n(x)f(x)dx = 0, \tag{2.19}$$

i.e. the nonhomogenous term must be orthogonal to the null eigenfunction, and if this is not the case then no solution exists [93].

2.4 Numerical methods

2.4.1 Numerical continuation

Numerical continuation is a process of determining a solution to the problem $G(u, \lambda) = 0$ i.e. as a function of the parameter λ. This relies on the existence and persistence of a solution family $u(\lambda)$ as dictated by the implicit function theorem. Framed in terms of the numerical continuation problem, if $G : \mathbb{R}^n \times \mathbb{R} \to \mathbb{R}$ satisfies

1. $G(u_0, \lambda_0) = 0, \quad u_0 \in \mathbb{R}^n, \lambda_0 \in \mathbb{R}$

2. The Jacobian matrix $G_u(u_0, \lambda_0)$ is nonsingular (i.e. u_0 is an isolated solution)

3. G and G_u are smooth near u_0

then there is a solution family $u(\lambda)$ which is smooth and unique such that

1. $G(u(\lambda), \lambda) = 0$ for any λ near λ_0

2. $u(\lambda_0) = u_0$

The simplest form of numerical continuation is parameter (or natural) continuation [94, 95]. In this framework, an isolated solution (u_0, λ_0) and a direction vector $\frac{du_0}{d\lambda}$ are known. A new solution u_1 at parameter $\lambda_1 = \lambda_0 + \delta\lambda$ may be computed by solving

$$G(u_1, \lambda_1) = 0 \tag{2.20}$$

via Newton's method (provided G_u is nonsingular and $\Delta\lambda$ is small) [96]. At step ν of this process, this is given by:

$$G_u(u_1^\nu, \lambda_1)\Delta u_1^\nu = -G(u_1^\nu, \lambda_1), \tag{2.21}$$
$$u_1^{\nu+1} = u_1^\nu + \Delta u_1^\nu, \tag{2.22}$$

where the process is initialized with $u_1^0 = u_0 + \Delta\lambda\frac{du_0}{d\lambda}$. This process is iterated and yields quadratic convergence $u_1^\nu \to v$ provided the starting point is close enough for the linear approximation of G to hold, $G(v, \lambda_1) = 0$, and $G_u(v, \lambda_1) \neq 0$. Tolerances defining sufficient convergence and step sizes must both be input into the algorithm and adapted for the specific circumstances of the problem.

Once a solution (u_1, λ_1) is obtained, $\frac{du_1}{d\lambda}$ can be obtained by differentiating $G(u(\lambda), \lambda) = 0$ with respect to λ, yielding:

$$G_u(u_1, \lambda_1) \cdot \frac{du_1}{d\lambda} + G_\lambda(u_1, \lambda_1) = 0. \tag{2.23}$$

The process may then be repeated to generate a branch of solutions. This approach fails when the continuation approaches a fold point where the Jacobian becomes
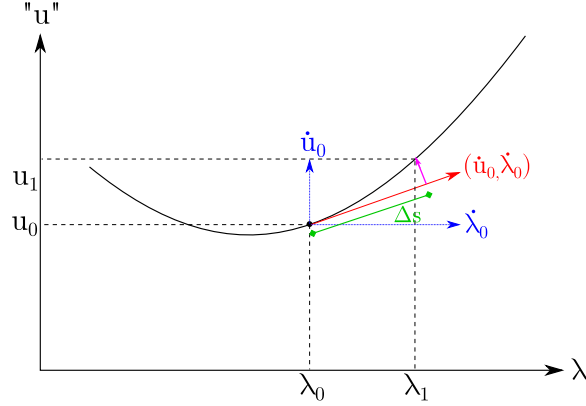
Figure 2.9: Schematic view of pseudo-arclength continuation as described in Eqs. 2.24,2.25

singular. Physically, at these points the continuation must double back on itself in the continuation parameter, with $\frac{d\boldsymbol{u_1}}{d\lambda}$ becoming infinite at the fold point and leading Newton's method to fail [97].

To overcome this challenge, pseudo-arclength continuation is used in which perturbations to the solution and parameter are made based on a step size Δs, and we consider derivatives taken along the tangent to the arc of the solution branch. Defining the overdot as $\frac{d}{ds}$, this step is taken along the plane tangent to the solution branch at $(\boldsymbol{u_0}, \lambda_0)$ and perpendicular to $(\dot{\boldsymbol{u}}_0, \dot{\lambda}_0)$. Δs defines the distance of the step taken in this extended space, tangent to the the solution branch in contrast to $\Delta\lambda$ which projected in a lower dimensional space solely in the direction of increasing λ. This approach requires we solve the extended system:

$$\boldsymbol{G}(\boldsymbol{u_1}, \lambda_1) = 0 \tag{2.24}$$

$$(\boldsymbol{u_1} - \boldsymbol{u_0}) * \dot{\boldsymbol{u}}_0 - (\lambda_1 - \lambda_0)\dot{\lambda}_0 - \Delta s = 0 \tag{2.25}$$

via Newton's method:

$$\begin{pmatrix} (\boldsymbol{G_u^1})^\nu & (\boldsymbol{G_\lambda^1})^\nu \\ \dot{\boldsymbol{u}}_0{}^* & \dot{\lambda}_0 \end{pmatrix} \cdot \begin{pmatrix} \Delta\boldsymbol{u_1^\nu} \\ \Delta\lambda_1^\nu \end{pmatrix} = - \begin{pmatrix} \boldsymbol{G}(\boldsymbol{u_1^\nu}, \lambda_1^\nu) \\ (\boldsymbol{u_1^\nu} - \boldsymbol{u_0}) * \dot{\boldsymbol{u}}_0 + (\lambda_1^\nu - \lambda_0)\dot{\lambda}_0 - \Delta s \end{pmatrix} \tag{2.26}$$

This process is shown schematically in Fig. 2.9.

The direction vector at the next step may be computed by taking derivatives of Eqs. (2.24),(2.25) with respect to λ analogously to Eq. (2.23). Doing so yields:

$$\begin{pmatrix} \boldsymbol{G_u^1} & \boldsymbol{G_\lambda^1} \\ \dot{\boldsymbol{u}}_0{}^* & \dot{\lambda}_0 \end{pmatrix} \cdot \begin{pmatrix} \dot{\boldsymbol{u}}_1 \\ \dot{\lambda}_1 \end{pmatrix} = \begin{pmatrix} \boldsymbol{0} \\ 1 \end{pmatrix}. \tag{2.27}$$

In this form of continuation, Δs defines a distance we move along the branch of solutions rather than just advancing in the parameter λ. This allows branches of

solutions to be continued past a fold. For a boundary value problem (BVP) defined on a domain $x_j \in [0, 1]$, this is done across a mesh $[x_0 = 0, x_N = 1]$ where naively $\Delta x = 1/N$ and where derivatives are defined in terms of finite differences such that $\boldsymbol{G_u}$ is a tridiagonal matrix. AUTO employs a more sophisticated method using orthogonal collocation with piecewise polynomials to perform numerical continuation of BVP's more efficiently and with adaptive mesh-selection [95]. This is accomplished as follows. We introduce Lagrange basis polynomials $\{\ell_{j,i}(x)\}$ in each interval $[x_{j-1}, x_j]$ with $j = 1, ..., N$ defining the interval index, $i = 0, 1, ..., m$ with m defining the maximal degree of the polynomial, and $h_j = x_j - x_{j-1}$ defining the interval size:

$$\ell_{j,i}(x) = \prod_{k=0, k \neq i}^{m} \left(\frac{x - (x_j - \frac{k}{m}h_j))}{(x_j - \frac{i}{m}h_j) - (x_j - \frac{k}{m}h_j)} \right) . \tag{2.28}$$

The local polynomials $\boldsymbol{p}_j(x)$ on the interval $[x_{j-1}, x_j]$ can be written in terms of these basis polynomials:

$$\boldsymbol{p}_j(x) = \sum_{i=0}^{m} \ell_{j,i}(x) \boldsymbol{u} \left(x_j - \frac{i}{m}h_j \right) . \tag{2.29}$$

In this way, an approximation to the solution of the continuous problem $\boldsymbol{u}(x)$ may be assembled piecewise from orthogonal Lagrange basis polynomials. This generates $N \times m \times n$ collocation equations for a set of n coupled differential equations with N mesh points and approximated by polynomials of degree m:

$$\boldsymbol{p}_j'(z_{j,i}) = G(\boldsymbol{p}_j(z_{j,i}), \lambda) \tag{2.30}$$

where $z_{j,i}$ are the collocation points in the subinterval $[x_{j-1}, x_j]$, i.e. the mth degree polynomial roots. Boundary and integral conditions may also discretized on this domain and define n_b and n_q additional equations to solve. Finally, the pseudo-arclength equation (2.25) defines one final equation, yielding a total of $mNn + n_b + n_q + 1$ nonlinear equations to be solved for the unknowns $\{\boldsymbol{u}\left(x_j - \frac{i}{m}h_j\right), \lambda\}$ via Newton-Chord iteration. When continuation is implemented numerically on such a discretized domain, the Jacobian matrix of the extended system takes the form of a bordered tridiagonal matrix [94].

Phase conditions

For BVP's satisfying $\mathbf{G}(\mathbf{u}(x), \lambda) = \mathbf{0}$ defined on a domain x with a periodic solution $\mathbf{u_k}(\mathbf{x})$ satisfying the boundary conditions on the kth step of numerical continuation, if $\mathbf{u}_k(x)$ is a solution then so too is $\mathbf{u}_k(x + d)$ for arbitrary d. This creates an ambiguity for the numerical continuation algorithm loop as a continuous family of states exists at each step, and any of them may satisfy the governing equation equally well. This can lead to periodic states 'travelling' along the domain with each Newton loop without improving convergence and can lead to states of arbitrary phase being obtained at each parameter step, which makes comparison challenging. To eliminate this freedom,

we impose a *phase condition*, an additional constraint that the solution to the system must minimize:

$$D(d) \equiv \int ||\mathbf{u}_k(x+d) - \mathbf{u}_{k-1}(x)||_2^2 \, dx \,. \tag{2.31}$$

In order to minimize this, the optimally chosen solution at step k, $\mathbf{u}_k(x+\tilde{d})$, satisfies $D'\left(\tilde{d}\right) = 0$. Taking the derivative of (2.31) with respect to $\tilde{d}$, we have:

$$\int \left(\mathbf{u}_k(x+\tilde{d}) - \mathbf{u}_{k-1}(x)\right) \cdot \partial_{\tilde{d}} \mathbf{u}_k(x+\tilde{d}) \, dx = 0 \tag{2.32}$$

Choosing the initial phase such that $\tilde{\mathbf{u}}_k(x) \equiv \mathbf{u}_k(x+\tilde{d}) = 0$ yields the requirement:

$$\int \left(\tilde{\mathbf{u}}_k(x) - \tilde{\mathbf{u}}_{k-1}(x)\right) \cdot \partial_{\tilde{d}} \tilde{\mathbf{u}}_k(x) \, dx = 0 \,. \tag{2.33}$$

This equation augments the primary equation, which itself gains an additional term allowing for translation of the solution mediated by the new parameter c at each step k:

$$\mathbf{G}(\mathbf{u}_k(x), \lambda) + c \, \partial_x \mathbf{u}_k = \mathbf{0} \tag{2.34}$$

This new parameter c remains unfixed during continuation to satisfy (2.33) [94].

2.4.2   Numerical shooting

In numerical analysis of BVP's, a BVP may be recast as an initial value problem (IVP) in which the shape of the solution profile is interpreted as a trajectory resulting from initial conditions (boundary conditions on the left side) which reaches a desired end state (boundary conditions on the right side) [96]. The shooting method uses gradient descent to find the correct initial conditions which minimize the difference between the obtained and desired end state.

For example, if we consider the second order BVP:

$$u''(x) = f(x, u(x), u'(x)), \quad u(x_0) = u_0, \quad u(x_1) = u_1 \tag{2.35}$$

Then we can let $y(x; A)$ solve the IVP:

$$u''(x) = f(x, u(x), u'(x)), \quad u(x_0) = u_0, \quad u'(x_0) = A \tag{2.36}$$

and if $u(x_1; A) = u_1$, then this u is also a solution to the starting BVP. The process of solving requires determining the value of A such that $u(x_1, A) = u_1$ [98, 96].
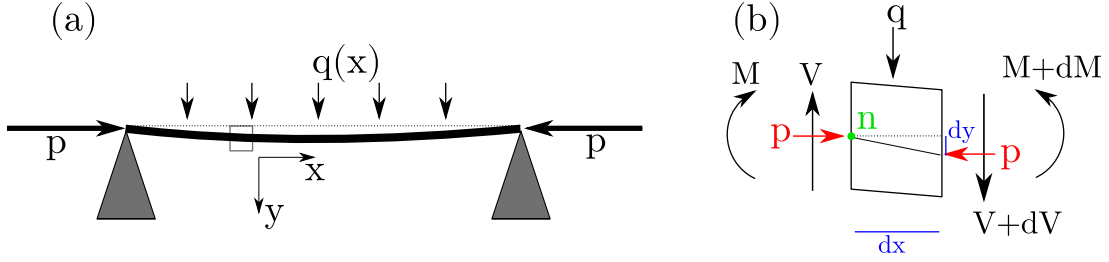
Figure 2.10: (a) Macroscopic view of a simply supported beam of length l buckling under compression p and lateral load q. (b) A microscopic view of the marked element of the beam depicting the forces and moments on an element of the beam about the point n (green dot).

2.5 Buckling

An elastic beam with endpoint supports, an applied axial compressive force p, and distributed lateral load $q(x)$ will undergo Euler column buckling as p is quasistatically varied as depicted in Fig. 2.10(a) [14].

Figure 2.10(b) depicts an infinitesimal element of the beam shown in (a). Considering the shearing force V and summing forces along the y axis, we obtain:

$$-V + qdx + (V + dV) = 0 \rightarrow q = -\frac{dV}{dx} \qquad (2.37)$$

Assuming the angle between the horizontal and the beam axis is small and considering the moments about the point n, we obtain:

$$M + qdx\left(\frac{dx}{2}\right) + (V + dV)dx - (M + dM) + pdx\frac{dy}{dx} = 0 \qquad (2.38)$$

Dropping terms of which are second order in infinitesimals, this simplifies to

$$V = \frac{dM}{dx} - p\frac{dy}{dx} \qquad (2.39)$$

If we assume that the shearing deformations of the beam axis can be neglected as second order effects, the beam axis curvature is given by

$$-M = EI\frac{d^2y}{dx^2} \qquad (2.40)$$

where EI (composed of Young's modulus and the moment of inertia respectively) provides the bending modulus of the beam in the bending (x, y) plane. Combining Eqs. (2.37,2.39,2.40), we obtain:

$$\frac{d^4y}{dx^4} + p\frac{d^2y}{dx^2} = q \qquad (2.41)$$

22

This is a fourth order equation for the vertical deflection of a buckling beam. We take the simplest possible load $q(x)$ to demonstrate the form of solutions and obtain the critical compressive force, the limiting value at which point an arbitrarily small load will induce lateral deflection exceeding the bounds of applicability imposed by our linearization. We take $q(x) = Q\delta(l/2)$, a point load at the center of the beam. Solving (2.40) on the left and right side of the load, we obtain:

$$L: EI\frac{d^2y}{dx^2} = -Q\frac{x}{2} - py \tag{2.42}$$

$$R: EI\frac{d^2y}{dx^2} = -Q\frac{l/2 - x}{2} - py\,; \tag{2.43}$$

with $k^2 = p/EI$, this has solutions

$$L: y_L(x) = A\cos(kx) + B\sin(kx) - \frac{Qx}{2p} \tag{2.44}$$

$$R: y_R(x) = C\cos(kx) + D\sin(kx) - \frac{Q}{2p}(l - x)\,. \tag{2.45}$$

The deflection at the support points is 0, so $y(0) = y(l) = 0$ requires that $A = 0$ and $C = -D\tan(kl)$. Imposing continuity and smoothness of the beam at $x = l/2$, we obtain

$$B = \frac{Q\sin(kl/2)}{pk\sin(kl)} \quad D = -\frac{Q\sin(kl/2)}{pk\tan(kl)}\,, \tag{2.46}$$

such that the solutions are given by

$$L: y_L(x) = \frac{Q\sin(kl/2)}{pk\sin(kl)}\sin(kx) - \frac{Qx}{2p} \tag{2.47}$$

$$R: y_R(x) = -\frac{Q\sin(kl/2)}{pk\tan(kl)}\sin(k(l - x)) - \frac{Q}{2p}(l - x)\,. \tag{2.48}$$

The maximum deflection occurs at $x = l/2$ and is given by

$$y(l/2) = \frac{Q}{2pk}\left(\tan\left(\frac{kl}{2}\right) - \frac{kl}{2}\right) \tag{2.49}$$

This becomes infinite when $kl = \pi$ for any nonzero Q, implying that at

$$p^* = \frac{EI\pi^2}{l^2} \tag{2.50}$$

any lateral load will produce a large vertical deflection. We call this value the critical compressive force and recognize that finite buckling amplitudes may occur at this value of p for infinitesimal perturbations q. The bifurcation of the buckled state from the trivial state in the vicinity of p^* is subcritical, comparable to the patterned state bifurcation from the trivial state in the Swift-Hohenberg equation [99].

23

Chapter 3

The models

We are interested in the cross-sectional shapes of a closed tubular membrane under external pressure and subject to a nonlinear force from a supporting substrate. In this thesis, we will take two specific models of the substrate. In the first, we consider a solid elastic support, while in the second, we consider a fluid one. Both of these models will be seen to possess the same or similar governing equations for steady state solutions despite differing physical interpretations of the constants in the equation.

An equation for in-plane deformations of the elastic interface may be derived by balancing the normal forces and the torque on an interfacial element of length ds. The normal force includes contributions from the elastica bending rigidity, imposed pressure, and substrate force. The specific details of the substrate force will be described in the following subsections. The equilibrium states of an inextensible elastic rod are described by the stationary Kirchhoff equations [100]

$$\partial_s \mathbf{F} + \left[P + \frac{1}{2} F(r) \right] \mathbf{n} = 0, \qquad \partial_s \mathbf{M} + \mathbf{t} \times \mathbf{F} = 0 \,, \tag{3.1}$$

where $\mathbf{F}$ and $\mathbf{M}$ are, respectively, the force and moment acting on the centerline of an element of the ring, $P \equiv P_i - P_o$ is the difference between interior and exterior pressures, and $F(r)/2$ is the radially dependent substrate force, and s is the arclength along the ring. We apply these equations to the closed elastic membrane to find the equilibrium solutions of the elastic membrane coupled to the solid or fluid substrate. Here $\mathbf{t} = (\cos \phi, \sin \phi)$ is the unit vector tangent to the ring at location s and $\mathbf{n} = (\sin \phi, -\cos \phi)$ is the corresponding unit normal vector pointing outwards.

Taking the moment to be proportional to the local curvature of the elastica κ, i.e. $\mathbf{M} = B\kappa\mathbf{k}$, where B is the (constant) bending modulus and $\mathbf{k}$ is normal to the plane, we note the identities:

$$\partial_s \mathbf{n} = \kappa \mathbf{t}, \qquad \partial_s \mathbf{t} = -\kappa \mathbf{n}, \qquad -\kappa \mathbf{k} = \mathbf{t} \times \partial_s \mathbf{t} \,, \tag{3.2}$$

verifiable immediately upon taking derivatives and noting that $\partial_s \phi = \kappa$. Applying Eq. (3.2) to the moment balance equation along the elastica, we obtain

$$\mathbf{t} \times (-\mathcal{B}\partial_s^2 \mathbf{t} + \mathbf{F}) = 0 \,,$$

implying that

$$\mathbf{F} = \mathcal{B}\partial_s^2\mathbf{t} + \lambda(s)\mathbf{t},$$

where $\lambda(s)$ is a Lagrange multiplier to impose inextensibility. Inserting this result into the force balance equation, we obtain

$$[-\mathcal{B}(\partial_s^2\kappa - \kappa^3) - \lambda\kappa + P + \frac{1}{2}\Delta\rho\,\Omega^2 r^2]\mathbf{n} + [-3\mathcal{B}\kappa\partial_s\kappa + \partial_s\lambda]\mathbf{t} = 0. \qquad (3.3)$$

The second bracket implies that

$$\lambda(s) = \frac{3}{2}\mathcal{B}\kappa^2 - T, \qquad (3.4)$$

where $\lambda(s)$ encodes the interface tension comprised of a curvature-dependent term and a Lagrange multiplier T required if the interface is assumed inextensible. We refer to T, for simplicity, as the tension. This quantity is determined by solving a nonlinear eigenvalue problem and quantifies the response of the system to changes in the system parameters, at fixed interface length.

Inserting this result into the first bracket in Eq. (3.3), we obtain the governing equation:

$$\mathcal{B}\left(\frac{1}{2}\kappa^3 + \partial_s^2\kappa\right) - T\kappa - P - \frac{1}{2}F(r) = 0, \qquad (3.5)$$

where the local curvature is given by $\kappa \equiv \partial_s\phi$. The geometry of the local angle ϕ, the angle between the tangent plane and the horizontal or x-axis, is detailed in Fig. 3.1. Perturbing the Cartesian coordinates (x, y) with origin at the tube center as shown,
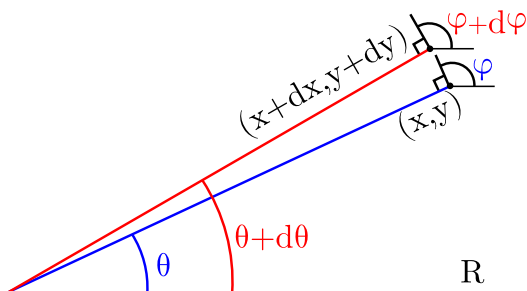
Figure 3.1: A point at coordinates (x, y) is rotated to coordinates $(x + dx, y + dy)$ following a perturbation to the local angle $\phi + d\phi$. The distance between these coordinates is spanned by an arclength ds.

we obtain:

$$x + dx = R\cos(\theta + d\theta) \text{ and } y + dy = R\sin(\theta + d\theta)$$
$$x + dx = R\left(\cos(\theta)\cos(d\theta) - \sin(\theta)\sin(d\theta)\right) \text{ and } y + dy = R\left(\sin(\theta)\cos(d\theta) + \cos(\theta)\sin(d\theta)\right)$$
$$dx = -R\sin(\theta)d\theta + \mathcal{O}\left(d\theta^2\right) \text{ and } dy = R\cos(\theta)d\theta + \mathcal{O}\left(d\theta^2\right)$$

Taking $d\theta$ to be infinitesimal, noting that $ds = Rd\theta$, and applying $\theta = \phi - \pi/2$, we obtain the relations $\partial_s x = \cos\phi$ and $\partial_s y = \sin\phi$, with $r^2(s) \equiv x^2(s) + y^2(s)$. The constants in (3.5) are the bending modulus $\mathcal{B}$ and the (unknown) baseline tension T required to maintain the length L of the lining (note that compression is indicated by $T < 0$). The imposed pressure difference P is taken as the primary parameter.

A family of forces per unit area $F(r)$ will be considered in this thesis and described below in the specific cases of a solid or fluid substrate.

3.1   Solid substrate model

To represent the lining on the inside of a soft springy tube, a minimal model for the endothelium lining of an artery coupled to layers of collagen in the tunica media [101], we consider an inextensible, infinitely thin membrane of length $L = 2\pi R$ attached to a soft substrate as shown in Fig. 3.2. We suppose that in pressure equilibrium ($P = 0$) the unlined soft tubular substrate has an inner radius $r_0 < R$ (Fig. 3.2) and hence that, when attached to the substrate as a lining, the elastic lining is forced to wrinkle.

We will consider the family of forcings $F_n(r) = K_n(r^n - r_0^n)$, $n = 0, 2, 4, 6$, intended to model several possible nonlinear substrates of stiffness K_n coupled to the membrane. This form of nonlinear force is motivated by application of the Winkler foundation model, typically framed in the case of a flat elastic beam coupled to a flat substrate in which the restoring force is taken to be a linear function of the beam/substrate displacement [102, 103]. Integrating the substrate displacement along the arclength of a thick, tubular substrate, the simplest resulting force is quadratic in the radius, making F_2 the simplest nonlinear model that can be considered. Qualitatively, this family of forces contains the physical features of the substrate we would like to model. It is zero when $r = r_0$, positive for $r > r_0$, and negative for $r < r_0$. More realistic representation of the substrate forces may be obtained by consideration of higher-order models [104] or models with nonlocal contributions [25]. For this reason, F_2 will be considered for the majority of this thesis until section 6.3 when higher order forces will be considered using analytical results developed for $n = 2$.

When the substrate force F_2 is expanded around r_0, it behaves like the classical Winkler foundation [102] with constant stiffness $K_2 r_0$. The quadratic contribution to the force vanishes as $r_0 \to \infty$ (flat-foundation limit), and a Winkler-foundation type response emerges again. The Winkler foundation model has been applied in studies of substrate-supported elastica and instabilities leading to both wrinkled and localized states [105, 29, 30].

We take $K_0 = 0$, where this problem reduces to the buckling of a tubular elastic membrane without any substrate present. For $n = 2, 4, 6$, the forcing may be provided by a solid overcompressed exterior elastic substrate or an overextended interior elastic substrate as shown in Fig. 3.2. Inserting this forcing, the governing equation for steady

state solutions becomes:

$$\mathcal{B}\left(\frac{1}{2}\kappa^3 + \partial_s^2\kappa\right) - T\kappa - P - \frac{1}{2}K_n(r^n - r_0^n) = 0\,. \tag{3.6}$$

The duality between interior and exterior substrate placement is due to the symmetry $(\kappa, P, K_n) \to (-\kappa, -P, -K_n)$ in Eq. (3.6).
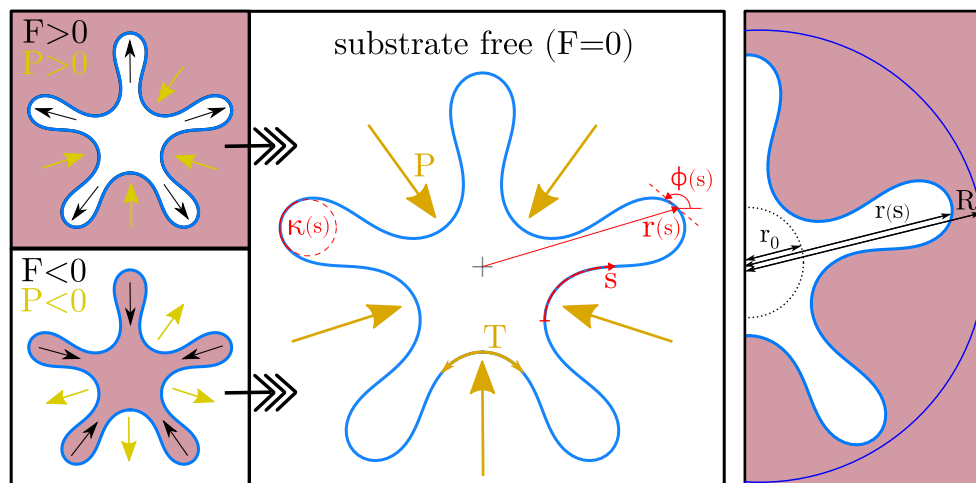
Figure 3.2: The solution profiles $\mathbf{r}(s)$ are shown in blue. Left panel: competition between pressure and substrate forces arising from external (top) or internal (bottom) support leads to a nontrivial critical wrinkle wavenumber $m = 5$. Center panel: the substrate-free ($F = 0$) case leads to the same buckled state with $m = 5$ but for different system parameters. Right panel: the undercompression of the substrate, seeking to relax to r_0, but resisted by the membrane to a position $r(s)$. Uncompressed membrane shown at $r(s) = R$. The problem variables are shown in the center panel.

The resting substrate radius term r_0 will be folded into the pressure term going forward when considering the solid support model. We are interested in understanding the properties of the equilibrium states in this system as either the substrate stiffness or membrane bending modulus changes for a given pressure difference P, or as P varies for a fixed substrate stiffness.

3.2   Fluid substrate model

For our second example described by Eq. (3.5), we consider a Hele-Shaw cell with a fluid of density ρ_i surrounded by a fluid of density ρ_o and separated from it by a closed, elastic membrane of length $L = 2\pi R$ and bending modulus $\mathcal{B}$, assumed to be independent of the curvature (Fig. 3.3). The system rotates with constant angular
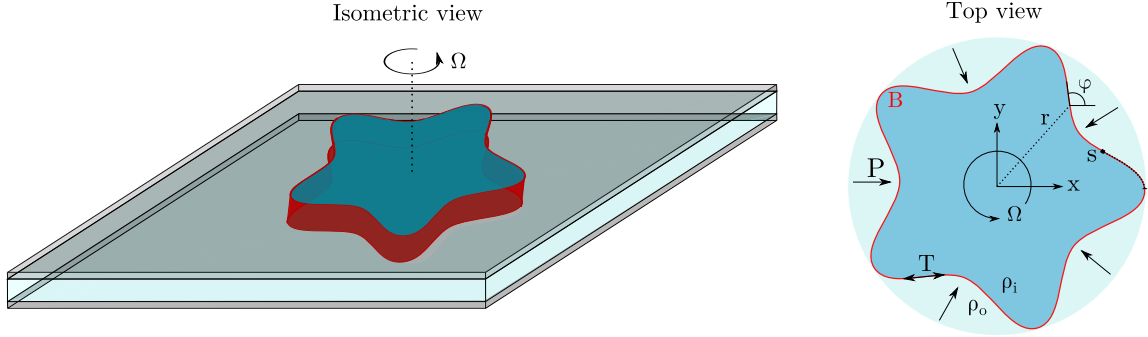
Figure 3.3: A rotating Hele-Shaw cell containing two fluids of densities ρ_i and ρ_o separated by an elastic membrane (red) wrinkled with wavenumber $m = 5$ (left) together with a schematic top view (right). The interface is parametrized by arclength s, with $(x(s), y(s))$ providing a parametric representation of the interface profile.

velocity Ω about an axis perpendicular to the cell at $\mathbf{r} = 0$. In equilibrium, the inner liquid occupies a circular region with the axis of rotation at its center. Inserting the centrifugal force due to the rotation and density difference, the substrate force is given by centrifugal term $F(r) = \Delta\rho\Omega^2 r^2$, and the governing equation is therefore:

$$\mathcal{B}\left(\partial_s^2\kappa + \frac{1}{2}\kappa^3\right) - T\kappa - P - \frac{1}{2}\Delta\rho\,\Omega^2 r^2 = 0\,. \tag{3.7}$$

The perturbed interface is parametrized with the arclength s such that the curvature of the interface at location s or equivalently at $\mathbf{r}(s) = (x(s), y(s))$ relative to the origin is given by $\kappa = \partial_s\phi$, where $\phi(s)$ is the angle between the tangent to the interface at point s and the x axis (Fig. 3.3) as before. The density difference $\Delta\rho \equiv \rho_i - \rho_o > 0$ is defined between the interior and exterior fluids, and a pressure difference $P \equiv P_i - P_o$ is imposed between them. A baseline tension T in the elastica is required to maintain its inextensibility. We call the resulting problem the *constrained length* problem. In contrast, when T is set to zero the length of the interface is unconstrained, and we call the resulting problem the *unconstrained length* problem. Both forms of the problem exhibit steady state solutions. Since we solely consider steady states of the rotating two-fluid Hele-Shaw system in this section, and such states are not accompanied by fluid flow, the results are independent of viscosity.

3.3   Membrane extensibility

The two limits we consider, a perfectly inextensible and a perfectly extensible membrane, are expected to bracket more realistic models. In fact, the inextensible limit is a good approximation for a wide variety of materials. The inextensible limit has been applied to many problems spanning biology and physics with good qualitative

agreement found between predictions and results [5, 39, 104]. In particular, the inextensible limit appears to be appropriate for biological materials described by the Ogden-Gasser-Holzapfel model where good agreement has been found between results that assume inextensibility and more realistic FEM-based computations [101]. Similar problems have approached the length constraint from an alternative angle by considering the effect of growth on a filament connected to a rigid substrate via an array of springs. In this case, imposed growth strain leads to periodic and localized deformations of the filament which are qualitatively consistent with the results presented in our paper [30, 29]. The freely extensible case may occur in the Hele-Shaw situated system in which the interface between the two fluids occurs as a result of a chemical reaction between the two fluids or simply due to their immiscibility [44]. For this reason, we consider the freely extensible limit solely in the case where the interface occurs between two fluids and not for the solid substrate.

Chapter 4

Solid substrate: $n = 2$

We construct an idealised two-dimensional model for this class of tubular wrinkling systems and compute strongly deformed states up to the point of self-contact, analyse their stability, and organise the results in the form of bifurcation diagrams. These diagrams describe the response of the system (compression, tension, maximum curvature) as a function of a control parameter, for example, the imposed pressure difference. We use the results to identify a transition from unwrinkled to periodic wrinkled states and then to folded states similar to what is observed in spring-loaded linings or tubular chitosan hydrogel surfaces [30, 106]. Fold states arise via secondary bifurcations from the wrinkled state as in the one-dimensional case. Two cases are considered in detail, one with prominent wrinkling and a second one in which wrinkling is absent and only buckling remains.

Considering Eq. (3.6) for $n = 2$, we define the natural length scale

$$\lambda \equiv \left(\frac{\mathcal{B}}{K_2}\right)^{\frac{1}{5}}, \tag{4.1}$$

and introduce a dimensionless parameter that measures the perimeter of the lining in terms of λ, $\ell \equiv R/\lambda$. It is noteworthy that an initially flat system comprised of an elastic membrane (bending stiffness $\mathcal{B}'$) bound to an elastic foundation (stiffness K') under uniaxial load (a fourth order problem) possesses a natural wavelength $\lambda' = (\mathcal{B}'/K')^{1/4}$ [5]. Equation (3.7) may be rescaled according to

$$s \sim R, \ \kappa \sim R^{-1}, \ r \sim R, \ T \sim \mathcal{B}/R^2, \ P \sim \mathcal{B}/R^3, \tag{4.2}$$

to obtain the complete fifth order problem in its simplest form:

$$\partial_s^3 \phi + \frac{1}{2}(\partial_s \phi)^3 - T\partial_s \phi - P - \frac{1}{2}\ell^5 r^2 = 0, \tag{4.3}$$
$$\partial_s x = \cos(\phi),$$
$$\partial_s y = \sin(\phi).$$

The tension is an immediate measure of the system response, but it will be useful to define additional system response metrics as functionals of the spatial profile. Stokes theorem can be used to write the area within the lining, rescaled relative to the area of the unperturbed circle, as:

$$S[\phi(s)] = \frac{1}{2\pi R} \oint [x \sin\phi - y \cos\phi] \, \mathrm{d}s, \qquad (4.4)$$

such that its fractional compression is $\Delta \equiv 1 - S$. The total energy, also rescaled relative to the circle, is given by two terms:

$$E[\phi(s)] = \frac{2}{\pi(4 + \ell^5)} \oint \left[(\partial_s \phi)^2 + \frac{1}{4}\ell^5 r^2 (x \sin\phi - y \cos\phi) \right] \mathrm{d}s, \qquad (4.5)$$

The first term results from the energy stored in the bending of the membrane, while the second term comes from the energy stored in the extension of the substrate.

We note that the solid substrate system has the same governing equation as the rotating fluid filled Hele-Shaw cell system in the case $n = 2$ and $r_0 = 0$ although the physical interpretations of the substrate force terms are different [58, 59, 65].

4.1   Linear and weakly nonlinear theory

The simplest solution to (4.3) is the circle:

$$\phi_0(s) = s, \quad x_0(s) = \sin s, \quad y_0(s) = -\cos s. \qquad (4.6)$$

This solution immediately implies a linear relationship between the imposed pressure and the resulting tension:

$$T_0 = \frac{1}{2}(1 - \ell^5) - P_0, \qquad (4.7)$$

and serves as the starting solution about which to construct a linear and weakly nonlinear analysis. Introducing a small parameter ϵ measuring the amplitude of a perturbation of the circle solution, we expand the solution (ϕ, x, y), and parameters (T, P) as follows:

$$\phi(s) = \sum_{j=0}^{N} \epsilon^j \phi_j(s), \quad x(s) = \sum_{j=0}^{N} \epsilon^j x_j(s), \quad y(s) = \sum_{j=0}^{N} \epsilon^j y_j(s), \qquad (4.8)$$

$$T = \sum_{j=0}^{N} \epsilon^{2j} T_{2j}, \quad P = \sum_{j=0}^{N} \epsilon^{2j} P_{2j}. \qquad (4.9)$$

Half wavelength rotations of wrinkled solutions are equivalent to the transformation $(\epsilon \to -\epsilon)$. Due to this invariance of the system, the coefficients of odd powers of ϵ in P and T vanish because a spatial rotation cannot physically result in a shift in pressure or tension. Substituting these expansions into (5.2) and the equations for x and y leads to a linear problem of the form

$$\mathcal{L}[\phi_j, x_j, y_j] \equiv \partial_s^3 \phi_j + \left(\frac{3}{2} - T_0 \right) \partial_s \phi_j - \ell^5 (x_0 x_j + y_0 y_j) = \mathcal{N}_j,$$

at each order in the weakly nonlinear analysis, $j = 1, 2, 3...$, with the first three $\mathcal{N}_j$ given by

$$\mathcal{N}_1 = 0$$

$$\mathcal{N}_2 = -\left(\frac{3}{2}(\partial_s\phi_1)^2 + \frac{1}{2}\ell^5(x_1^2 + y_1^2) - P_2 - T_2\right)$$

$$\mathcal{N}_3 = -\left(\frac{1}{2}(\partial_s\phi_1)^3 + 3(\partial_s\phi_1)(\partial_s\phi_2) + \ell^5(x_1x_2 + y_1y_2)\right) + T_2\partial_s\phi_1.$$

The above problem is nonautonomous and analytically challenging due to the presence of the (x, y) terms. However, geometric identities of planar curves may be exploited to generate an equivalent autonomous problem which is more analytically tractable. To eliminate x_j and y_j from $\mathcal{L}[\phi_j, x_j, y_j]$, we compute $(\partial_s^2\mathcal{L} + \mathcal{L})[\phi_j, x_j, y_j]$:

$$\partial_s^5\phi_j + \left(\frac{5}{2} - T_0\right)\partial_s^3\phi_j + \left(\frac{3}{2} - T_0\right)\partial_s\phi_j + \ell^5\left[2(\partial_s x_0)(\partial_s x_j) + 2(\partial_s y_0)(\partial_s y_j) + x_0\partial_s^2 x_j + y_0\partial_s^2 y_j\right]$$

$$= (\partial_s^2 + 1)\mathcal{N}_j. \tag{4.10}$$

Expansions of the geometric identities $\partial_s x = \cos\phi$ and $\partial_s y = \sin\phi$ now results in

$$\partial_s^5\phi_j + \left(\frac{5}{2} - T_0\right)\partial_s^3\phi_j + \left(\frac{3}{2} - T_0 + \ell^5\right)\partial_s\phi_j = \mathcal{G}_j + (\partial_s^2 + 1)\mathcal{N}_j, \tag{4.11}$$

where the first three $\mathcal{G}_j$ are given by

$$\mathcal{G}_1 = 0$$

$$\mathcal{G}_2 = \frac{1}{2}\ell^5(\partial_s\phi_1)^2$$

$$\mathcal{G}_3 = \ell^5\left(\frac{1}{2}\phi_1^2\partial_s\phi_1 - \phi_1\phi_2\right).$$

such that the problem is autonomous and remains homogenous for $j = 1$.

Solving (4.11) order by order for $j = 1, 2, 3, ...$ subject to the requirement that the solution is periodic yields expressions for (ϕ_j, x_j, y_j), and parameters (T_j, P_j).

For $j = 1$, the problem 4.11 is given by:

$$\partial_s^5\phi_1 + \left(2 + P_0 + \frac{\ell^5}{2}\right)\partial_s^3\phi_1 + \left(1 + P_0 + \frac{3\ell^5}{2}\right)\partial_s\phi_1 = 0.$$

This equation reduces to an algebraic equation on assuming that $\phi_1(s) \propto C_1 + A_1\sin(ms)$:

$$m^5 - \left(2 + P_0 + \frac{\ell^5}{2}\right)m^3 + \left(1 + P_0 + \frac{3\ell^5}{2}\right)m = 0, \tag{4.12}$$
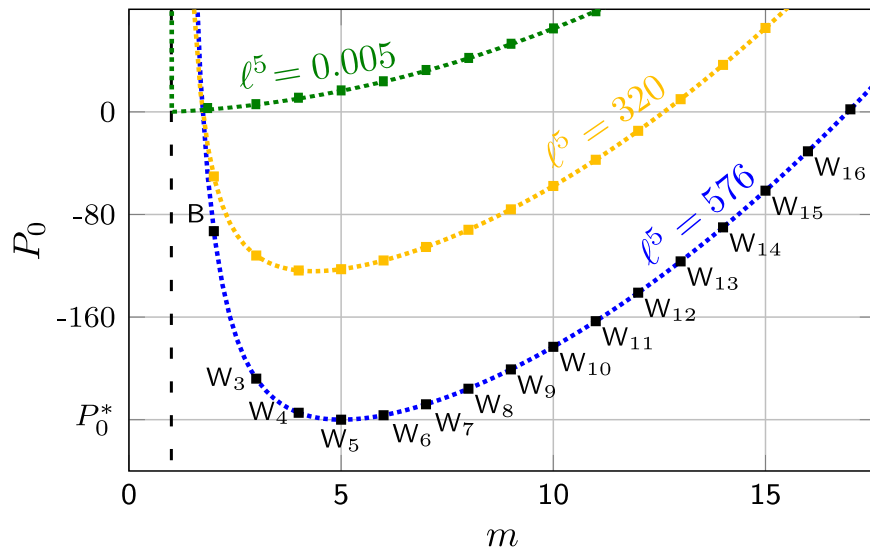
Figure 4.1: The wrinkle wavenumber m as a function of the pressure P_0 for $\ell^5 = 576$ (blue curve, $m^* = 5$), $\ell^5 = 320$ (yellow curve, $m^* = 4$) and $\ell^5 = 0.005$ (green curve, $m^* = 2$). $L = 2\pi$, so the two largest $\ell^5 = 576$ values have been chosen to yield integer wavenumbers at onset.

where m must be an integer to satisfy closure requirements and $m \geq 2$ since the dilation mode is eliminated by the length constraint. These solutions correspond to periodic states we refer to as wrinkles (W_m); C_1 corresponds to a rigid rotation of the solution, so we can set $C_1 = 0$ as a choice of phase. Thus

$$\phi_1 = \sin(ms), \tag{4.13}$$

$$x_1 + iy_1 = \frac{m\cos(ms) - i\sin(ms)}{m^2 - 1} \exp(is). \tag{4.14}$$

Equation (4.12) determines the critical pressure P_0^* for the onset of the wrinkling instability as the pressure difference increases and the wavelength of the resulting wrinkles for a given ℓ^5. Figure 4.1 depicts P_0 as a function of m for three different ℓ^5 values. The figure shows how the circular tube depressurizes and becomes wrinkled as P_0 overcomes the threshold $P_0^* \equiv (-\ell^5 + 4\ell^{5/2})/2$. It also shows how the choice of ℓ^5 determines the order of appearance of new unstable wavenumbers. The critical wavenumber at P_0^* is obtained via $\partial P/\partial m = 0$, yielding the simple equation:

$$m^* = \sqrt{1 + \sqrt{\ell^5}}. \tag{4.15}$$

When $\ell^5 < 9$ the onset wavenumber is $m^* = 2$ since $m = 1$ corresponds to translations (Fig. 4.1). The critical pressure difference may also be rewritten in terms of the original, non-rescaled terms to facilitate physical predictions for wrinkling onset,

33

yielding:

$$\tilde{P}_0^* = \frac{1}{2}K\left(r_0^2 - R^2\right) + 2\left(\frac{\mathcal{B}K}{R}\right)^{1/2}. \tag{4.16}$$

This relates the physical properties of the lining, the substrate, and the geometry of the tube to the critical pressure for wrinkling. It also indicates that the critical pressure can be tuned via suitable choices of material properties such as r_0 and R in order to generate wrinkles even at ambient pressure when $P_0 = 0$ (for example, as shown in Fig.1.1(b)). Physically, this can be shown to require that the total membrane length is greater than the relaxed substrate interior perimeter (i.e. $r_0 < R$), which follows immediately from Eq. (4.16).

Continuing from the linear results to higher order, for $j = 2$, Eq. (4.11) becomes

$$\begin{aligned}
\partial_s^5\phi_2(s) &+ \frac{(l^5 + m^4 - 1)}{m^2 - 1}\partial_s^3\phi_2(s) + \frac{m^2(l^5 + m^2 - 1)}{m^2 - 1}\partial_s\phi_2(s) \\
&= \frac{P_2 m^4 - 2P_2 m^2 + P_2 + T_2 m^4 - 2T_2 m^2 + T_2}{m^4 - 2m^2 + 1} \\
&+ \frac{-0.25l^5 m^4 + 0.75l_5 m^2 - 0.75m^6 + 1.5m^4 - 0.75m^2}{m^4 - 2m^2 + 1} \\
&+ \frac{3m^2\left(-l_5 + 4m^4 - 5m^2 + 1\right)}{4\left(m^2 - 1\right)}\cos(2ms).
\end{aligned} \tag{4.17}$$

The constant coefficient right hand side terms must be zero following the Fredholm alternative theorem due to the form of the solution to the homogenous problem for $j = 1$. Having chosen P_2 as a function of T_2

$$P_2(T_2) = \frac{-T_2 m^4 + 2T_2 m^2 - T_2 + 0.25l^5 m^4 - 0.75l^5 m^2 + 0.75m^6 - 1.5m^4 + 0.75m^2}{m^4 - 2m^2 + 1}, \tag{4.18}$$

to eliminate the unwanted constant coefficient term on the right hand side, the equation takes the form:

$$a_2\partial_s^5\phi_2 + b_2\partial_s^3\phi_2 + c_2\partial_s\phi_2 = 0 + E_2\cos(2ms). \tag{4.19}$$

The coefficient $\cos(2ms)$ suggests the ansatz $\phi_2 = A_2\sin(2ms)$, which yields:

$$(a_2(2m)^5 + b_2(2m)^3 + c_2(2m))A_2 = E_2, \tag{4.20}$$

which may be solved for A_2 to obtain:

$$\begin{aligned}
\phi_2 &= \frac{1}{8m}\sin(2ms), \\
x_2 + iy_2 &= \left[-\frac{1}{4} + \frac{i}{8m}\sin(2ms)\right]\exp(is).
\end{aligned}$$

34

For $j = 3$, we obtain:

$$
\partial_s^5 \phi_3(s) + \frac{(l^5 + m^4 - 1)}{m^2 - 1} \partial_s^3 \phi_3(s) + \frac{m^2 (l^5 + m^2 - 1)}{m^2 - 1} \partial_s \phi_3(s)
$$
$$
= \left(\frac{m \left(8 P_2 m^4 - 16 P_2 m^2 + 8 P_2 - 2 l^5 m^4 + 9 l^5 m^2 - 3 l^5 - 3 m^6 + 9 m^4 - 9 m^2 + 3\right)}{8(m^2 - 1)} \right) \cos(ms)
$$
$$
+ \left(\frac{m \left(-l^5 m^2 - 3 l^5 + 9 m^6 + 17 m^4 - 29 m^2 + 3\right)}{8(m^2 - 1)} \right) \cos(3ms). \tag{4.21}
$$

The prefactor of $\cos(ms)$ is set to zero following the solvability conditions to obtain P_2 independent of T_2:

$$
P_2 = \left[\frac{(2 l^5 m^4 - 9 l^5 m^2 + 3 l^5 + 3 m^6 - 9 m^4 + 9 m^2 - 3)}{8(m^4 - 2 m^2 + 1)} \right]. \tag{4.22}
$$

such that (T_2, P_2) may now be written independently. We are left with an equation of the form:

$$
a_3 \partial_s^5 \phi_3 + b_3 \partial_s^3 \phi_3 + c_3 \partial_s \phi_3 = E_3 \cos(3ms), \tag{4.23}
$$

so under the ansatz $\phi_3 = A_3 \sin(3ms)$, we have

$$
(a_3 (3m)^5 + b_3 (3m)^3 + c_3 (3m)) A_3 = E_3, \tag{4.24}
$$

which may be solved for A_3 to obtain:

$$
\phi_3 = \frac{(m^2 + 3)}{192 m^2} \sin(3ms). \tag{4.25}
$$

The spatial coordinates (x_3, y_3) follow immediately, and (T_2, P_2) are given by:

$$
P_2 = \frac{2 m^4 - 9 m^2 + 3}{8 (m^2 - 1)^2} \ell^5 + \frac{3 (m^2 - 1)}{8},
$$
$$
T_2 = \frac{3}{8 (m^2 - 1)} \ell^5 + \frac{3 (m^2 + 1)}{8}.
$$

(T_2, P_2) are the first correction to the (T_0, P_0) values for the circle state and therefore determine the slope $\partial P / \partial T$ of the primary wrinkle branches at the bifurcation points given by (4.12):

$$
\frac{P_2}{T_2} = \frac{3}{8} \left((m^2 - 1) + \ell^5 \frac{\frac{2}{3} m^4 - 3 m^2 + 1}{(m^2 - 1)^2} \right). \tag{4.26}
$$

This slope is always positive unless $m = 2$ and $\ell^5 \geq 81$. The mode $m = 2$ is special, because of its maximum wavelength; this mode is the first one to emerge in the absence of the intrinsic scale ℓ [70], and we therefore refer to it as the buckling mode (B).

The process of solving order by order continues analogously at higher orders. For j even, the solvability condition imposed on $\mathcal{G}_j + (\partial_s^2 + 1)\mathcal{N}_j$ generates $P_j(T_j)$, while for j odd, it generates $T_{j-1}(m, \ell^5)$. Higher order expressions were obtained through symbolic calculations using Sympy and Maple. Truncations of these results are presented below

$$\phi = s + \epsilon \sin(ms) + \epsilon^2 \frac{\sin(2ms)}{8m} + \epsilon^3 \frac{(m^2 + 3)\sin(3ms)}{192m^2}$$
$$+ \epsilon^4 \frac{\sin(2ms)(\cos(2ms)m^2 + 5m^2 + \cos(2ms) - 1)}{256m^3}$$
$$+ \epsilon^5 \frac{(m^4 + 18m^2 - 3)\sin(3ms) + \sin(5ms)\left(\frac{m^4}{5} + 2m^2 + 1\right)}{4096m^4}$$
$$+ \epsilon^6 \frac{\sin(2ms)\left(\left(m^4 + \frac{10}{3}m^2 + 1\right)\cos(2ms)^2 + (6m^4 + 12m^2 - 2)\cos(2ms) + \frac{109m^4}{4} - \frac{83m^2}{6} + \frac{5}{4}\right)}{8192m^5}$$
$$+ \mathcal{O}(\epsilon^7). \tag{4.27}$$

$$T = \frac{\alpha_2}{(m-1)(m+1)} - m^2 + \frac{3}{2}$$
$$+ \left(\frac{3}{8}(m^2 + 1) - \frac{3\alpha_2}{(8(m-1))(m+1)}\right)\epsilon^2$$
$$+ \left(\frac{3\alpha_2(3m-1)(3m+1)}{512(((m-1)(m+1))m^2)} + \frac{3(m^4 + 22m^2 + 1)}{512m^2}\right)\epsilon^4$$
$$+ \left(\frac{3(5m^6 + 371m^4 + 43m^2 - 3)}{32768m^4} - \frac{9\alpha_2(3m^2 + 1)(5m^2 - 1)}{32768(((m-1)(m+1))m^4)}\right)\epsilon^6 + \mathcal{O}(\epsilon^8) \tag{4.28}$$

$$P = \frac{\alpha_2(m^2 - 3)}{2((m-1)(m+1))} + (m-1)(m+1)$$
$$+ \left(\frac{3}{8}(m-1)(m+1) - \frac{\alpha_2(2m^4 - 9m^2 + 3)}{8((m-1)^2(m+1)^2)}\right)\epsilon^2$$
$$+ \left(\frac{\alpha_2(24m^6 - 107m^4 + 54m^2 - 3)}{512((m^2(m-1)^2)(m+1)^2)} + \frac{3(m-1)(m+1)(15m^2 + 1)}{512m^2}\right)\epsilon^4$$
$$+ \left(\frac{9(m-1)(m+1)(21m^2 - 1)(3m^2 + 1)}{32768m^4} - \frac{\alpha_2(146m^8 - 641m^6 + 115m^4 + 69m^2 - 9)}{32768((m^4(m-1)^2)(m+1)^2)}\right)\epsilon^6$$
$$+ \mathcal{O}(\epsilon^8) \tag{4.29}$$

It is noteworthy that this solution is independent of the key parameter α_2 at every order computed for $n = 2$ (verified out to order ϵ^{12}). Further, the dependence of P and T on α_2 is linear at every order computed. The implications of these observations will be considered in greater detail in section 6 to motivate a search for exact solutions.

36

In the following we extend the above results using numerical continuation, the primary method for which is described in the next section.

4.2 Numerical continuation: method

Equation (4.3) is implemented in AUTO, a numerical continuation software package using pseudo-arclength continuation for bifurcation problems in ordinary differential equations (ODE's) [95]. The equations may be written as a nonlinear boundary value problem and implemented in AUTO as a 5-dimensional dynamical system in s encompassing the third order ODE for ϕ and the two first order ODEs for (x, y). For the constrained length sections of this paper, we construct the problem on the domain $s \in [0, \pi]$, representing half of a closed elastic interface of length 2π, subject to the boundary conditions

$$\phi(0) = \pi/2, \quad \phi(\pi) = 3\pi/2, \tag{4.30a}$$

$$x(0) = x_0, \quad x(\pi) = x_1, \tag{4.30b}$$

$$y(0) = y(\pi) = 0, \tag{4.30c}$$

$$\partial_s^2\phi(0) = \partial_s^2\phi(\pi) = 0. \tag{4.30d}$$

The final two conditions require the elastica endpoints are locations experiencing zero normal force such that the half-domain boundary conditions do not add any additional stresses to the system beyond what a full-domain solution would experience [35, 66]. This condition results from the moment equation of (3.1) with the constitutive equation $\boldsymbol{M} = \mathcal{B}\partial_s\phi\boldsymbol{k}$:

$$\partial_s\boldsymbol{M} + \boldsymbol{t} \times \boldsymbol{F} = 0 \implies \mathcal{B}\partial_s^2\phi = \boldsymbol{F} \cdot \boldsymbol{n} \tag{4.31}$$

These boundary conditions ensure that a smooth full circle solution can be generated via reflection of a half domain solution about the x axis.

For the unconstrained length sections, $s \in [0, L/2]$, where L is free to vary. Since the system is 5-dimensional with 8 boundary conditions, numerical continuation is performed in the four parameters (P, T, x_0, x_1) for the constrained length problem and (P, L, x_0, x_1) for the unconstrained length problem [107], i.e., for a given change in P, the new tension T (or L) is found as a nonlinear eigenvalue of the problem, while x_0, x_1 are adjusted to satisfy the force-free boundary conditions.

The boundary conditions (4.30) impose a reflection symmetry on all the solutions generated by the above procedure and so prevent the computation of states that break this symmetry. This is useful because it eliminates the continuous rotation symmetry of all full domain solutions and makes continuation much more straightforward. Since nonsymmetric states are nonetheless expected to be present [65], an alternative

approach to continuation of the above problem is taken in Sec. 5.10 that permits the computation of such solutions.

The results of this procedure have been carefully compared to those from the high order weakly nonlinear analysis and are found to be in excellent agreement as shown in Fig. 4.4 and Table 4.1 [66]. The nonlinear results have also been validated by matching to the exact analytical solutions obtained in section 6 to within numerical tolerance [83]. Self-contact forces can be included in order to continue solutions beyond our current range [70, 71], but we do not do so in this paper. Self-intersecting solutions are not shown.

4.3 Numerical continuation: $\ell^5 = 576$

With the implementation described in the previous section, we performed numerical continuation in AUTO with Eqs. 5.2,4.30 defining a BVP. The numerical continuation was initiated with a circular profile, an initial choice of P, $\ell^5 = 576$ chosen such that the critical wavenumber is $m^* = 5$, and tension T determined by Eq. 4.7 as a function of ℓ^5 and P. As predicted by linear theory, circular profile states fall along a straight line in the (T, P) plane, with the tension T increasing to resist dilation of the profile and maintain the length constraint on the elastica as the internal pressure increases relative to the external pressure, i.e. as P drops. In each step of continuation in the primary parameter P requires the continuation to provide a new response T as the solution to a nonlinear eigenvalue problem.

Due to this implementation, the (P, T) formulation provides the natural framework for numerical continuation. Figure 4.2 shows a bifurcation diagram depicting the baseline tension T as the system response to an imposed pressure difference P.

Primary branches of wrinkling solutions bifurcate from the circle branch with wavenumber and onset pressure difference exactly matching the results of Eqs. 4.12 for $\ell^5 = 576$. These wrinkling profiles grow more nonlinear as P increases with the exception of $m = 2$ which becomes more nonlinear as P decreases, a classic buckling response. The continuation-based approach also allows for the computation of secondary branches of mixed modes (M) and folds (F).

An additional measure of the system response is detailed in Figure 4.3 which shows the compression Δ (cf. Eq. 4.4) as a function of the imposed pressure difference P. The figure shows the pressure difference required for collapse of the initial circular cross section to set in (corresponding to the primary bifurcations at $\Delta = 0$) but also the subsequent response to quasistatic increases in P, i.e., the figure displays the tube law describing the mechanical response of different instability modes for the parameter choice $\ell^5 = 576$.

Both figures show primary wrinkle states W_m with different wavenumbers m, beginning with W_5 which corresponds to the onset wavenumber $m^* = 5$. They also depict a number of secondary branches (the mixed states M and the fold states
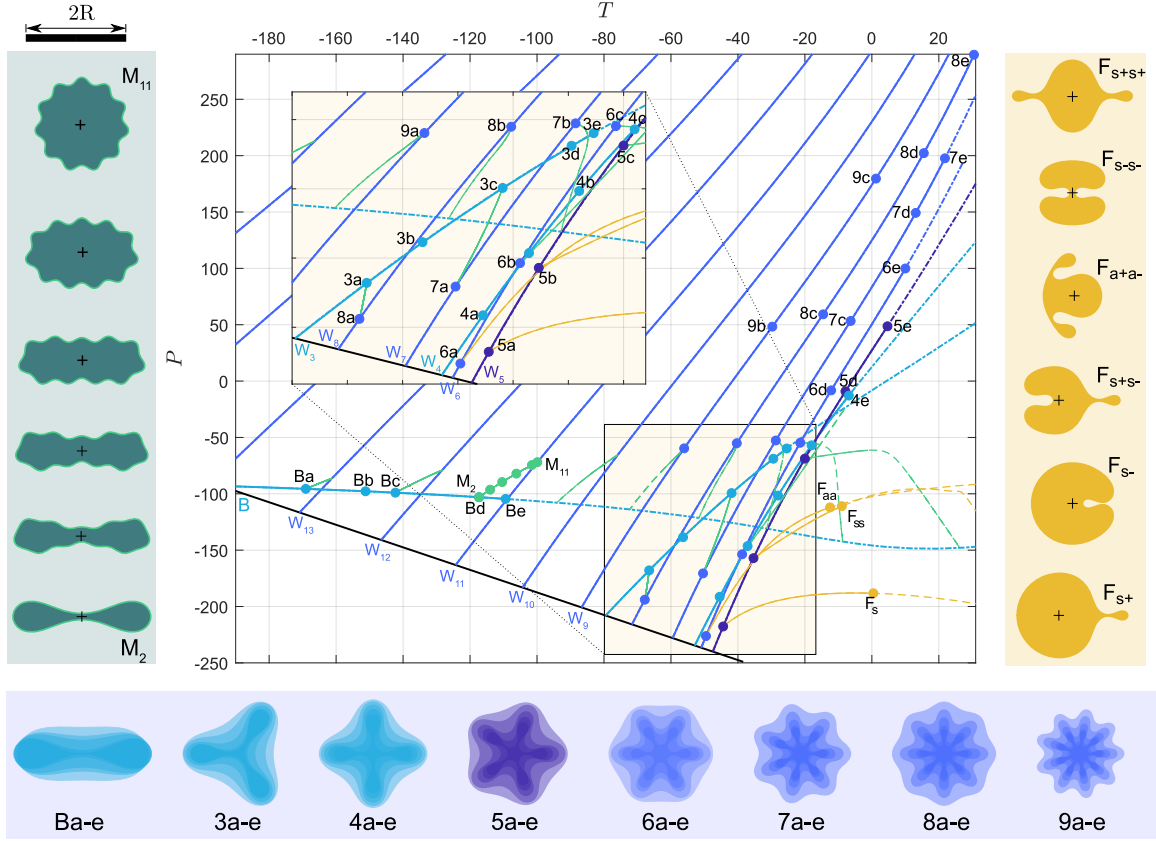
Figure 4.2: Bifurcation diagram for $\ell^5 = 576$ (corresponding to $m^* = 5$) showing the tension T resulting from an imposed pressure difference P. The black line corresponds to the circle solution (4.7); the primary branch W_5 corresponding to the critical wavenumber state is shown in purple. Subsequent primary wrinkle solutions W_m are labeled by their wavenumber ($m < 5$, cyan; $m > 5$, blue), while the secondary solutions are labeled F (fold, gold) or M (mixed mode, green). The letter B labels the buckling mode $m = 2$. Branches are presented up to the point of self-contact. Sample solutions at the locations indicated in the main plot are shown alongside with the different wrinkle profiles for each m superposed. All solutions are reflected across the x axis. The mixed mode branches extend between M_{m_1,m_2} where m_1 indicates the primary wavenumber and m_2 the new wavenumber introduced at the secondary bifurcation. The subscripts $\pm$ on F refer to the folded states with an extrusion ($+$) or intrusion ($-$). The subscripts s and a indicate whether these protrusions occur on the axis or off it. A diameter length scale bar is shown on the upper left. The inset shows the bifurcation diagram with more detail in the vicinity of the bifurcation of the m^* mode. An animation of the solutions along many of the solution branches in this figure is provided in the Supplementary Material.

F) that bifurcate from the W states, together with sample solution profiles at the locations indicated in the figures. Each W_m branch ultimately reaches a point of self-contact, beyond which point the continuation is terminated. Self-contact forces can be included following [70, 71], see also [37, 108], but this has not been implemented in this thesis.

The circle solution (black line in Fig. 4.2, $\Delta = 0$ in Fig. 4.3) exists for any pressure difference P; however, primary branches W_m of wrinkle states with different integer wavenumbers m only exist above the critical pressure P_0^*. The onset ordering of wrinkle states is determined by ℓ^5 following linear theory. Wrinkle solutions with wavenumbers below m^* are interspersed with those above m^*; the wavenumber of the former decreases as P increases until $m = 2$; beyond this point m increases monotonically with the pressure difference P and only wrinkle solutions with wavenumbers above m^* are present. This result is physically significant; it indicates that ℓ^5, and specifically a nonzero substrate strength, is the parameter responsible for mixing the onset order of wrinkling branches. The branch with $m = 2$ is the first to set in when a substrate is absent ($\ell^5 = 0$) and is therefore referred to as the buckling mode. Additionally, the pressure difference required to support a stationary state drops as the state becomes more nonlinearly deformed for suitably large ℓ^5, a classic buckling response. When m^* is not an integer, the primary instability corresponds to the integer m nearest to m^* provided $m^* \geq 2$. Figure 4.3 shows that the compression Δ is almost proportional to the applied pressure P for all the wrinkle modes up until the solutions become strongly nonlinear, i.e., that the modulus $Y \equiv \partial P/\partial \Delta$ is approximately constant.

Having constructed the bifurcation diagram and solutions numerically, the weakly nonlinear results for the wrinkled solutions may now be compared to the numerics. In Fig. 4.4, we compare the results from numerical continuation of (4.3) with boundary conditions (4.30) and the corresponding results obtained above from weakly nonlinear theory carried out to $\mathcal{O}(\epsilon^{13})$.

The ϵ values corresponding to the maximum displayed extent of each branch are summarized in table 4.1. The results demonstrate excellent agreement between perturbation theory and the numerically exact solutions for $\epsilon \lesssim 1$. Equally good agreement is found for the solution profiles, even for strongly nonlinear states reaching self-contact.

Table 4.1: Wavenumber m and maximum ϵ used in Fig. 4.4.

m	2	3	4	5	6	7	8	9	10	11	12	13	14
$\epsilon_{\max}$	1.96	1.54	1.32	1.17	1.25	1.29	1.35	1.37	1.37	1.25	1.18	1.04	0.96

As mentioned previously, numerical continuation produces two forms of secondary branches. Most commonly, secondary branches connect two wrinkling branches: one primary branch with an $m \geq m^*$ mode and the other primary branch with an $m < m^*$ mode. We call this secondary state a mixed mode. Figures 4.2 and 4.3 show

several intermediate solutions along the mixed mode branch connecting the primary branches $m = 11$ and $m = 2$ with nonzero amplitudes for wavenumbers $m = 2$ and $m = 11$. Many mixed mode branches also include self-intersecting states when one of the primary branches involved is beyond the point of self-contact. The number of connections between W branches increases with ℓ^5, as the number of branches above and (more significantly) below m^* grows (due to m^* increasing with ℓ^5), and more physically realizable mixed mode branches become possible.

Not all secondary branches from wrinkling state branches connect two primary modes; some secondary branches emerge from a primary branch and extend to regions of high T where no primary branches exist. These correspond to localized states called folds and always come in pairs with varying permutations of intrusions and extrusions (within the subset of symmetric solutions). The first pair of this class of secondary bifurcation yields a single spatially localized extrusion F_{s+} and a single spatially localized intrusionF_{s-}, both bifurcating from W_5. Both branches follow the same path in the (T, P) plane and reach self-contact at similar but distinct points. Additional pairs of secondary branches of this type bifurcate from $m \geq m^*$ and feature multiple folds on the domain (see e.g. F_{s+s-} in Figs. 4.2 and 4.3). These multifold states are analogous to those found in similar planar buckling systems [23]. A family F_a of asymmetric folds is also expected, but these states generically cannot be constructed by AUTO due to the symmetries imposed by our choice of boundary conditions. These states are discussed in Sec. 5.10. Figure 4.3 also reveals that the modulus Y drops dramatically along the branches of localized states as they become more nonlinear, a well-known consequence of the appearance of folds [23]. For branches of mixed mode states, the modulus Y can be negative as is the case for the buckling mode B but is positive for most others, i.e. the mixed modes inherit some of the physical response features of the primary states they connect.

The energy E may also be considered as a system response measure of the different wrinkled, buckled, folded, and mixed mode states as a function of the compression Δ. This is a particularly useful measure because it provides one interpretation of the stability of these steady state solutions. We expect the lowest energy state to be physically stable, so reorderings of the energy of states is expected to correspond to transitions in stability. The lowest energy solution corresponds to $m^* = 5$, the natural wavenumber of the system for $\ell^5 = 576$, as shown in Fig. 4.5 when the compression is small. However, as Δ increases, the localized states $F_{s\pm}$ bifurcate from the $m^* = 5$ state, and the lowest energy state becomes F_{s+}, with F_{s-} at a slightly higher energy. The wrinkle-to-fold transition is therefore defined by this secondary bifurcation, with threshold at $\Delta_c \approx 0.084$ for the particular case $\ell^5 = 576$. The direction of branching of F_{s+} and F_{s-} is consistent with that leading to spatially localized states in the bistable Swift-Hohenberg equation [109, 99]. As the compression continues to increase, the first set of localized states $F_{s\pm}$ cease to be physically realisable due to self-contact at which point another localized state becomes the global minimum of energy (Fig. 4.5).

Another useful measure of the system response is the maximum curvature κ_{max}. In

Fig. 4.6 the maximum curvature of wrinkled, buckled, folded and mixed mode states is plotted as a function of the pressure difference. This provides a useful measure of the overall shape due to the constraint imposed by the Gauss-Bonnet theorem which requires that $\int_0^{2\pi} \kappa ds = 2\pi$ for a non-self-intersecting planar curve, i.e. a high curvature at one position on the elastica has global implications for the curvature across the entire domain and hence the resulting overall shape. Further, the curvature of a state is physically of interest for the wrinkling process described in arteries as regions of high curvature are expected to be more effective at dislodging plaque buildups. Therefore, the metric κ_{max} could be relevant to biological applications of this work in understanding arterial fitness. Initially all wrinkle branches rapidly increase their curvature after their bifurcation from the constant curvature $\kappa = 1$ circle solution. Larger m values result in an even faster increase in $\kappa_{\max}$. Folds and some mixed states display an even faster increase in curvature after they emerge from secondary bifurcations, with κ_{max} of F_{s+} nearly quadrupling across a range of $\Delta P \approx 20$, an increase across a far smaller pressure window than that of any primary states. The transition between the wrinkle state W_5 and the fold states $F_{s\pm}$, the first one to take place, occurs at $P = -217.7$ (Fig. 4.2) and corresponds to $\kappa_{\max} \approx 3.09$.
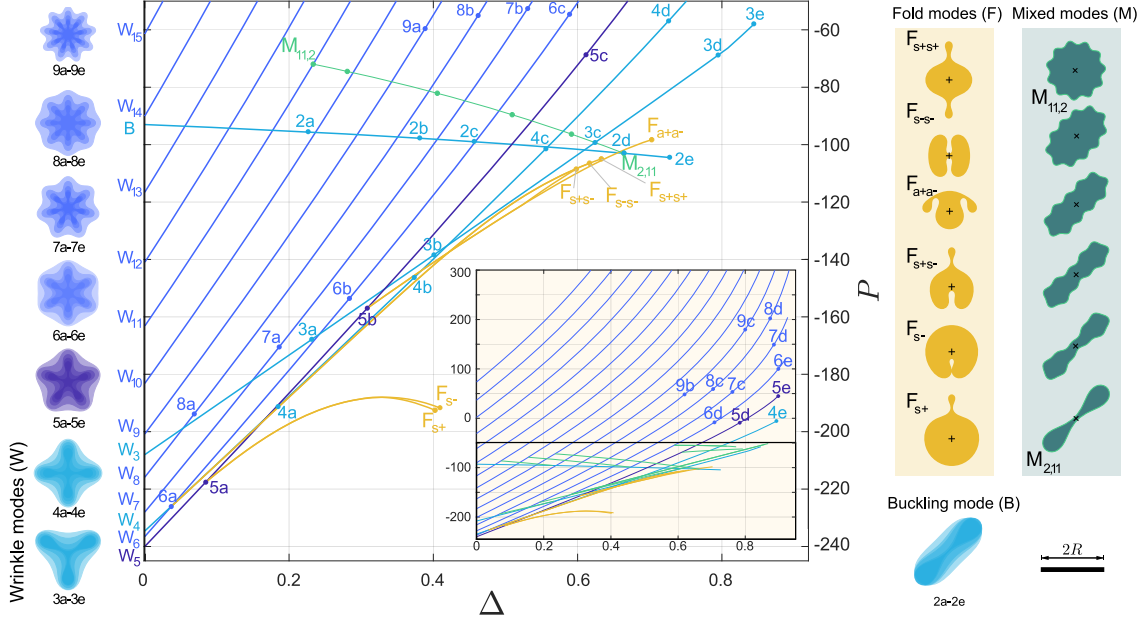
Figure 4.3: Bifurcation diagram for $\ell^5 = 576$ (corresponding to $m^* = 5$) showing the compression Δ as a function of the pressure difference P. The unperturbed circle state corresponds to $\Delta = 0$; the primary branch W_5 corresponding to states with wavenumber $m = 5$ is shown as a thin purple line. Subsequent primary wrinkle solutions W_m are labeled by their wavenumber ($m < 5$, cyan; $m > 5$, blue), while the secondary solutions are labeled F or M according to their type (fold or mixed mode). Branches are presented up to the point of self-contact. Sample solutions at the locations indicated in the main plot are shown alongside with the different wrinkle profiles for each m superposed. All solutions are reflected across the x axis for ease of visualization (solutions F and M have been rotated by 90° and 45° for convenience; the $+/\times$ symbols at the center of each profile indicate the orientation of the axes). The mixed mode branches extend between M_{m_1,m_2} where the first subscript indicates the primary wavenumber and the second the new wavenumber introduced at the secondary bifurcation. The subscripts $\pm$ on F refer to the folded states with an extrusion $(+)$ or intrusion $(-)$. The subscripts s and a indicate whether these protrusions occur on the axis or off it. The letter B labels the buckling mode $m = 2$. A scale bar of unit length is included on the right. The inset shows the same results but over a larger range of P.
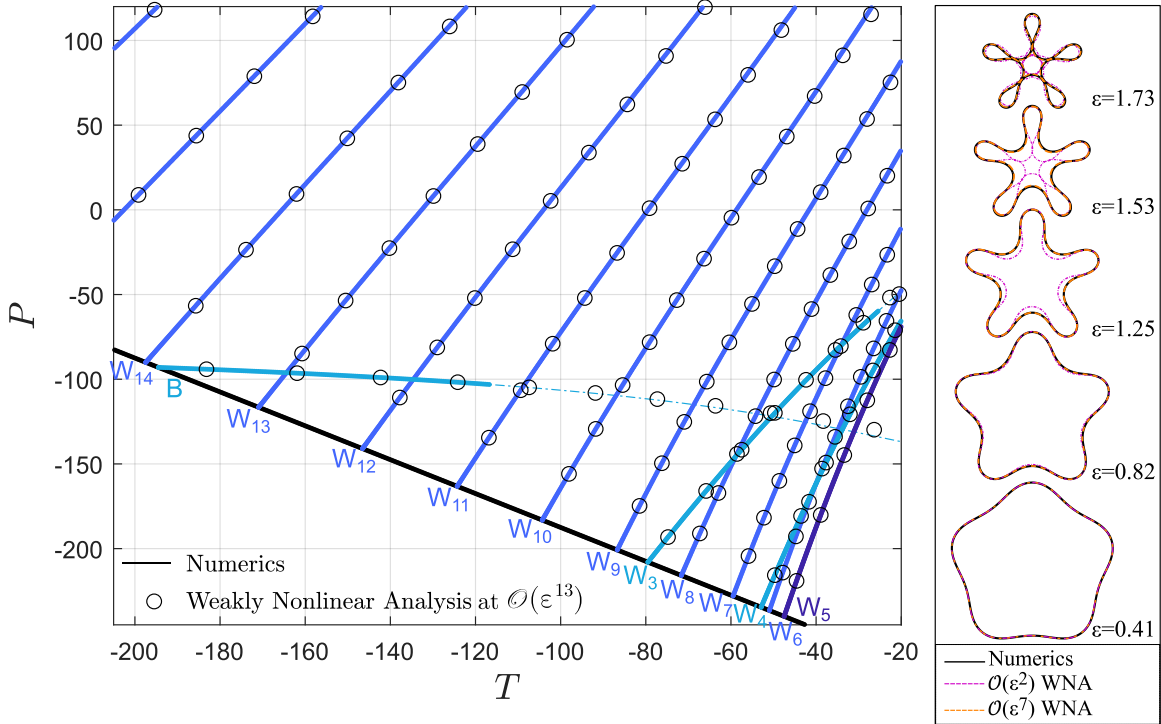
Figure 4.4: Left: comparison between numerical continuation for $\ell^5 = 576$ (solid lines) and the corresponding $\mathcal{O}(\epsilon^{13})$ weakly nonlinear analysis (open circles) demonstrating excellent agreement between perturbation theory and numerically exact solutions extending to $\epsilon = \mathcal{O}(1)$ at the top of the figure. Right: comparison between numerical solutions on the W_5 branch and weakly nonlinear solutions at $\mathcal{O}(\epsilon^2)$ and $\mathcal{O}(\epsilon^7)$ when $\ell^5 = 576$.
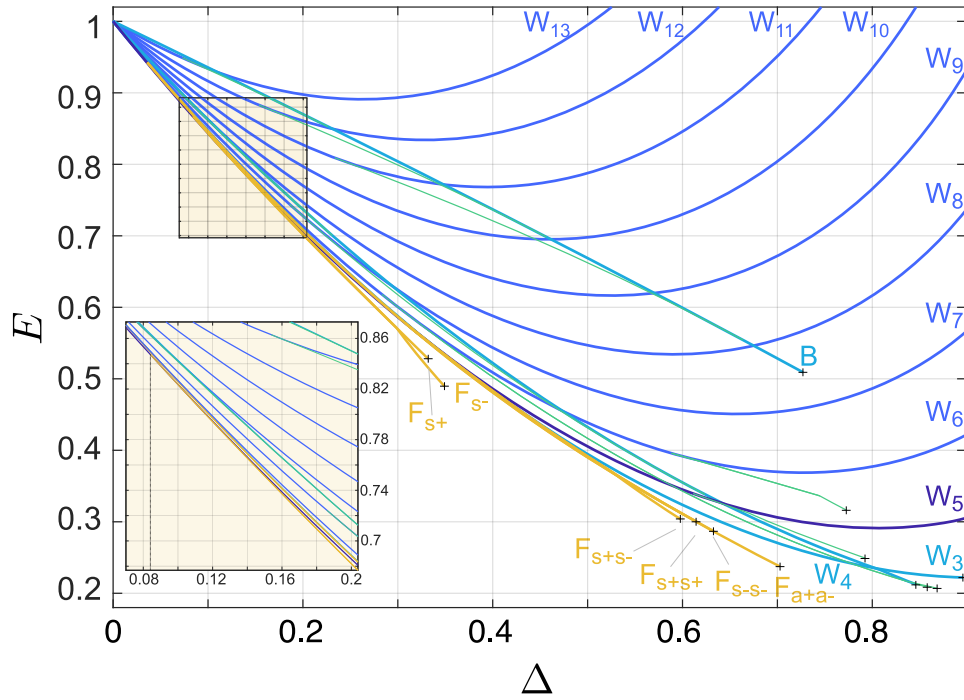
Figure 4.5: The energy E of the solutions in Figs. 4.2 and 4.3 across the compression Δ. Points of self-contact are marked with crosses. All branches start from the circle solution at $\Delta = 0$. The inset shows a zoom in which the fold state F_{s+} becomes the global energy minimum.
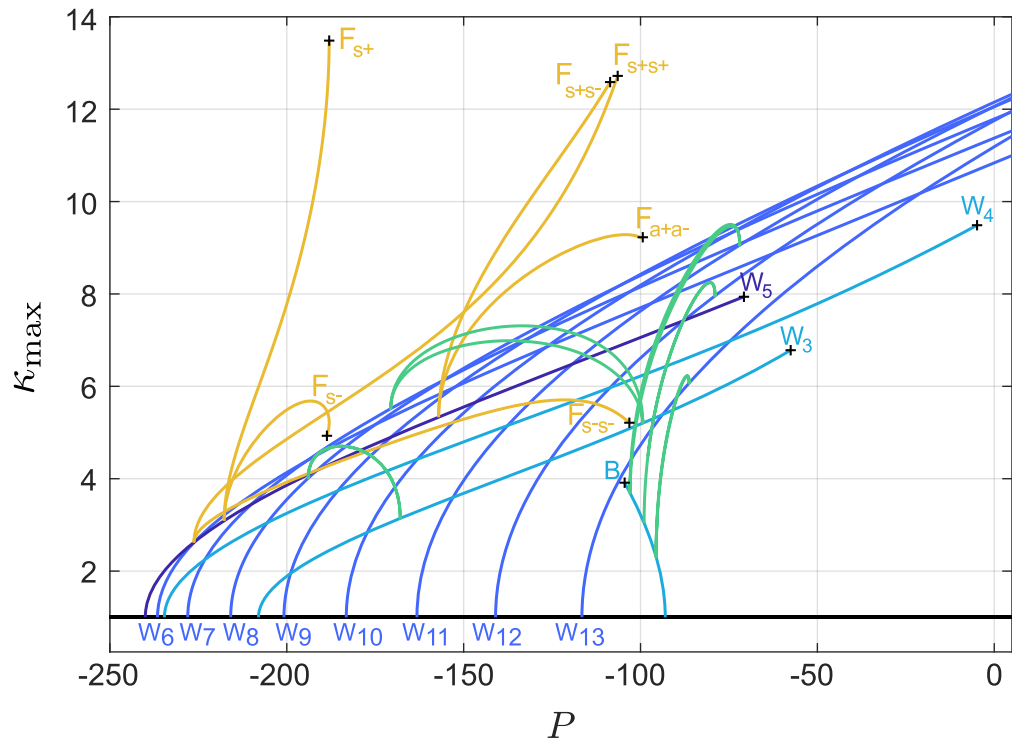
Figure 4.6: Maximum curvature $\kappa_{\max}$ as a function of the pressure difference P across the full range of compression for $\ell^5 = 576$. Self-contact of the solutions is marked with crosses. The black horizontal line shows the $R = 1$ circle solution with $\kappa_{max} \equiv 1$.

4.4 Numerical continuation: $\ell^5 = 0.005$

In this section, ℓ^5 is taken to be very small in order to compare the the results for a freely buckling ring ($\ell^5 = 0$) and a substrate supported ring as described in the previous section with $\ell^5 = 576$. When $\ell^5 \to 0$, the problem limits to the well-known pure buckling problem which does not possess an intrinsic length scale [70, 71]. In this case, the bifurcation diagrams simplify substantially, and the first buckling mode corresponds to $m = 2$ with more complex buckling modes requiring larger and larger pressures as the wavenumber m increases. When $\ell^5 = 0$, the primary third order equation for ϕ in the governing equation (5.2) decouples from the first order equations defining the spatial coordinates (x, y) such that the system may be written solely as a second order ODE in the curvature κ. This simpler problem possesses closed form solutions [110, 72, 111].

Due to this decoupling at $\ell^5 = 0$, we consider $\ell^5 = 0.005$. This nonzero but small choice for ℓ^5 provides the necessary limiting behavior, but it is sufficiently large to keep the equations coupled such that the numerical continuation scheme does not break down. In Fig. 4.7, the results of numerical continuation are summarized for comparison with Figs. 4.3–4.6.

When $\ell^5 = 0.005$, the wavenumber of the solutions emerging from the circle branch increases monotonically with the pressure difference P, beginning with the buckling mode $m = 2$. As the substrate influence decreases to zero, the pressure difference becomes the primary determinant of wrinkling, and positive pressure differences P are required for wrinkling onset for $m \geq 2$. Notably, all branches, including $m = 2$, have positive modulus Y as shown in Fig. 4.7a in contrast to $\ell^5 = 576$ when the buckling mode B had a negative modulus along the entire branch of solutions. All states are still labeled W in Fig. 4.7, but this is only because ℓ is not identically zero, at which point they should all be labelled as buckling states. No mixed modes or folds occur prior to self-contact for $\ell^5 = 0.005$ or more generally for $\ell^5 \ll 1$. Mixed modes do not occur because there is no mixing of the onset order of primary states, so there are no branches with $m < m^*$ and $m > m^*$ adjacent in parameter space. Similarly, as $\ell^5 \to 0$, secondary bifurcations to fold states move progressively farther out along each primary branch and beyond the point of self-contact, such that they do not appear in Fig. 4.7. Conversely, when ℓ^5 increases, they move down each primary branch and towards the circle solution. Therefore, secondary bifurcations to folds and mixed modes occur prior to self-contact of the primary states and for negative values of P for sufficiently large ℓ, as in Fig. 4.2.

The compression Δ is shown as a function of P in Fig. 4.7a. The modulus $Y = \partial P / \partial \Delta$ is positive for all wavenumbers m including $m = 2$ but, compared to Fig. 4.3, is much smaller along each branch. Comparing these results, the stiffening of the substrate has the effect of inhibiting the increase in compression Δ with increasing P.

Figure 4.7b shows the tension T, also as a function of P. As noted above, all

47
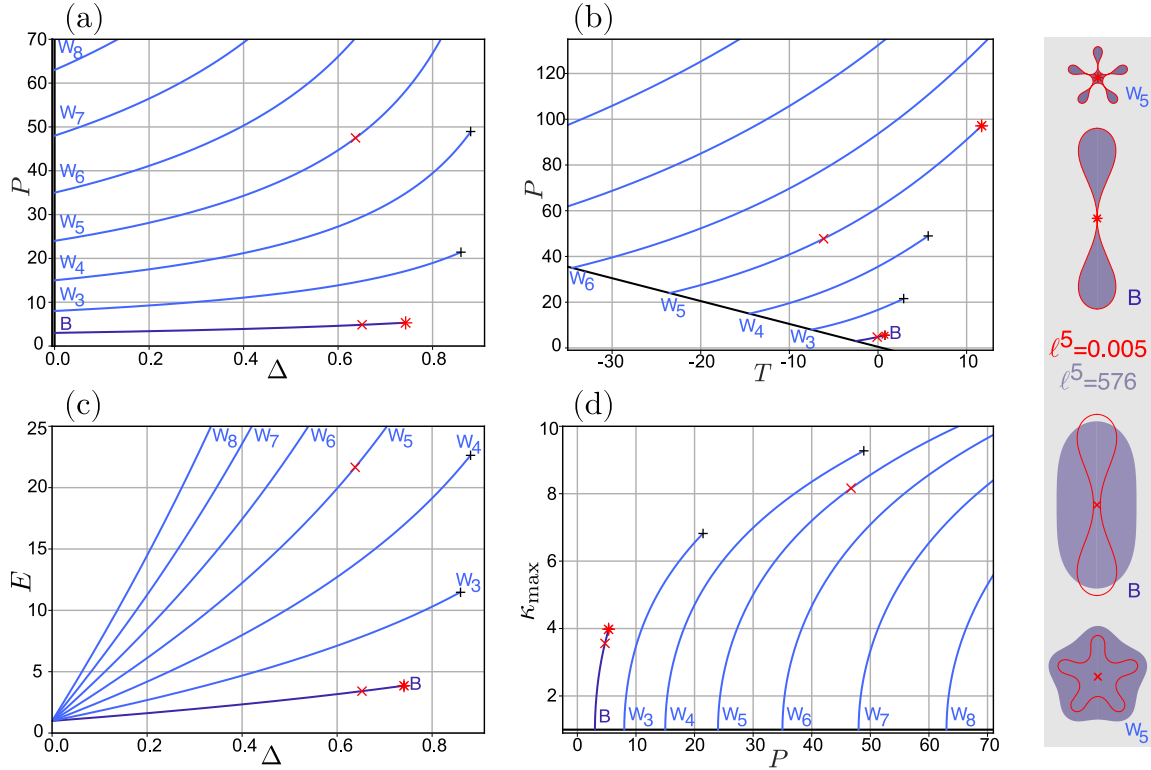
Figure 4.7: Bifurcation diagrams for $\ell^5 = 0.005$ for comparison with the case $\ell^5 = 576$ (Figs. 4.3–4.6) showing the circle (black) and all bifurcations from it, following the same color scheme and labels as in Fig. 4.2. The $m = 2$ buckling mode is now the first primary branch (B, purple line). Solution branches are shown up to the point of self-contact (crosses). (a) The compression Δ as a function of the pressure difference P. (b) The tension T resulting from an imposed pressure difference P. All primary branches have positive slope $\partial P / \partial T$ in accord with the weakly nonlinear theory. (c) The energy E as a function of the compression Δ. The $m = 2$ buckled state (B, purple line) is the global minimum energy state. (d) The maximum curvature κ_{max} as a function of P. The circle solution corresponds to $\kappa_{\mathrm{max}} = 1$ (black horizontal line). The side panel (lower) depicts the $m = 2$ and $m = 5$ solution profiles when P is increased from P_0 by 10% ($\Delta P = 24$, $\ell^5 = 576$) and 2% ($|\Delta P| = 1.86$, $\ell^5 = 0.005$). This point is indicated by a red $\times$ in the figure: the tube is substantially more compressed when ℓ^5 is smaller. The side panel also shows (upper) the $m = 2$ and $m = 5$ solutions overlaid at the point of self-contact for both ℓ values (red $*$, the only point at which different ℓ values can be precisely compared). The figure shows that for both $m = 2$ and $m = 5$ the profiles at this point are identical, i.e., the profiles at the point of contact are independent of ℓ.

branches have positive slope. Additionally, the pressure range required to reach self-contact shrinks with ℓ^5. For $\ell^5 = 0.005$, the change in P required to parametrize the entire $m = 3$ branch is about $\Delta P \approx 10$, contrasting with $\Delta P \approx 140$ for $\ell^5 = 576$. Despite these differences, the primary branches bifurcate subcritically, in the sense that the tension T becomes less negative as P increases.

The results in Figs.4.7a,b agree with the weakly nonlinear theory developed in section 4.1: all primary branches have positive slopes $\partial P/\partial T$ (Fig. 4.7b), even for $m = 2$, consistent with the asymptotic results for ϕ and (T, P). Additionally, the angle of branching in the (T, P) plane given by Eq.4.26 is positive for all branches, consistent with the requirement that a negative slope can only occur for $m = 2$ and $\ell^5 \geq 81$. Similarly, the modulus $Y = \partial P/\partial\Delta$ is positive for all wavenumbers m (Fig. 4.7a).

The energy E is shown as a function of the compression Δ in Fig. 4.7c for $\ell^5 = 0.005$ (cf. with Fig. 4.5). In contrast to the case for $\ell^5 = 576$, the energy for $\ell^5 = 0.005$ increases monotonically with the compression and the wavenumber m. Physically, this can be understood by consideration of the two contributions to the energy. When ℓ^5 is small, the the substrate extension energy is dominated by the elastica bending energy, and the bending energy contribution grows as the solution compresses further. Therefore, for a given compression, the state with the lowest overall curvature is the lowest energy state, i.e., the wavenumber $m = 2$ state is the minimum energy state and therefore is globally stable until self-contact. After this point, stability is transferred to the next lowest wavenumber solution, $m = 3$, etc. As ℓ^5 increases, the substrate energy becomes more significant, and overall curvature becomes an insufficient measure of stability.

The maximum curvature κ_{max} is plotted as a function of the pressure difference P in Fig. 4.7d (cf. Fig. 4.6). For small ℓ^5, maximum curvature (and therefore self-contact) occurs much earlier with increasing P than for larger ℓ^5. In each case, the maximum curvature necessarily coincides with the point of self-contact and is identical to the corresponding curvature when $\ell^5 = 576$, indicating that the curvature of a given wavenumber state is invariant to changes in ℓ^5.

Concluding the discussion of Fig. 4.7, the side panel compares the profiles of the $m = 2$ and $m = 5$ solutions for $\ell^5 = 0.005$ and $\ell^5 = 576$. The comparison is made at a point 10% from the critical pressure P_0 for $m = 5$ and 2% from the critical pressure for $m = 2$ and again at the point of self-contact for both (red $\times$s and $*$ symbols, respectively). As mentioned earlier in the discussion of Fig. 4.7a,b, when ℓ^5 is large, the amount of compression for given ΔP is substantially less than for smaller ℓ^5. Thus the wrinkling or buckling process occurs over a smaller interval of P as ℓ^5 decreases. However, at the point of self-contact the profiles in the two cases are identical and independent of the parameter ℓ as suggested by the weakly nonlinear analysis.

As ℓ^5 increases, the wavenumber of the first mode to set in, m^*, increases as predicted by linear theory (cf. Fig. 4.1). These discrete shifts from one integer critical wavenumber to the next causes repeated *mode jumping*. For example, when
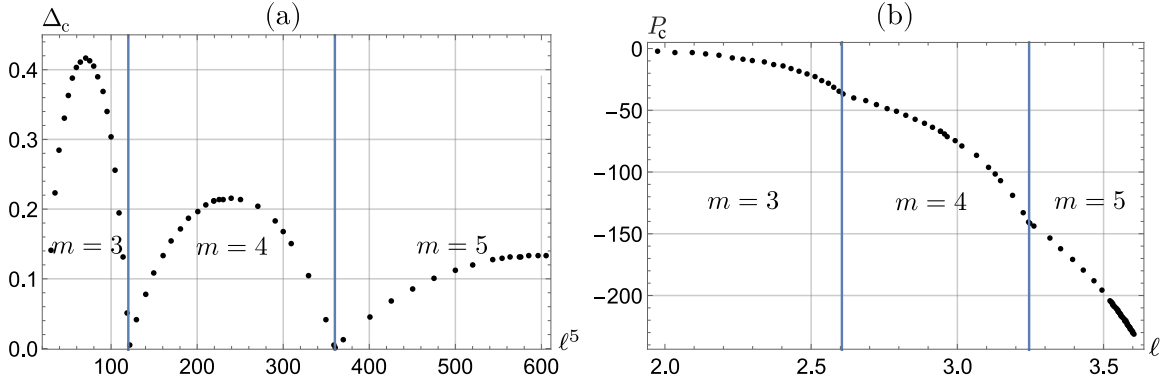
Figure 4.8: (a) The compression Δ_c at the secondary bifurcation from the primary wrinkled state to the first fold state as a function of ℓ^5, showing the behaviour of this bifurcation point with changing wavenumber of the wrinkled state. The vertical lines show the codimension two points $\ell^5_{m,m+1} \equiv (m-1)m(m+1)(m+2)$ when $m = 3$ and 4. (b) The corresponding plot of P_c as a function of ℓ.

$\ell^5 = 320$ the critical wavenumber is $m^* = 4$, while for $\ell^5 = 576$ it is $m^* = 5$. Thus, as ℓ^5 increases, $m^* = 4$ remains the critical wavenumber mode over a finite interval in ℓ^5 until it is replaced by $m^* = 5$ as the new critical mode. This transition is associated with a codimension two point requiring tuning of P and ℓ^5 such that the dispersion relation (4.12) is simultaneously solved by two adjacent values of m, here $m^* = 4$ and $m^* = 5$. A similar mode jumping phenomenon occurs in wrinkling of planar elastica (cf. [23, Figure 5]). Mode jumping has implications for secondary states as well, as secondary fold states bifurcate from wavenumbers close to m^*. For example, when $m^* = 4$ the single fold states $F_{s\pm}$ bifurcate from W_4; as ℓ^5 increases towards the codimension two point $\ell^5_{4,5} = 360$ the secondary bifurcations leading to the folds move down along the W_4 branch and reach zero amplitude when $\ell^5 = \ell^5_{4,5}$. For $\ell^5 > \ell^5_{4,5}$ the dominant mode is $m^* = 5$ and the secondary bifurcation to the fold state now takes place on W_5. As ℓ^5 increases, this bifurcation moves up along W_5 to a maximum amplitude before moving down again as the next codimension two point is approached. This process repeats as ℓ^5 continues to increase, and Δ_c and P_c, the compression and pressure difference threshold for the onset of the fold state from the primary state, therefore both oscillate and jump from branch to branch. This behaviour is shown for Δ_c in Fig. 4.8(a) and P_c in 4.8(b) and is similar to results in the planar case [23, Figure 5]. As ℓ^5 increases (i.e. as the tube radius R becomes large relative to the natural length scale), the tubular problem is expected to approach a near-planar geometry, and the results are therefore expected to become comparable to those of the planar system.

50

Chapter 5

Fluid substrate

In the previous section, we analyzed Eq. (3.6), resulting from the choice of a solid substrate, and provided an organization of the equilibrium solutions via bifurcation diagrams and an exploration of the effect of the parameter ℓ^5 on these results. In this section, we will consider Eq. (3.7), the governing equation for the steady state deformation of an elastic interface between two fluids in a rotating Hele-Shaw cell. This leads to two significant perspective changes from the prior section: the membrane may be taken to be perfectly extensible such that its length is unconstrained as discussed in section 3.3, and the forcing is now determined by the rotation rate, a much more straightforward parameter to quasistatically tune in experiments than the stiffness.

The time-dependent growth of the wrinkle instability was explored for this system in a series of papers by Carvalho et al [64, 59] with a subsequent study of strongly nonlinear, time-independent states [65] based on the assumption that the pressures in the interior and exterior fluids are identical and that the interface cannot support tension. The second assumption is consequential: it implies there is no force that resists changes in the interface length. As a result, Carvalho et al report a series of steady state profiles with different interface lengths without organizing these states into a bifurcation scenario that describes how the steady states of the system vary with system parameters.

We will again construct bifurcation diagrams in terms of the pressure difference and the resulting tension (P, T) in the case that the interface is inextensible or in terms of the pressure difference and resulting interface (P, L) in the case when it is not. If P is held fixed and the rotation rate Ω is varied, one may instead show the (Ω, T) plane.

5.1 Constrained length

We expect a centrifugal instability to set in when $\Delta\rho > 0$, i.e., when the density of the inner fluid exceeds that of the outer one, and use this fact to introduce the natural

length scale of the instability

$$\lambda \equiv \left(\frac{\mathcal{B}}{\Delta\rho\,\Omega^2} \right)^{\frac{1}{5}}.$$ (5.1)

We use this scale to construct a dimensionless parameter $\ell \equiv R/\lambda$ that measures the radius R of the elastica in units of the natural length λ.

Rescaling Eq. (3.7) according to $s \sim R$, $\kappa \sim R^{-1}$, $r \sim R$, $T \sim \mathcal{B}/R^2$, $P \sim \mathcal{B}/R^3$, we obtain

$$\partial_s^3 \phi + \frac{1}{2}\left(\partial_s \phi \right)^3 - T\partial_s\phi - P - \frac{1}{2}\ell^5 r^2 = 0.$$ (5.2)

Instability of the circular membrane arises when the denser interior fluid is displaced outwards, thereby increasing the outward force upon it. When this force exceeds the restraint arising from the curvature of the interface, the tension T, and the imposed pressure difference P, instability sets in and it is this balance which gives rise to wavelength selection.

In the unperturbed problem, the interface is circular and of length $L = 2\pi$, with $T = \frac{1}{2}(1-\ell^5)-P$. A linear stability analysis of this state yields the dispersion relation for the mode number m of the fingering instability [66]

$$m^4 - \left(2 + P + \frac{\ell^5}{2} \right) m^2 + \left(1 + P + \frac{3}{2}\ell^5 \right) = 0.$$ (5.3)

From this relation, we can determine the wavenumber m^* of the first unstable mode that sets in as P increases and the critical value $P = P^*$ at which it does so:

$$m^* = (1 + \ell^{5/2})^{1/2}, \qquad P^* \equiv (-\ell^5 + 4\ell^{5/2})/2,$$ (5.4)

all for a fixed rotation rate Ω. Alternatively, we may fix P and increase the rotation rate leading to the critical rotation rate $\Omega(m, P)$,

$$\Omega \equiv \left[\frac{B}{\Delta\rho R^5} \left(\frac{2(m^2 - 1)(P - m^2 + 1)}{3 - m^2} \right) \right]^{1/2},$$ (5.5)

for the appearance of a mode with wavenumber m; minimizing this expression over m for fixed P recovers the results in Eq. (5.4). Figure 4.1 shows several examples of the marginally stable wavenumber m as P and ℓ^5 vary and shows that, as ℓ^5 increases, instability sets in at lower and lower values of P and with larger and larger values of m^*, i.e., larger finger wavenumbers. This is the fingering instability whose nonlinear development is key to understanding the constrained system. When m^* is not an integer, the figure shows that the primary instability corresponds to the integer m nearest to the m^* given by Eq. (5.4).

5.2 Unconstrained length

When the interface cannot support any tension, the instability may lead to interface growth. In this case $T = 0$ and the length L of the interface becomes a free parameter. We are interested in this case because earlier work by Carvalho et al. [65] presented a number of solutions to Eq. (5.2) with $T = 0$ with interfaces of different (and unspecified) lengths. With L as a free parameter, nondimensionalization requires rescaling Eq. (3.7) using the natural length scale λ. We take $s \sim \lambda, \kappa \sim \lambda^{-1}, r \sim \lambda, P \sim \mathcal{B}/\lambda^3$ such that the rescaled governing equation is now given by

$$\partial_s^2 \kappa + \frac{1}{2}\kappa^3 - P - \frac{1}{2}r^2 = 0. \tag{5.6}$$

For a circular interface this equation yields a monotonic relation between the pressure difference and the interface length, $P = ((L/2\pi)^{-3} - (L/2\pi)^2)/2$, so in equilibrium there is only one L for a given P.

A linear stability analysis of this state, similar to that leading to (5.3), yields

$$m^4 - \frac{5}{2}m^2 + \left[\frac{3}{2} + \left(\frac{L}{2\pi}\right)^4\right] = 0. \tag{5.7}$$

This relation has no real roots for $L \geq \pi$, indicating that solutions of wavenumber m do not emerge as primary bifurcations from the circle state as P varies. Thus all nontrivial states are the result of a finite amplitude perturbation.

5.3 Constrained length: fingers

The order with which primary finger states bifurcate from the circle state is determined by the parameter ℓ^5 as it sets the critical wavenumber m^* via Eq. (5.4). Subsequent bifurcations as P increases lead to modes with wavenumbers m alternately above and below m^*. Once $m = 2$ is reached only modes with large wavenumbers m remain and these continue to be destabilized as P increases as seen in Fig. 5.1 (cf. Fig 4.2). The figure shows the response of the system, as indicated by the tension T, to changes in the imposed pressure difference P for three values of ℓ^5, i.e. the rotation rate, obtained using numerical continuation starting from the neutral modes of the circle state (black line). The corresponding solution profiles at the point of first self-contact are shown alongside. We see that for large enough ℓ^5 the primary finger states bifurcate to secondary branches of mixed mode states connecting a primary branch with $m < m^*$ to a primary branch with $m > m^*$ (Fig. 5.1(b), shown in green), as well as to circumferentially localized states we call folds (Fig. 5.1(a,b), shown in yellow) which do not connect to another branch. The mixed modes do not set in prior to self-contact when ℓ^5 is small but begin to proliferate with increasing ℓ^5; for

this reason they are omitted from panel (c). The primary mode with $m = 2$ is called here a buckling mode (labeled B) because of its radically different behavior at large ℓ^5, with negative modulus dP/dT, behavior typical of buckling processes [66]. In the absence of a natural wavelength λ or as λ becomes large relative to the domain, the $m = 2$ mode is the first to become unstable [70].

Single folds bifurcate from the first primary branch $(m = m^*)$ and do so prior to self-contact whenever $m^* \geq 3$. Figure 5.1(a) shows the case $m^* = 3$ $(\ell^5 = 64)$ and shows that these states emerge in pairs, here a single protrusion fold F_{s+} and a single intrusion fold F_{s-} (for profiles see Figs. 5.6 and 5.7). The resulting branches track closely but do not self-contact at the same point; mixed mode branches are absent. In panel (b), for $\ell^5 = 576$, fingering, buckling and mixed modes are all present, as well as additional folds. In (c), for $\ell^5 = 14400$, the number of mixed modes and folds becomes large, and these states are omitted.

As in the previous section, the finger profiles are ℓ^5-independent [110, 73, 74, 83], so the displayed self-contact solutions hold for any of the bifurcation diagrams, although their location in the (T, P) plane does vary with ℓ^5 [83].
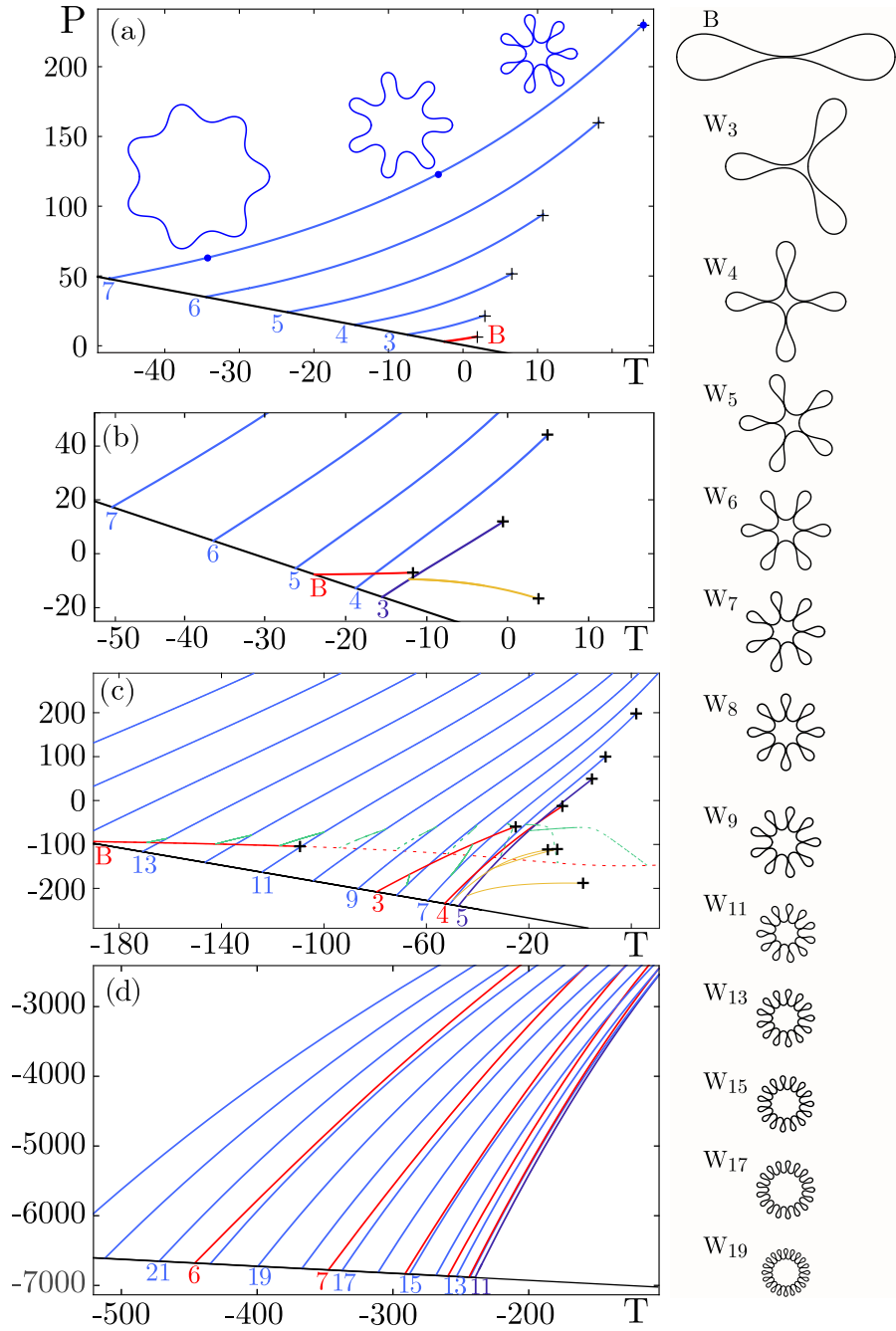
Figure 5.1: Bifurcation diagrams in the (T, P) plane for (a) $\ell^5 = 0$ ($m^* = 2$), (b) $\ell^5 = 64$ ($m^* = 3$), (c) $\ell^5 = 576$ ($m^* = 5$) with some states beyond self-contact shown with dashed lines, and (d) $\ell^5 = 14400$ ($m^* = 11$), showing the succession of color-coded primary branches of finger states as P increases: primary fingers with $m = m^*$ (purple), $m > m^*$ (blue), and $m < m^*$ (red). Mixed mode (green) and fold (yellow) branches are suppressed in (d). Primary bifurcation points are labeled by the corresponding wavenumber m, while points of self-contact are indicated with crosses. Selected solution profiles at the point of self-contact are shown on the right.

55

5.4   Constrained length: $P = 0$ fingers

Finger solutions when the applied pressure difference $P = 0$ are of physical interest as they dictate solutions which may be observed in ambient conditions, emerging solely from the competition between inertial and elastic energies. Of course, these solutions have the same shape as before, but the length and tension at which they arise are not known *a priori*. Figure 5.2 shows their location in the (T, L) plane. Solutions bifurcate with m increasing monotonically from $m^* = 2$ as L increases. We note that the size of the marginally stable circle state may be smaller than in Fig. 5.1 for finger solutions with m values close to m^* since these typically bifurcate from the circle state already at more negative P, i.e. for these states $L < 2\pi$. Moreover, for the value of ℓ^5 used in Fig. 5.2, $\ell^5 = 576$, the states with $m = 2, 3$ reach self-contact at $L < 2\pi$ and at negative values of T, i.e., under compression. In contrast, for larger values of m, the circle at threshold is generally larger than $L = 2\pi$ and self-contact generally occurs at small or slightly positive values of the tension T.
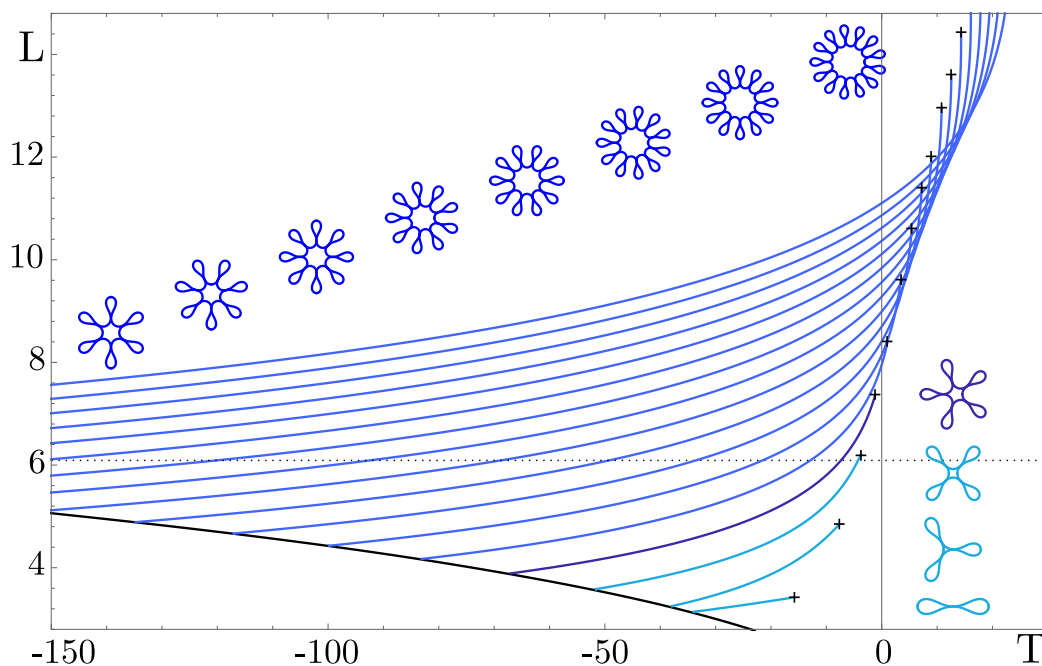
Figure 5.2: The $P = 0$ steady state solutions in the (T, L) plane for $\ell^5 = 576$ ($m^* = 5$ in purple), where L is the interface perimeter. All profiles are plotted on the same scale. The horizontal dashed line indicates $L = 2\pi$, the length used in all other constrained problem computations.
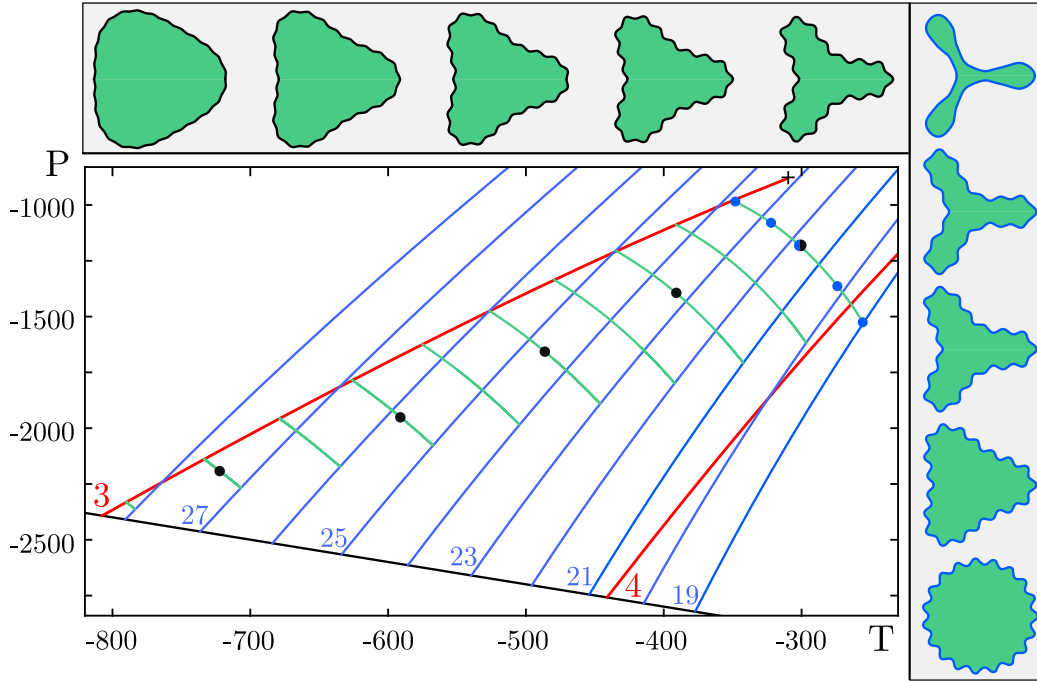
Figure 5.3: A partial bifurcation diagram for $\ell^5 = 6400$ ($m^* = 9$) with all complete mixed mode connections between the $m = 3$ finger state and other primary branches. The profiles above the bifurcation diagram correspond to the black dots proceeding from left to right, while the profiles on the right correspond to the blue dots on the mixed mode branch $M_{3,19}$, proceeding downwards.

5.5 Constrained length: mixed modes

In Fig. 5.3, we show an example of the richness of the mixed mode connections at higher values of ℓ^5, here $\ell^5 = 6400$ ($m^* = 9$), where more states with $m < m^*$ are interspersed with states with $m > m^*$. The profiles above the diagram provide examples of mixed mode states with comparable contributions from both wavenumbers (black dots). In contrast, the profiles along the side correspond to profiles along a single mixed mode branch, here the branch $M_{3,19}$ connecting the $m = 3$ and $m = 19$ primary finger branches.

In Fig. 5.4, we show another example of mixed mode connections, computed for $\ell^5 = 14400$ ($m^* = 11$). The figure shows the connections along a primary branch with $m = 23$, i.e., $m > m^*$, as opposed to Fig. 5.3 where we showed all the secondary connections for a $m = 3$ primary branch, $m < m^*$. The solutions in Figs. 5.3 and 5.4 match closely those previously identified via a different computational procedure (see Figure 4 of Ref. [65]).

The spatial profiles of mixed modes depend on the parameter ℓ^5 via its effect on the primary bifurcation ordering. A branch of mixed mode solutions connects
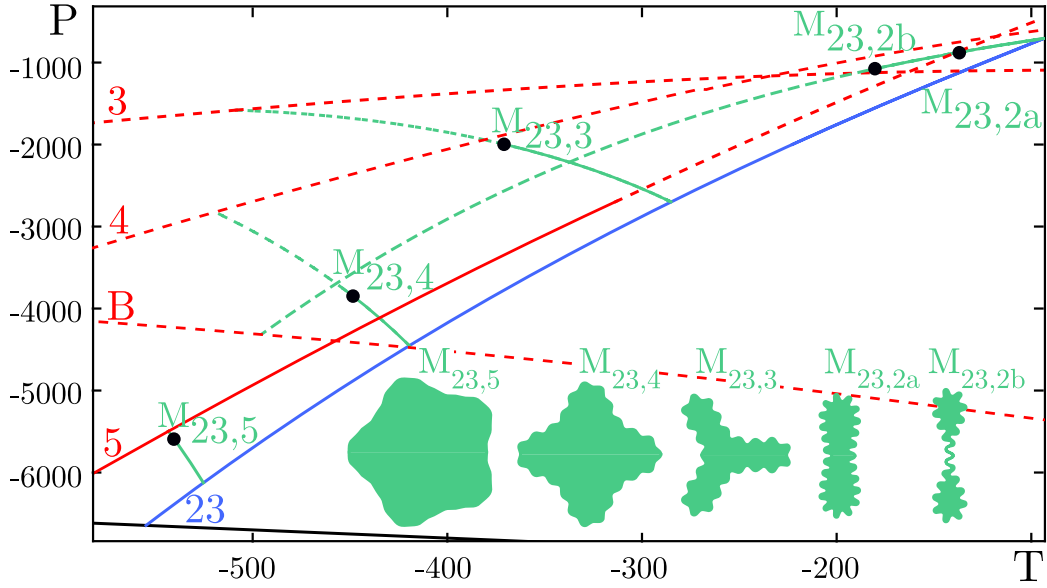
Figure 5.4: A partial bifurcation diagram for $\ell^5 = 14400$ ($m^* = 11$) with four mixed mode connections between $m = 23$ and the primary branches with $m = 2$ (B), $3, 4, 5$. Solutions beyond the point of self-contact are shown with broken lines. The lower panels show profiles at the locations indicated by black dots (two on the $M_{23,2}$ branch).

two primary branches with $m < m^*$ and $m > m^*$ when they are nearby in the (T, P) parameter space. When ℓ^5 increases, the ordering is increasingly scrambled as shown in Fig. 5.1, and the mixed mode branch locations are shifted with the primary branches. This impacts the solution profiles structurally since different mixed mode connections become available for different primary branch orderings. Even when a specific connection between primary wavenumbers persists, the mixed mode profile is still impacted by changes in ℓ^5 as the bifurcations from the primary states of wavenumber m_1 and m_2 shift and the relative amplitude contribution of the m_1 and m_2 primary states changes accordingly. This second effect is shown in Fig. 5.5.
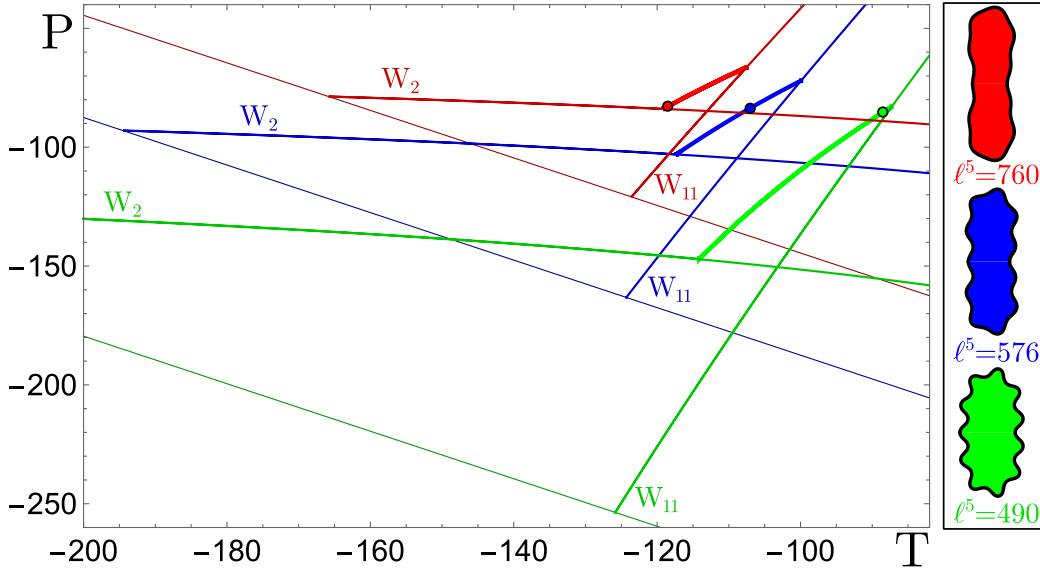
Figure 5.5: The $m = 2, 11$ mixed mode branch for $\ell^5 = 490, 576, 760$. All solutions are shown at an equal compression $\Delta = 0.1$.

5.6 Constrained length: folds

Additional secondary branches which do not connect to any other branches bifurcate from the finger branches at or near the critical branch with $m = m^*$ (Fig. 5.1(a,b), yellow curves). These correspond to localized solutions and typically come in pairs. The first pair always has a single intrusion or protrusion ($F_{s\pm}$) and bifurcates from the critical finger branch (Fig. 5.1, yellow curves). Intruding and protruding states follow essentially identical paths in the bifurcation diagram and reach self-contact at almost the same point in the (T, P) plane (Fig. 5.1(a)).

Figure 5.6 explores the ℓ^5-dependence of the simplest fold states F_{s+} at self-contact and shows that the width of the localized structure decreases in the expected way relative to the perimeter length as $\ell \equiv R/\lambda$ or equivalently the rotation rate increases.

Changes in ℓ^5 also have an effect on the localized state branches in parameter space. Figure 5.7(a) shows that for moderate values of ℓ^5 the branches of $F_{s\pm}$ fold on

Figure 5.6: F_{s+} solutions at self-contact for increasing values of ℓ^5 corresponding to $m^* = 3, 4, 5, 6, 9, 11$.
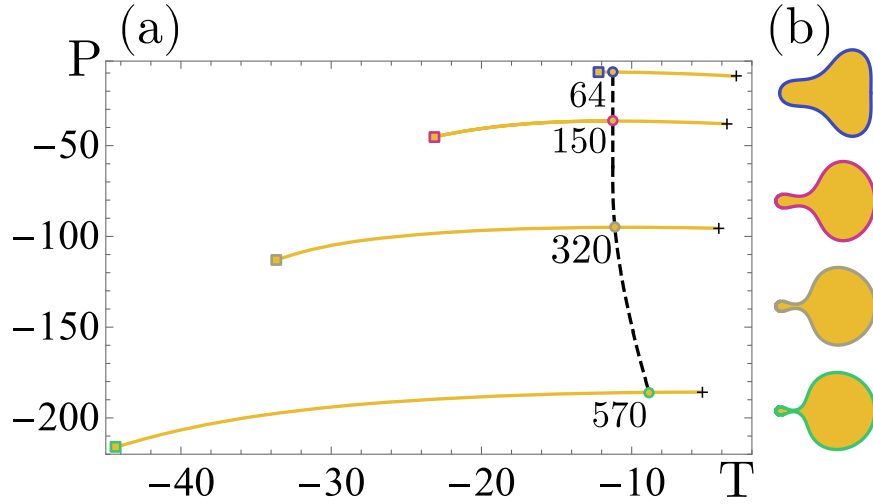
Figure 5.7: Numerical continuation (black dashed line) in the (T, P) plane of the local maxima on the branch of F_{s+} localized fold states (yellow lines) between $\ell^5 = 64$ ($m^* = 3$) and $\ell^5 = 570$ as indicated in the labels. Since T measures the response of the system to changes in the pressure difference P, these maxima represent saddle-node bifurcations. The continuation is terminated when the saddle-node reaches the point of self-contact (crosses) or the bifurcation point from the primary branch (squares). The corresponding solution profiles at the labeled saddle-nodes are shown alongside.

themselves, each exhibiting a saddle-node bifurcation. These bifurcation points can be followed numerically and Fig. 5.7(b) shows the result of such a computation for F_{s+} starting from the saddle-node bifurcation at $\ell^5 = 225$ and both increasing and decreasing ℓ^5. Evidently, as ℓ^5 varies, so does the wavenumber m^* of the branch from which the F_{s+} bifurcate. This is in fact a continuous process: as ℓ^5 increases, for example, the secondary bifurcation to F_{s+} moves down along the $m^* = 4$ branch to the primary bifurcation point. As this happens, the $m = 5$ primary bifurcation passes through the $m^* = 4$ primary bifurcation point, so that for larger ℓ^5 the circle state loses stability first to $m^* = 5$, followed by $m = 4$, i.e., the $m = 4$ and $m = 5$ branches exchange positions. Beyond this point the secondary bifurcation to F_{s+} moves up the new m^* branch, and the whole process repeats [23, 112]. However, despite the jumps in m^* the movement of the saddle-node of the fold states F_{s+} as ℓ^5 varies is continuous. With increasing ℓ^5, the saddle-node moves past the point of self-contact, and we terminate the continuation when this first happens ($\ell^5 \approx 570$).

As ℓ^5 increases, the variety of localized fold states increases dramatically since fold states now bifurcate not only from the critical finger state with $m = m^*$, but also from the subsequent primary finger branches. In Fig. 5.8, we show all localized
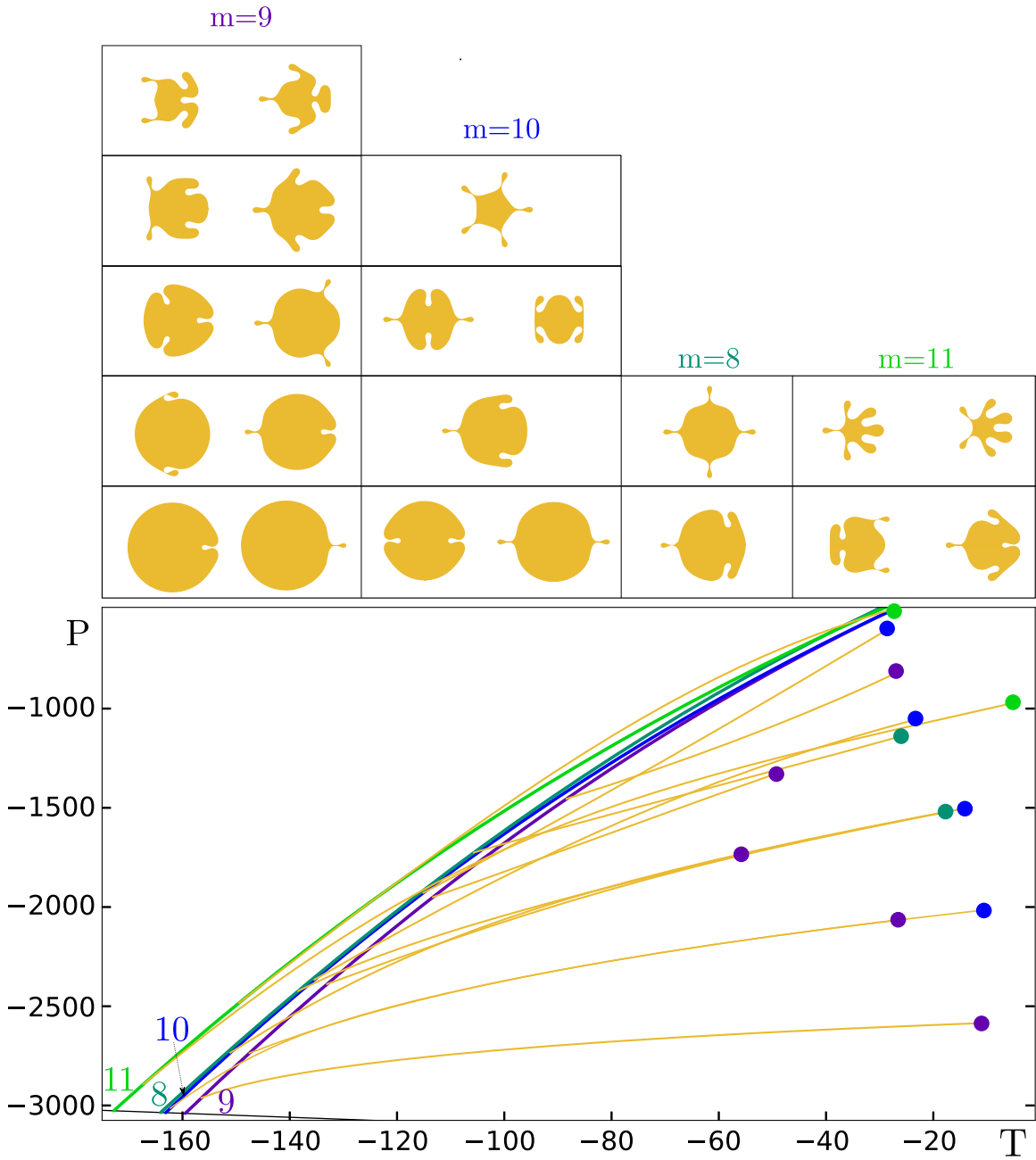
Figure 5.8: Bifurcation diagram for $\ell^5 = 6400$ depicting the first few finger modes ($m^* = 9$, and $m = 10, 8, 11$, color-coded) and the multitude of remarkable fold states that bifurcate from them (yellow). Solutions at the point of self-contact, arranged in ascending order and labeled with dots of the corresponding color, are shown at the top. Branches of intrusions and protrusions are almost degenerate leading to overlapping dots.

fold states for a given ℓ^5 ($\ell^5 = 6400$). The critical primary branch supports the most secondary bifurcations to fold solutions. Although subsequent branches have a similar overall number of secondary bifurcations, the number of bifurcations to fold states decreases while the number of bifurcations to mixed mode states increases. The details depend on the number of factors of each integer m and hence on the symmetry of the branch states. For example, Fig. 5.8 shows several localized states with a $\frac{2\pi}{3}$ rotational symmetry emerging from the $m = 9$ finger branch which shares this symmetry. Similarly, we see a $\frac{2\pi}{5}$ rotational symmetry in one of the localized states emerging from $m = 10$ and a $\frac{\pi}{2}$ rotational symmetry in one that emerges from $m = 8$.

5.7 Unconstrained length: fingers

Equation (5.6) results from consideration of the same system taking T to be zero and the interface length L to be a free parameter, with numerical continuation of steady state symmetric finger states proceeding as before. Figure 5.9 shows the continuation of several finger states in the (L, P) plane. The area and perimeter of the steady state finger profile grow dramatically as the interior pressure drops. With a smaller contribution from internal pressure, a larger contribution from the centrifugal force is needed to support a steady state, requiring larger L. However, finger states no longer bifurcate from the circle state, in stark contrast to the constrained length results with nonzero tension. Further, although secondary bifurcations do set in as L increases, for these small values of m they set in beyond the point of self-contact. This is no longer the case for larger values of m as shown in Fig. 5.10.
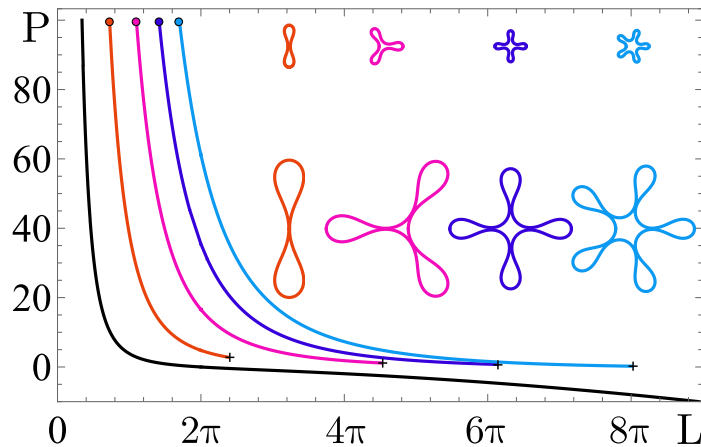
Figure 5.9: Numerical continuation of $m = 2, 3, 4, 5$ finger states (orange, pink, dark and light blue, respectively) in the (L, P) plane. The branch of circle states is shown in black, and self-contact is indicated by crosses. The finger states no longer bifurcate from the circle state.
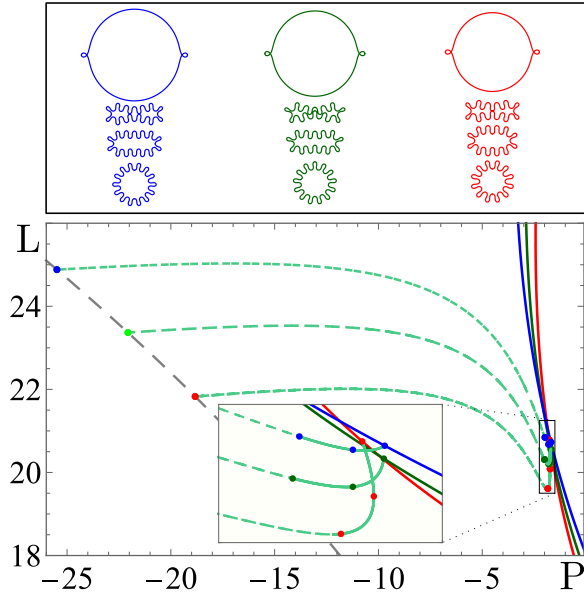
Figure 5.10: Bottom: mixed mode connections (light green) between $m = 2$ (grey) and $m = 12$ (red), $m = 13$ (dark green), and $m = 14$ (blue) finger states shown in the (P, L) plane. Dashed lines indicate solutions beyond first self-contact. Top: sample solutions at the color-coded locations indicated in the bottom panel proceeding from the $m = 2$ start of the mixed mode branch to its endpoint at the other end. In each case the top profile corresponds to an unphysical, self-intersecting solution on the $m = 2$ branch while the profile below corresponds to last self-contact (lower panel zoom). Beyond this point the solutions are realizable; the final profile corresponds to a pure finger state at the right end of the branch.

5.8 Unconstrained length: mixed modes

mixed mode states connecting two primary branches with different numbers of fingers also exist. Figure 5.10 shows three mixed mode branches (light green lines) originating on the $m = 2$ finger branch (grey line), shown in the (P, L) plane. The branches terminate on the $m = 12$ (red), $m = 13$ (dark green) and $m = 14$ (blue) finger states, respectively. The solutions are realizable near the high m end of the branch (solid light green lines) but as P becomes more and more negative they make self-contact, beyond which point the solutions are no longer physically realizable. The top panel in the figure shows the pure finger state at the right end of each branch (lowest profile), a physical solution before self-contact (second profile from the bottom), the solution at first self-contact (third profile from bottom) and finally an unphysical, self-intersecting profile very close to the termination of the mixed mode branch on the $m = 2$ branch (top profile).

5.9   Unconstrained length: folds

Fold states arise through bifurcations from the primary finger states, although this time almost exclusively from states far beyond self-contact. Figure 5.11 shows a number of examples in the (P, L) plane. The number of distinct states created in each bifurcation grows in successive bifurcations as P decreases (L increases) and depends on the wavenumber m of the underlying finger state. At large negative P (large L) branches with the same number of intrusions and protrusions are almost degenerate since both contribute only slightly to the length, despite originating in general from different primary finger states as indicated by the color-coded profiles at the top panels. For example, there are four branches labeled 2, two of which originate from the $m = 2$ finger branch (red) and two of which originate from the $m = 3$ finger branch (orange). The branches originating in the same branch are strictly degenerate in this projection, although they reach self-contact at slighly different locations (not shown).

Every primary finger branch (thick lines) yields a multitude of secondary branches of fold states with varying numbers of intrusions and protrusions. The first fold state to emerge from a primary finger state with wavenumber m generates a state with $m - 1$ folds, and each subsequent secondary bifurcation adds one additional fold. These folds can be intruding, protruding, or come in antisymmetric pairs (due to the symmetry constraint imposed by our boundary conditions). There is always a special pair of intruding and protruding fold states which respect the symmetry of the finger state they bifurcate from.

As P becomes more negative and the length of the domain increases, the profiles gradually deform from the self-intersecting, nonphysical states they bifurcate from into non-self-intersecting, physically realizable states. Beyond the point of last self-contact, the profiles remain physical even as their length continues to increase. Simultaneously, the details of the shape of the folds become less important, and the branches collapse to evenly spaced curves, each corresponding to a particular number of folds, as indicated on the left of the bifurcation diagram. Each of these asymptotic lines consists of multiple branches originating from different primary states. For example, there are four distinct 2-fold states, two of which are symmetric states with either two intrusions or two protrusions originating from the second primary bifurcation on the $m = 2$ finger branch, and two additional states, one with one intrusion and one protrusion, and one with a pair of antisymmetric folds, originating from the first primary bifurcation on the $m = 3$ finger branch. In the present projection, these pairs of branches lie on top of one another and one therefore sees only two branches, labeled 2. Likewise there are three branches labeled 3, originating in the third bifurcation on the $m = 2$ branch, the second bifurcation on the $m = 3$ branch and the first bifurcation on the $m = 4$ branch, each with appropriate multiplicity (see
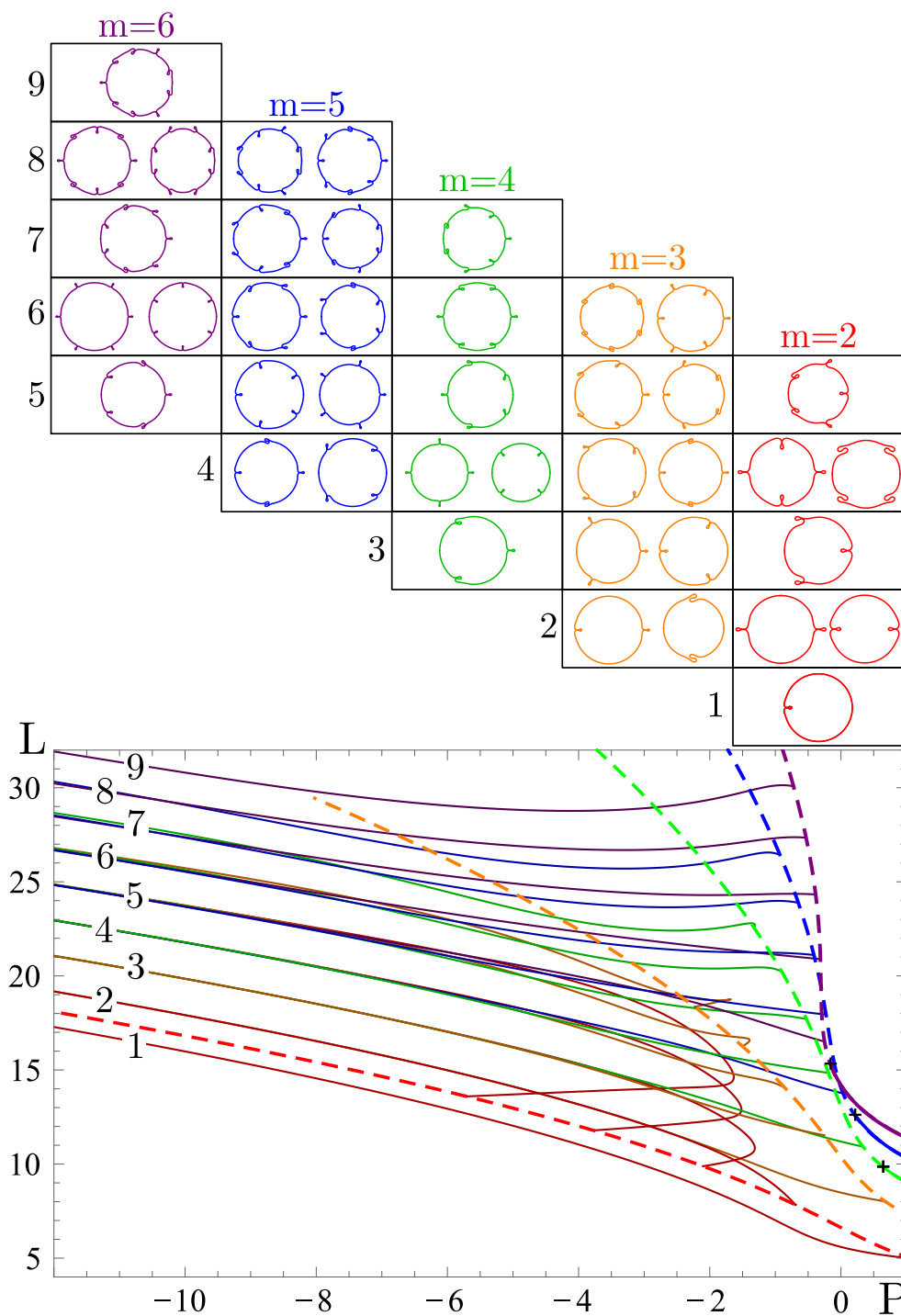
Figure 5.11: Bifurcation diagram depicting the $m = 2, 3, 4, 5, 6$ finger states in thick lines (red, orange, green, blue, and purple, respectively), and the many fold states bifurcating from them (thin lines, corresponding color). Self-contact for primary states is marked with a cross, and states beyond this point are dashed. Sample solutions (all rescaled to equal size for clarity) are arranged in ascending order according to the number of localized intrusions and protrusions on the 2π domain (profile labels correspond to branch labels in the bifurcation diagram). Profiles originating in subsequent primary bifurcations are arranged vertically and correspond to $P \approx -20$.

profiles in row labeled 3). As in the case of the fold states for the constrained length (Fig. 5.8), many fold states respect the symmetry of the primary branch they bifurcate from. For example, the second pair of states bifurcating from $m = 3$ features a solution with three intruding folds and a solution with three protruding folds, while $m = 6$ bifurcates to a state with three pairs of antisymmetric folds and a solution with six alternating intrusions and protrusions with overall symmetry under rotations through $2\pi/3$. The different states of alternating symmetric intrusions and protrusions as well as antisymmetric folds resemble the folded states of a floating planar elastic sheet under compression [23], particularly when L is large.

5.10   Asymmetric states

In the unconstrained case, many interesting steady state finger profiles have been reported in the literature [65], but the continuation scheme summarized in Eqs. (4.30) rules out many of them since it can only generate solutions that are symmetric about the x axis. However, using an explicit Runge-Kutta method and numerical shooting, we are able to construct a variety of full-domain solutions which do not obey the previous symmetry restriction imposed by our continuation procedure. As in these previous works, numerical shooting is performed using the gradient of our unconstrained length system such that the only parameters are (L, ℓ^5) with fixed $T = 0$ [65]:

$$\partial_s^4 \phi + \frac{3}{2} \left(\partial_s \phi\right)^2 \partial_s^2 \phi - \ell^5 \left(x \cos\left(\phi\right) + y \sin\left(\phi\right)\right) = 0 \,. \tag{5.8}$$

Figure 5.12 shows resulting examples that are similar in nature to those discovered in previous work (cf.[65]). On the left, mixed mode solutions with no reflection symmetry are shown, while the right shows chiral versions of the localized states displayed in Fig. 5.8. Owing to the reflection symmetry $(\phi, s) \to -(\phi, s)$ of Eq. (5.2), each left-handed solution is accompanied by an identical but right-handed solution. It is important to note that these solution profiles were obtained as solutions to the unconstrained length problem (and hence as a result for the fluid variant of our problem), but they also satisfy the length constrained problem as well (and hence the solid substrate formulation). However, the physical applicability of the solid substrate model, in which the substrate force depends only on the radius of the membrane, is questionable for chiral states due to the necessary highly nonlinear substrate shear involved, which is not accounted for in our minimal model.

To determine the origin of these states in parameter space we implemented a full-circle numerical continuation of the same unconstrained length problem (5.8) in AUTO using periodic boundary conditions for $(\partial_s \phi, \partial_s^2 \phi, \partial_s^3 \phi, x, y)$ with Dirichlet boundary conditions for ϕ at $s = 0, 2\pi$ to pin the phase on the full domain. Additionally, a phase condition was applied to eliminate the rotational freedom of these
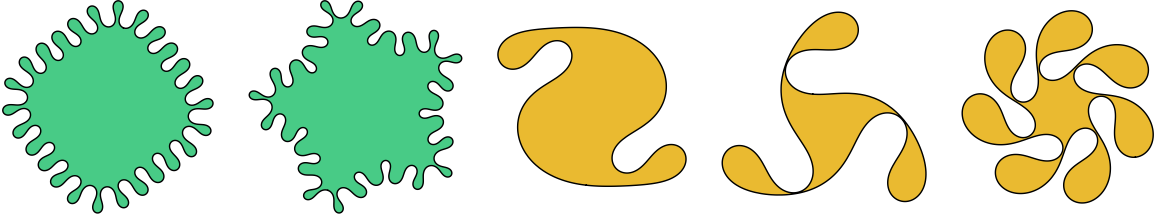
Figure 5.12: Asymmetric states computed on the full domain. From left to right, computed for $P = 0$; mixed modes (green): ($L = 15.714$, $\ell^5 = 8232.56$) and ($L = 15.714$, $\ell^5 = 6257.5$); fold modes (yellow): ($L = 6.283$, $\ell^5 = 650$), ($L = 25.649$, $\ell^5 = 0.916$), and ($L = 15.707$, $\ell^5 = 295$).

full domain states, yielding the extended system:

$$\partial_s^4 \phi + \frac{3}{2} \left(\partial_s \phi \right)^2 \partial_s^2 \phi - \ell^5 \left(x \cos \left(\phi \right) + y \sin \left(\phi \right) \right) + c \partial_s \phi = 0 \,, \tag{5.9}$$

$$\int_0^{2\pi} \left(\partial_s \phi - (\partial_s \phi)_{old} \right) \cdot (\partial_s^2 \phi)_{old} \ ds = 0 \,. \tag{5.10}$$

Following Eq.(2.33), the phase speed c is taken to be an additional freely varying parameter in the continuation in order to satisfy the additional equation provided by the phase condition. In Fig. 5.13, we show numerical continuation of the three-fold chiral state shown in Fig. 5.12, i.e. the output from numerical shooting is used as a starting point for numerical continuation due to the challenges with bifurcation detection from the branch of circle solutions.

As ℓ^5 increases, the size of the chiral extrusions decreases relative to the domain size, consistent with the localized states shown in Fig. 5.6. This suggests that these chiral states are localized states and not wrinkle solutions. It is notable that the degree of asymmetry varies smoothly across the parameter sweep, ranging from a nearly 180° bend at the bottom left to a 45° bend at the top center and top right. This continuous variation in asymmetry is reminiscent of the continuous family of solutions spanning from perfectly symmetry to perfectly antisymmetric found in the planar problem [22]. In addition to the bend at the neck of the localized states, the size of the neck varies as well, tending to zero at the self-contacting states at the top and bottom, while remaining wider for the states in the middle.

In order to better understand the origin of these chiral states, a full-circle numerical continuation of the constrained length problem (3.7) was constructed in AUTO again using periodic boundary conditions for $(\partial_s \phi, \partial_s^2 \phi, \partial_s^3 \phi, x, y)$ with Dirichlet boundary conditions for ϕ at $s = 0, 2\pi$ to pin the phase on the full domain. The same phase condition was applied to eliminate the rotational freedom of these full domain states. For the constrained length problem, the continuation of the first few primary and secondary branches of symmetric and asymmetric states is shown in Fig. 5.14.
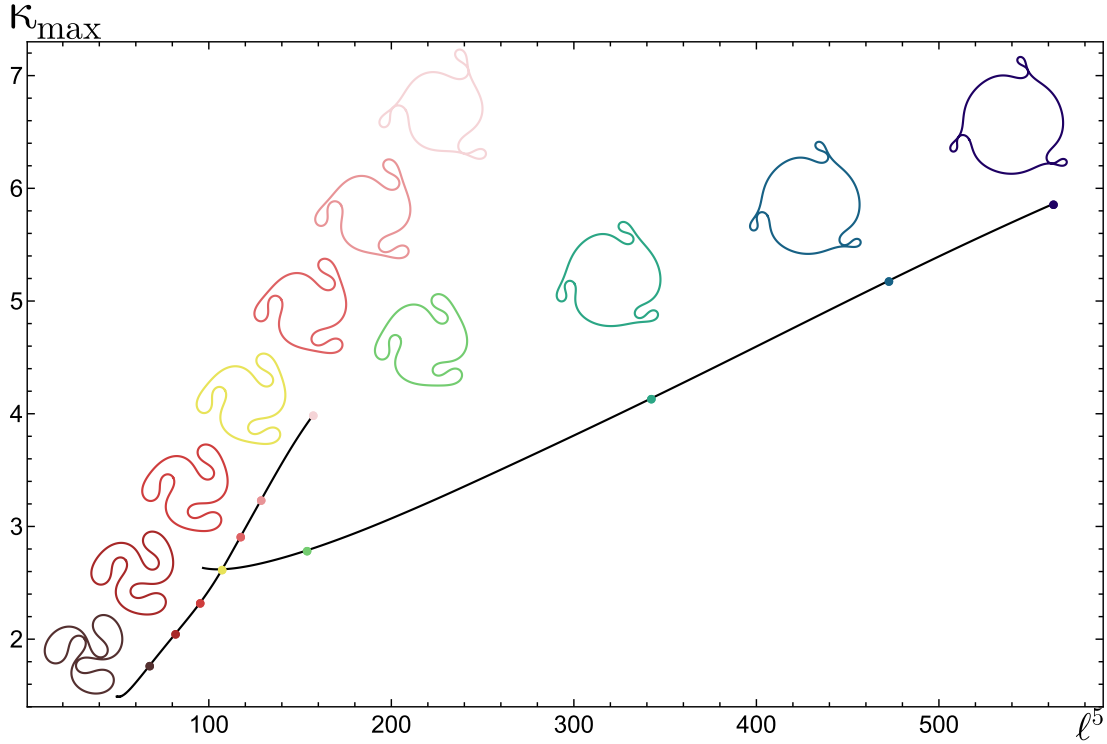
Figure 5.13: Maximum curvature across varying ℓ^5 resulting from numerical continuation of the fourth state from left in Fig. 5.12 ($L = 25.649$, $\ell^5 = 0.916$). Solutions are shown at marked points and continuation is terminated at self-contact.

Figure 5.14 shows that asymmetric states appear via secondary bifurcations from the symmmetric finger states, which is consistent with the fact that all primary states in O(2)-symmetric steady state bifurcation problems are necessarily reflection-symmetric [113]. It has previously been observed that the branches of symmetric intruding and protruding folds emerging from a common bifurcation point coincide in the (T, P) plane [66]. Figure 5.14 shows that in fact *all* secondary branches (intruding, protruding, symmetric, or chiral) emerging from a common bifurcation point coincide in the (T, P) plane although they do not reach self-contact at the same location. The asymmetric states shown here are hypothesized to be multifold chiral variants of the symmetric localized states. Figure 5.14 only depicts the single and double fold localized states, but, by comparison to Figs. 5.8,5.11 which include localized states with arrangements of three or more intrusions or extrusions on the domain, analogous multifold chiral states such as those shown in Fig. 5.12 are expected to also originate in secondary bifurcations from symmetric finger states.
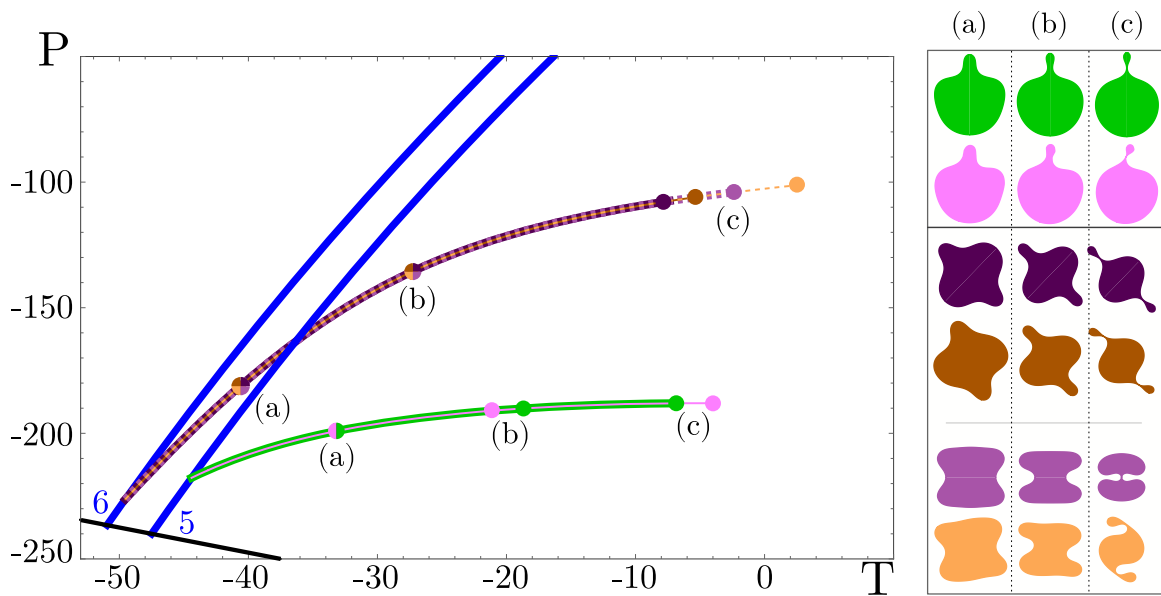
Figure 5.14: Full-domain numerical continuation for $\ell^5 = 576$ in the (T, P) plane showing the first three symmetric and asymmetric fold states emerging simultaneously from secondary bifurcations of the $m = 5$ and $m = 6$ symmetric finger states (blue lines) which in turn bifurcate from the circle states (grey line). The branches of symmetric and asymmetric states coincide in this projection. Color-coded solution profiles corresponding to the locations indicated in the left panel are shown along the right.

Chapter 6

Exact Solutions

The weakly nonlinear analysis performed for $n = 2$ indicated at every order computed that the substrate force strength did not impact the spatial profiles (cf. Eq. 4.27). This hints that the supported elastica model has a connection to the substrate-free model, a significant relation that may allow exact wrinkle solutions to be constructed from the well-known buckled states of the substrate-free case. Intuitively, if the spatial profiles are equivalent for any substrate force, they must be equivalent to the results of zero substrate force. The following results apply equally to both the fluid and solid substrate models discussed in previous sections. In this section, we show that this is indeed possible. Specifically, for this family of substrate forces scaling with r^2, r^4, r^6, the wrinkle profiles are related to the buckled states of the free, unsupported ring [72]. The resulting wrinkle profiles are therefore *universal* for this set of substrate forces, and a parameter space mapping exists which relates the buckled solutions of the classical, unsupported ring problem to the wrinkle solutions for rings with substrate support. This mapping is used to predict bifurcation diagrams for the family of supported-ring problems considered in this thesis, and is validated with numerical continuation.

We rewrite Eq. (4.3) in terms of the curvature, using α_n instead of ℓ^5 as a general parameter to parametrize the dimensionally different substrate forcing for $n = 0, 2, 4, 6$ ($\alpha_0 = 0$):

$$\partial_s^2 \kappa + \frac{1}{2}\kappa^3 - T\kappa - P - \frac{1}{2}\alpha_n r^n = 0,$$
$$\kappa(s) \equiv \partial_s \phi, \quad \partial_s \mathbf{r} = (\cos\phi, \sin\phi). \tag{6.1}$$

Our finding relies on a remarkable feature of weakly nonlinear theory describing periodic perturbations of the circle solution of Eqs. (6.1) in powers of the perturbation amplitude ϵ [66]: as shown in subsection 4.1, for the case $n = 2$, the solution $\phi(s)$ is independent of the force-strength parameter α_2 at every order and the parameters (T, P) are linear in α_2 at every order. To show this, the solution profile (ϕ, x, y) was expanded in powers of ϵ and the parameters T and P in solely even powers of ϵ due

to the rotational symmetry of the solution. The resulting Eqs. (4.27,4.28,4.29) and additional orders confirm this out to $\mathcal{O}(\epsilon^{12})$. For the cases $n = 4$ and $n = 6$, this is no longer true and (ϕ, x, y) and (T, P) all depend nonlinearly on α_n at each order computed as shown in Appendix A. However, the spatial profiles remain strikingly similar across the parameter ranges previously considered.

The absence of any α_2 dependence in the profile (4.27) has significant physical implications, one of the primary contributions of this thesis: wrinkle profiles are *universal* in this sense. Specifically, identical wrinkles profiles occur for substrates of different strengths (different α_2 values), or even for the free ring $\alpha_2 = 0$, for appropriate (different) values of the pressure difference P and tension T. The parameter transformation $(T, P) \to (T, P)$ is linear in α_2 and is therefore equivalent to a one-to-one relation between the pressure difference P and the substrate force measured by α_2. Moreover, since the $\alpha_0 = 0$ problem has closed-form solutions for $\phi(s)$ (described in detail in the following section), so does the problem for any $\alpha_2 > 0$. In the following, we demonstrate these facts, determining the transformation $(T, P) \to (T, P)$ that maps a given wrinkle profile at $\alpha_2 > 0$ into the same profile for the free ring $\alpha_0 = 0$. To do so, we first detail the previously known results for $\alpha_0 = 0$, upon which all other results will be based.

6.1   Free ring problem

The free inextensible elastic ring problem described by (6.1) with $\alpha_0 = 0$ was studied in detail in [69], and is completely integrable [72, 110]. Closed-form analytical solutions are known and allow the construction of branches of highly nonlinear wrinkle solutions up to the point of self-contact as shown in the (T, P) plane in Fig. 5.1a. The wavenumbers m come in in the order $m = 2, 3, 4$, etc. as P increases above zero, a consequence of the absence of an intrinsic length scale. In order to establish the connection between the cases $F = 0$ and $F(r) = \alpha_2 r^2$, we consider the equation for $F = 0$ on a domain of (potentially different) length $2\pi R_2$. This extra degree of freedom is needed to ensure the solutions of both systems are periodic. We define the curvature Q as a function of arclength t and the tension and pressure parameters μ, σ, yielding the familiar equation:

$$\frac{d^2 Q(t)}{dt^2} + \frac{1}{2}Q^3(t) - \frac{\mu}{2}Q(t) - \frac{\sigma}{2} = 0.$$ (6.2)

This equation has the first integral

$$\left(\frac{dQ}{dt}\right)^2 = 2E - \frac{1}{4}Q^4 + \frac{\mu}{2}Q^2 + \sigma Q,$$ (6.3)

where E is a constant of integration. We also note a key geometric identity satisfied by the corresponding radius $\rho(t) \equiv \sqrt{X^2(t) + Y^2(t)}$,

$$\rho^2(t) - \frac{8E + \mu^2}{\sigma^2} - \frac{4Q(t)}{\sigma} = 0, \tag{6.4}$$

first identified in [72]. Equation (6.2) has exact solutions given by [110]

$$Q(t) = \frac{(A\beta + B\alpha) - (A\beta - B\alpha)\mathrm{cn}(ut, k)}{(A + B) - (A - B)\mathrm{cn}(ut, k)}, \tag{6.5}$$

where $\mathrm{cn}(ut, k)$ is the elliptic cosine function with modulus $\sqrt{k}$, $\alpha < \beta \in \mathbb{R}, \gamma = \bar{\delta} \in \mathbb{C}$ are the four roots of the quartic polynomial on the right side of Eq. (6.3), and A, B, u, k are functions of these roots:

$$A = \sqrt{4\eta^2 + (3\alpha + \beta)^2}, \quad B = \sqrt{4\eta^2 + (\alpha + 3\beta)^2}, \quad u = \sqrt{AB}/4, \quad \eta = \frac{\gamma - \delta}{2i}, \tag{6.6}$$

and

$$k = \frac{1}{\sqrt{2}}\sqrt{1 - \frac{4\eta^2 + (3\alpha + \beta)(\alpha + 3\beta)}{[4\eta^2 + (3\alpha + \beta)(\alpha + 3\beta)]^2 + 16\eta^2(\beta - \alpha)^2}}. \tag{6.7}$$

Here $\alpha, \beta, \gamma, \delta$, the roots of the quartic polynomial, are given by:

$$\alpha = -\sqrt{\frac{\omega}{2}} - \sqrt{\mu - \sigma\sqrt{\frac{2}{\omega}} - \frac{\omega}{2}} \tag{6.8}$$

$$\beta = -\sqrt{\frac{\omega}{2}} + \sqrt{\mu - \sigma\sqrt{\frac{2}{\omega}} - \frac{\omega}{2}} \tag{6.9}$$

$$\gamma = \sqrt{\frac{\omega}{2}} + \sqrt{\mu + \sigma\sqrt{\frac{2}{\omega}} - \frac{\omega}{2}} \tag{6.10}$$

$$\delta = \sqrt{\frac{\omega}{2}} - \sqrt{\mu + \sigma\sqrt{\frac{2}{\omega}} - \frac{\omega}{2}}, \tag{6.11}$$

where $\alpha, \beta \in \mathbb{R}$ and $\gamma = \bar{\delta} \in \mathbb{C}$ are complex, and ω is a function of the parameters μ, σ, E,

$$\omega = \frac{\left[\mu + \left(3(3^2\sigma^2 + \sqrt{\chi}) - \mu\left(\mu^2 + 2^33^2E\right)\right)^{1/3}\right]^2 - 2^33E}{3\left(3(3^2\sigma^2 + \sqrt{\chi}) - \mu(\mu^2 + 2^33^2E)\right)^{1/3}}, \tag{6.12}$$

and

$$\chi = 3\left(2^3E\left[(\mu^2 + 8E)^2 - 3^22\mu\sigma^2\right] - \sigma^2(2\mu^3 - 3^3\sigma^2)\right). \tag{6.13}$$

72
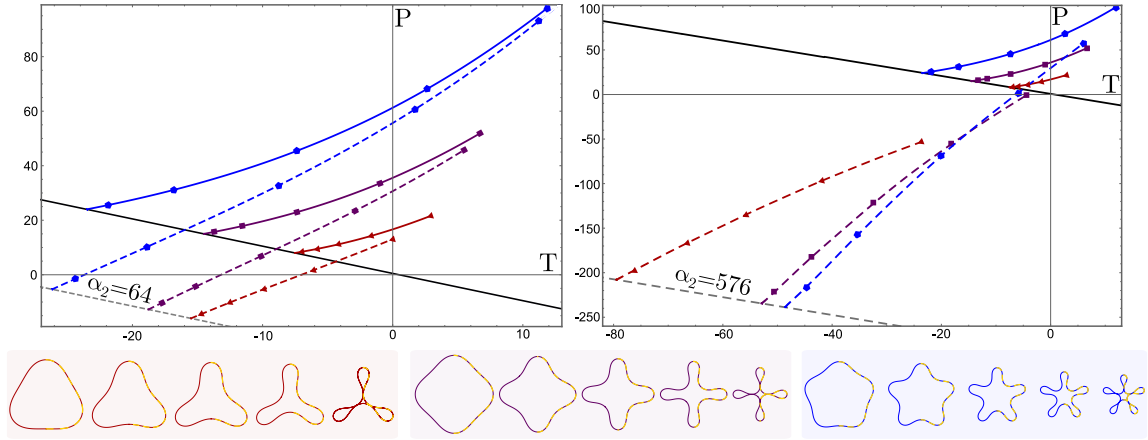
Figure 6.1: Top: Numerical continuation for two values of α_2 showing solution branches in the (T, P) plane for $R_1 = 1$ and wavenumbers $m = 3$ (red triangles), $m = 4$ (purple squares), and $m = 5$ (blue pentagons). Solid lines: $\alpha_0 = 0$ (see Fig. 5.1a); dashed lines $\alpha_2 = 64$ (left) and $\alpha_2 = 576$ (right). Colored markers on the dashed lines map to the corresponding markers on the solid lines. Bottom: Color-coded solution profiles at points indicated in the top panels. The solid profiles show the analytical solution while the superposed orange dashed profiles are from numerical continuation (right half of each profile). The solutions agree to within numerical accuracy. In each case, the final profile corresponds to self-contact.

Other forms of the solution exist, but these necessarily self-intersect and are hence nonphysical [110].

The pressure parameter σ may be positive or negative since Eq. (6.2) remains invariant under $(Q, \sigma) \to (-Q, -\sigma)$ and changing the sign of the curvature does not alter the physical spatial profile. The choice that $\alpha, \beta \in \mathbb{R}$ and $\gamma, \delta \in \mathbb{C}$ requires that $\sigma < 0$ and therefore the association $\sigma \propto -P$ such that a positive net external pressure load P leads to buckling solutions. If, instead, $\sigma > 0$ such that $\alpha, \beta \in \mathbb{C}$ and $\gamma, \delta \in \mathbb{R}$, the solution remains physically valid provided the pressure is redefined such that $\sigma \propto P$. Therefore, the solution is physical and applies in both cases assuming the roots are appropriately relabeled and the pressure redefined.

With these results, finding an exact physically realizable solution to Eq. (6.2) then reduces to finding combinations of the three parameters μ, σ and E which yield closed, non-self-intersecting curves when employed in Eq. (6.5). This system and these results will be referred to as the *pure buckling* or *free-ring* problem.

6.2 Rescaling: r^2

Adding an appropriate multiple of (6.4) to Eq. (6.2) and rescaling to map it onto the variables used for $n = 2$ via

$$Q = \frac{\kappa}{R}, \quad Q^3 = \frac{\kappa^3}{R^3}, \quad \frac{d^2Q}{dt^2} = \frac{1}{R^3}\frac{d^2\kappa}{ds^2}, \quad \rho = Rr, \tag{6.14}$$

where $R = R_2/R_1$ is a scaling factor that maps the domain length to 2π in the variable $s = t/R$, we obtain:

$$\frac{d^2\kappa(s)}{ds^2} + \frac{1}{2}\kappa^3(s) - R^2\left(\frac{\mu}{2} - \alpha_2\frac{2}{\sigma R^5}\right)\kappa(s) - R^3\left(\frac{\sigma}{2} - \alpha_2\frac{8E + \mu^2}{2\sigma^2 R^5}\right) - \frac{1}{2}\alpha_2 r^2(s) = 0. \tag{6.15}$$

Therefore, a one-to-one correspondence between Eqs. (6.1) with $n = 2$ and (6.2) exists under the mapping:

$$T = \frac{\mu R^2}{2} - \frac{2\alpha_2}{\sigma R^3}, \tag{6.16a}$$

$$P = \frac{\sigma R^3}{2} - \frac{8E + \mu^2}{2\sigma^2 R^2}\alpha_2, \tag{6.16b}$$

$$r^2(s) = \frac{8E + \mu^2}{\sigma^2 R^2} + \frac{4\kappa(s)}{\sigma R^3}. \tag{6.16c}$$

 As a result, the closed-form analytical solutions of the pure buckling problem defined in Eq. (6.2) also apply to the substrate supported problem defined in Eqs. (6.1) with $n = 2$ and therefore the wrinkling of rings subject to any force of the form $F \propto r^2$, cf. [74] are described by the pure buckling problem results. The terms independent of α_2 in Eqs. (6.16a, 6.16b) correspond to the substrate-free tension and pressure. The remaining terms, scaling linearly with α_2, provide the additional tension and pressure needed to counteract the substrate force such that an equivalent spatial profile is produced. The dependence of T and P on both σ, μ, and α_2 therefore leads to a reordering of the branches in the (T, P) plane.

These analytical results for $\alpha_2 > 0$ obtained with the use of the above mapping are confirmed using numerical continuation of (6.1) in AUTO [95] to show that these correspond to the analytical result (6.5) at appropriate locations in the (T, P) plane. To do so, (6.16) is solved using numerically generated values of (x, y, κ) at known (T, P) to obtain the values of μ, σ, E needed to construct the corresponding analytical solution (6.5). The mapping in Eqs. (6.16a, 6.16b) is then applied in order to compare the parameter-space location of these solutions with those of the free-ring problem or to map the free-ring solutions to the corresponding location in parameter space for the substrate-supported ring problem with nonzero α_2. The results for $n = 2$ and two values of α_2 are shown in Fig. 6.1 for comparison with Fig. 5.1a and demonstrate perfect agreement between numerical continuation and the closed-form solutions of

the free-ring problem at the corresponding points in the (T, P) plane. Figure 6.2 provides a quantitative comparison between these results and demonstrates excellent agreement within numerical tolerances between analytical and numerical results, confirming this geometric *universality*.
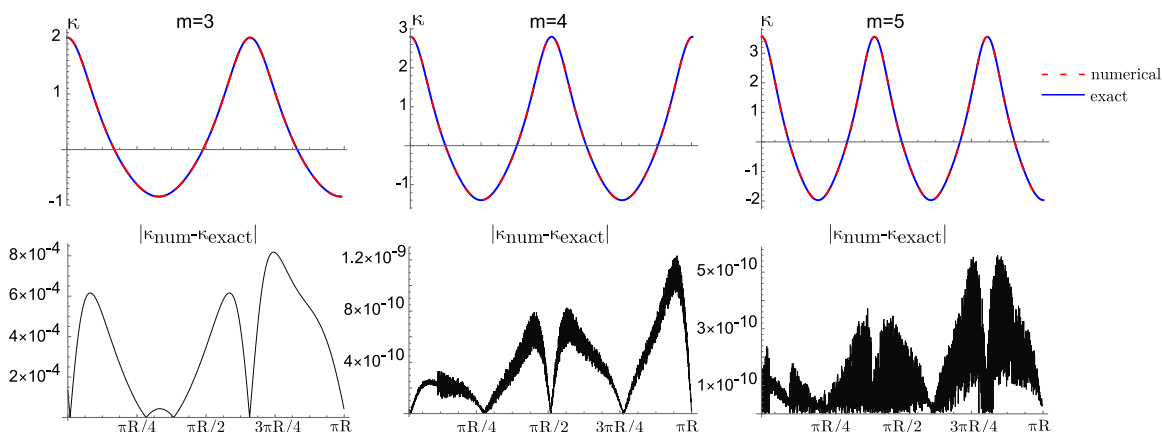
Figure 6.2: Top: Exact (blue) solution for the curvature $\kappa(s)$ over half the domain for $\alpha_2 = 576$ and $R = 3.41083$ overlaid with the corresponding numerical result (red). Bottom: absolute difference between the exact and numerically computed $\kappa(s)$. The error in each case is consistent with the numerical tolerances used in the computation. For the analytical solution the corresponding parameters are as follows: $(m = 3)$ $\mu = 0.50778, \sigma = 1.09113, E = 0.43376$; $(m = 4)$ $\mu = 1.15369, \sigma = 2.61283, E = 1.74328$; $(m = 5)$ $\mu = 2.04365, \sigma = 4.93013, E = 4.76243$. All three solutions correspond to first self-contact.

6.3   Higher order forcing: $n = 4, 6$

Remarkably, this universality extends beyond $F \propto r^2$. An analogous procedure, involving the addition of powers of the identity (6.4) to Eq. (6.2), can be used to map the free-ring solutions onto a broader family of substrate forces including those for which $n = 4$ or $n = 6$, or in which the force is a result of a combination of terms involving $n = 2, 4, 6$. This mapping requires a translation and rescaling of the curvature, yielding different closed-form solutions with distinct spatial profiles to $n = 2$. For this reason, the connection to the pure buckling problem is not as direct as the $n = 2$ comparison, but it shows that the free-ring solutions may be used to construct new analytical solutions for both $n = 4$ and $n = 6$. This mapping process is detailed below.

6.3.1 Rescaling: r^4

We can repeat the above rescaling procedure done for $n = 2$, adding different terms which are identically zero to the pure buckling equation. For example, squaring the geometric identity (6.4) and adding the result to (6.2) results in

$$\frac{d^2Q(t)}{dt^2} + \frac{1}{2}Q^3(t) - \frac{\mu}{2}Q(t) - \frac{\sigma}{2} - \frac{1}{2}\frac{\alpha_4}{R^7}\left(\rho^4(t) - (A + BQ(t))^2\right) = 0,\qquad(6.17)$$

where $A \equiv \frac{8E+\mu^2}{\sigma^2}$ and $B \equiv \frac{4}{\sigma}$. This equation has a term quadratic in Q which does not match the form of (6.1), but by writing $Q = \tilde{Q} + C_4$ we can eliminate this term with the choice

$$C_4 = -\frac{\alpha_4 B^2}{3R^7}.\qquad(6.18)$$

The same rescaling as in Eq. (6.14) can now be performed to obtain

$$\kappa_{ss} + \frac{1}{2}\kappa^3 - \left(\frac{\mu R^2}{2} - \frac{\alpha_4 AB}{R^5} + \frac{\alpha_4^2 B^4}{6R^{12}}\right)\kappa - \left(\frac{\sigma R^3}{2} - \frac{\alpha_4}{2R^4}\left(A^2 + \frac{\mu B^2}{3}\right) + \frac{A\alpha_4^2 B^3}{3R^{11}} - \frac{\alpha_4^3 B^6}{27R^{18}}\right) - \frac{1}{2}\alpha_4 r^4 = 0.\qquad(6.19)$$

The mapping to the original $n = 0$ problem is obtained by identifying T, P with the quantities in the first and second parentheses, respectively, and incorporating the definitions for A, B:

$$T = \frac{\mu R^2}{2} - \frac{4\alpha_4(\mu^2 + 8E)}{R^5\sigma^3} + \frac{128\alpha_4^2}{3R^{12}\sigma^4},\qquad(6.20)$$

$$P = \frac{\sigma R^3}{2} - \frac{\alpha_4}{R^4\sigma^4}\left(\frac{(\mu^2 + 8E)^2}{2} + \frac{8\mu\sigma^2}{3}\right) + \frac{64\alpha_4^2(\mu^2 + 8E)}{3R^{11}\sigma^5} - \frac{4096\alpha_4^3}{27R^{18}\sigma^6}.\qquad(6.21)$$

This procedure demonstrates that when $n = 4$ the wrinkle solutions of (6.1) and the buckling solutions of (6.2) are still identical, to within an additive constant in the curvature, provided the parameters (T, P) are adjusted accordingly.

With $Q(t)$ given by (6.5) as the solution to the pure buckling problem (6.2), we define the solution to the $\alpha_4 > 0$ problem via κ where $\kappa = R(Q - C_4)$. To maintain a closed physical solution, we once again find parameters for $Q(t; \mu, \sigma, E)$ but this time we require that $\int_0^{2\pi R}\kappa ds = \int_0^{2\pi R}R\left(Q + \frac{16\alpha_4}{3\sigma^2 R^7}\right)ds = 2\pi$. Profiles of κ and the corresponding Q from which it is derived are shown in Fig. 6.3. Only κ is closed.

6.3.2 Rescaling: r^6

Proceeding in a similar manner, we now add a cube of the geometric identity (6.4) to Eq. (6.2), obtaining

$$\frac{d^2Q(t)}{dt^2} + \frac{1}{2}Q^3(t) - \frac{\mu}{2}Q(t) - \frac{\sigma}{2} - \frac{1}{2}\frac{\alpha_6}{R^7}\left(\rho^6(t) - (A + BQ(t))^3\right) = 0,\qquad(6.22)$$
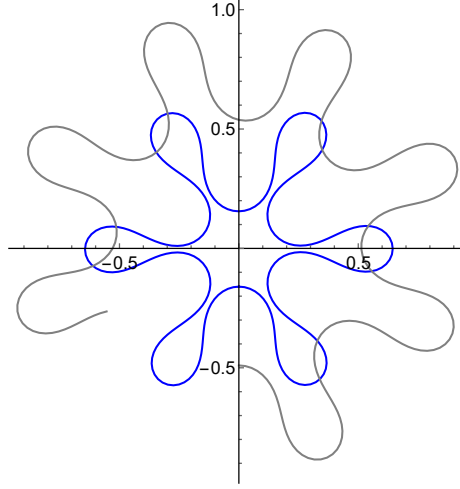
Figure 6.3: Spatial profile resulting from the analytical solution $\kappa(s)$ solving (6.1) for $\alpha_4 = 576$ (blue) and that from $Q(t)$ solving (6.2) (gray) for the same parameters: $\mu = 0.52, \sigma = 100.45, E = 694, R = 1.14176$. Owing to the translation term relating the curvatures $\kappa(s)$ and $Q(t)$, only κ closes smoothly.

where A, B are as before. The problem may be transformed into the form (6.1) with $n = 6$ via the transformation:

$$Q = \frac{\kappa}{\gamma R} + C, \quad t = sR, \quad \rho = Rr, \quad \gamma = \frac{1}{\sqrt{1 + 64\alpha_6/R^9\sigma^4}}, \qquad (6.23)$$

$$C_6 = -\frac{\alpha_6 16(8E + \mu^2)}{64\alpha_6\sigma + R^9\sigma^4}. \qquad (6.24)$$

Inserting the definitions of A, B from above, we obtain:

$$\kappa_{ss} + \frac{1}{2}\kappa^3 - \kappa\frac{(\frac{1}{2}R^2(\mu(\sigma^8 R^{18} + 4096\alpha_6^2\sigma^2 + 128R^9\alpha_6\sigma^5) - 768\alpha_6(8E + \mu^2)^2(\alpha_6 + \frac{R^9\sigma^3}{64}))))}{(R^9\sigma^4 + 64\alpha_6\sigma)^2}$$

$$- \frac{1}{2}\sqrt{1 + \frac{64\alpha_6}{R^9\sigma^3}}\left(\sigma R^3 + \frac{16R^3\alpha_6\mu(8E + \mu^2)}{(64\alpha_6\sigma + R^9\sigma^4)} + \frac{(8E + \mu^2)^3(-4096R^3\alpha_6^3 + R^{21}\alpha_6\sigma^6)}{(64\alpha_6\sigma + R^9\sigma^4)^3}\right)$$

$$- \frac{1}{2}\sqrt{1 + \frac{64\alpha_6}{R^9\sigma^3}}\alpha_6 r^6 = 0. \qquad (6.25)$$

We use the transformations described above for $n = 2, 4, 6$ to obtain exact solutions of (6.1) in terms of the exact solutions (6.5) of the pure buckling problem, and compare the results with numerical continuation results in the following section. Beyond the third power of the geometric identity, cross terms are introduced which can not be absorbed by a simple translation or rescaling. For this reason, the process of adding powers of the geometric identity may not be continued beyond this point, and results for $n > 6$ are not considered in this thesis.

6.3.3 Higher order forcing: results

With these results for exact solutions of the $n = 2, 4, 6$ and the mappings relating them to $n = 0$, we now compare the systems. Figure 6.4 shows overlays of the resulting analytical and numerical solutions for these values of n.
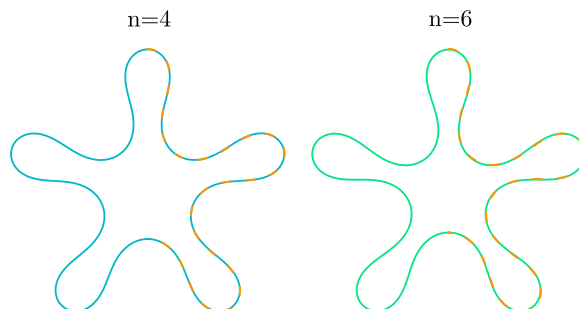
Figure 6.4: Analytical solutions ($n = 4$ blue, $n = 6$ green) overlaid with numerical solutions (orange) for $\alpha_{4,6} = 500$ and $R_1 = 1$.

The presence of an additive constant in the curvature results in spatial solutions that are no longer exactly identical, although in the limit of large R or m or small α_n, the additive term is heavily suppressed as a consequence of the form of the translation term (cf. Eqs. 6.18,6.24) and the solutions approach a universal profile. In Fig. 6.5 we show how the geometrical features for $n = 2, 4, 6$ compare across a wide range of α_n and m. The above construction also suggests a straightforward extension to substrate forces of the form $F \sim \sum \alpha_n r^n$, albeit with a more complicated $(T, P) \to (T, P)$ mapping, allowing analytical solution of the wrinkle problem with more complex (and more realistic) substrate forces.

Although the wrinkle profiles are the same, the (T, P) mapping modifies the physical response of the system under study as the pressure load increases. In the free-ring problem ($F = 0$) the wavenumbers m set in monotonically for $P > 0$ as P increases so the first mode to bifurcate from the circle branch is the $m = 2$ (buckling) mode. As a consequence of the absence of an intrinsic length scale, none of the primary branches ($m = 2, 3, \dots$) undergoes any secondary bifurcations right up to self-contact. However, when this length scale is present ($\alpha_n > 0$) wrinkle branches set in at different parameter values as shown in Fig. 6.6 and may set in in a different order, and the first mode to bifurcate as P increases may have $m > 2$ (wrinkle mode) and set in at negative P.

As seen in Fig. 6.5, the effect of the substrate on the spatial profiles for $n = 4, 6$ is heavily suppressed and only begins to become discernible in the bifurcation diagram for $\alpha_n \approx 1000$, where the solutions still appear nearly identical spatially. To make differences in the spatial profiles discernible, even higher values of α_n are necessary, which makes numerical continuation to highly nonlinear wrinkling solutions numerically unstable. To circumvent this, homotopy is applied. The exponent of r may
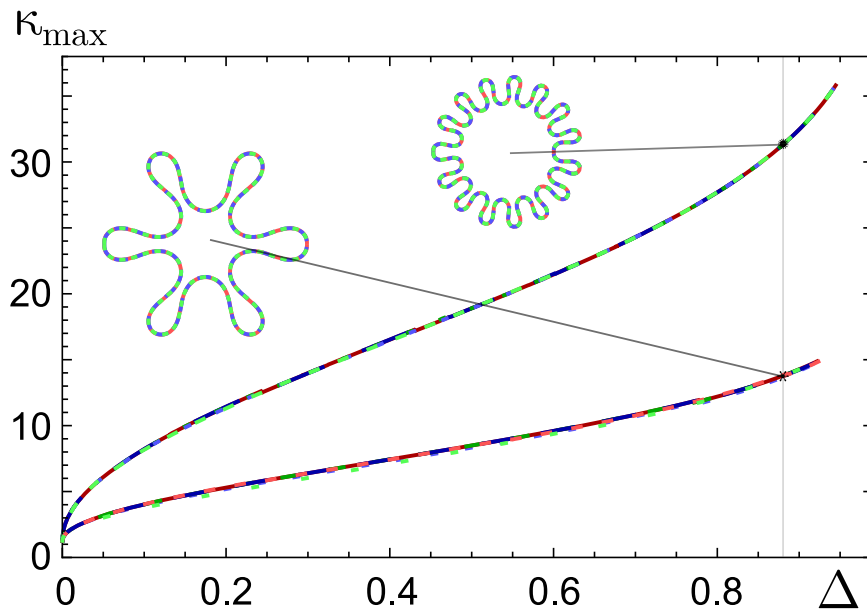
Figure 6.5: The compression $\Delta \equiv 1 - A/\pi$ for area A plotted against maximal curvature κ_{max} for $m = 6$ and $m = 15$. Solutions for $n = 2$ (dark red: $\alpha_2 = 10$ and light red: $\alpha_2 = 1000$), $n = 4$ (dark blue: $\alpha_4 = 10$ and light blue: $\alpha_4 = 1000$), and $n = 6$ (dark green: $\alpha_6 = 10$ and light green: $\alpha_6 = 1000$). Solutions are shown at $A = 0.4$ ($\Delta \approx 0.87$) and $R_1 = 1$.
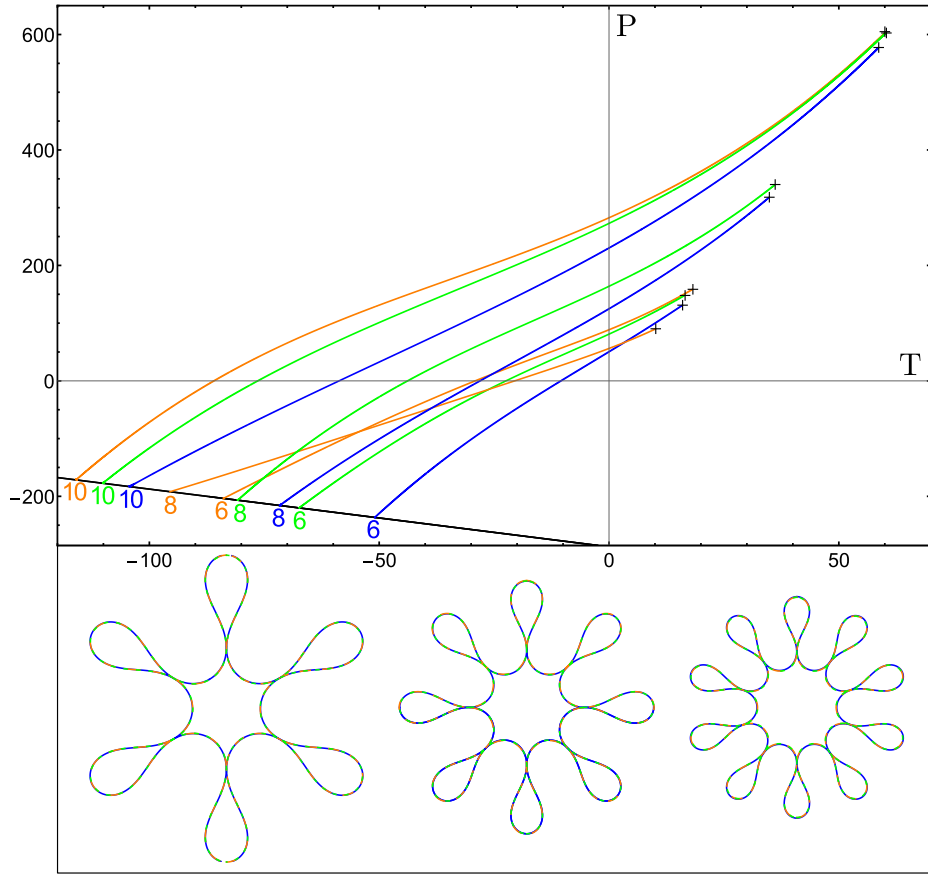
Figure 6.6: Primary wrinkling branches for $\alpha_{2,4,6} = 576$ in blue, green, and orange respectively. Solutions are shown at the point of self-contact (crosses).
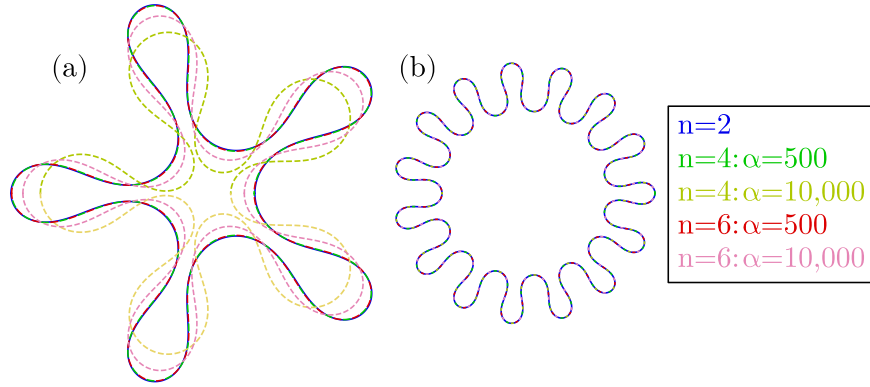
Figure 6.7: Solutions with $m = 5$ (a) and $m = 15$ (b) for $n = 2, 4, 6$ across a range of α values.

be taken as a continuation parameter d, initialized at $d = 2$ where continuation is straightforward and the spatial profile is independent of α_2. Continuation is performed out to the point of self-contact with d fixed at $d = 2$ and α_2 sufficiently small ($\lesssim 2000$). From this point, d is taken to be the primary bifurcation parameter such that the free parameters are (d, T, x_0, x_1), and continued to $d = 4$ or $d = 6$. Then the substrate parameter α_4 and α_6 are continued to the desired larger values. Finally, the resulting states are continued back down to the circle branch where possible in (P, T, x_0, x_1) with $d = 4, 6$. In this way, solutions and bifurcation diagrams may be constructed for $n = 4, 6$. Figure 6.7 compares the resulting spatial profiles. As α_n increases, the lobes become wider and the center of the shapes shrink. This effect is pronounced for low wavenumbers but heavily suppressed for high m. This qualitatively matches the findings from the rescalings for r^4 and r^6 where the translation to the buckling curvature solution scales inversely with σ, which tends to an increase in the wavenumber.

For a sufficiently weak substrate force, all secondary bifurcations occur beyond the point of self-intersection and are ignored as unphysical. However, as α_n increases, these secondary bifurcations move down along the wrinkle branches, eventually passing the point of self-contact to become physical solutions. Therefore, once α_n is large enough, secondary bifurcations take place prior to self-contact, yielding *folds* if the resulting secondary branch does not connect to another wrinkle branch or *mixed modes* if it does. Therefore, the presence of folds and mixed modes is predicated on substrate support despite the wrinkle solution mapping between substrate-free and substrate-supported systems previously noted.

When $n = 2$, the mixed modes are characterized by the simultaneous presence of two distinct wavenumbers m_1, m_2 whenever they connect primary branches with wavenumbers m_1 and m_2 [66]. When $n = 4$, similar structures are observed. However, the structure of secondary mixed mode branches becomes more complicated for $n = 6$. In this case, branches with a wavenumber below the critical wavenumber de-

81
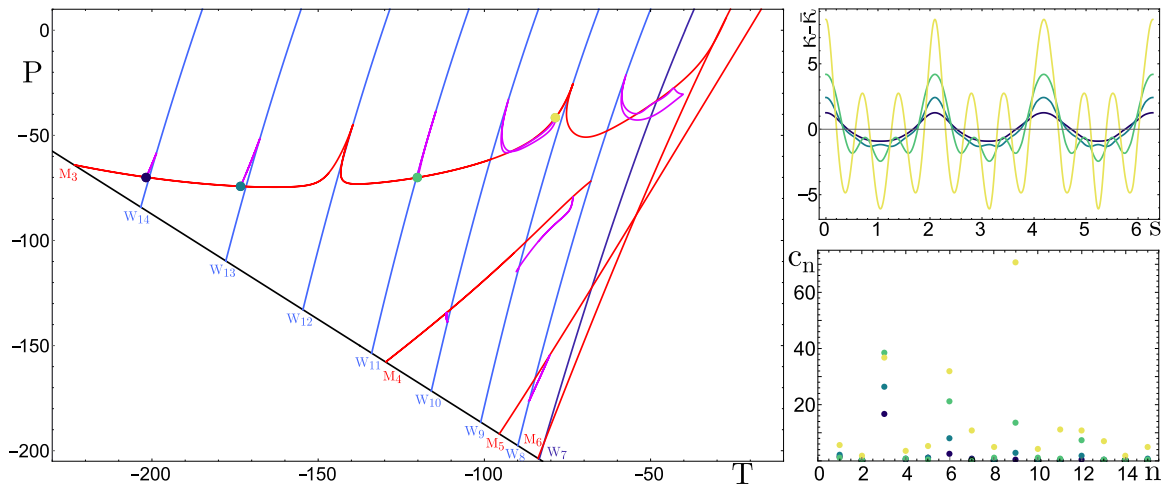
Figure 6.8: Left: a bifurcation diagram highlighting secondary mixed mode bifurcations for $\alpha_6 = 576$ (localized state branches omitted). Primary branches (W_m) are displayed in dark blue ($m = m^*$) and light blue ($m > m^*$). Branches which initiate with $m < m^*$ (M_m) are shown in red, although they develop higher wavenumber modes of increasing amplitude as they become more nonlinear. Mixed mode connections between these states are shown in purple. Top right: curvature solutions at marked points along M_3 are shown, centered about their mean. The development of the profiles highlights the presence of an increasing number of integer multiples of the original wavenumber $m = 3$. Bottom right: corresponding discrete Fourier transform computed via $c_n = \frac{1}{\sqrt{N}} \sum_{r=1}^{N} u_r e^{2\pi i(r-1)(n-1)/N}$ where each dataset $\{u_r\}$ has length $N = 800$.

velop additional modes as they become more nonlinear. These branches also connect directly to some primary branches, and mixed modes branches bifurcating from them have additional wavenumbers. For example, in Fig. 6.8, the M_3 branch bifurcates from the circle branch with sole wavenumber $m = 3$, but unlike for $\alpha_{2,4} = 576$, when $\alpha_6 = 576$, it develops additional, competing modes as it becomes more nonlinear. This branch connects directly to primary branches with wavenumbers which are integer multiples of $m = 3$, terminating on the M_6 branch, the lowest multiple possible, which is also a wavenumber below $m^* = 7$. It connects via mixed mode branches to primary branches which do not have solutions of integer multiple wavenumbers. These mixed mode branches can have three or more wavenumbers, in contrast to the mixed modes of only two wavenumbers seen previously for $\alpha_{2,4}$. A similar process is seen for M_4 which connects directly to W_8 and via mixed modes to $W_{9,10}$.

The structure of bifurcations to fold state branches are consistent across $n = 2, 4, 6$, although the spatial profiles are no longer exactly the same and have no counterpart in the free-ring problem with $F = 0$. Figure 6.9 shows examples of fold states for $n = 2, 4, 6$ with intrusion and extrusion. As expected for strongly nonlinear solutions, the scale of the localized states relative to the domain size increases with
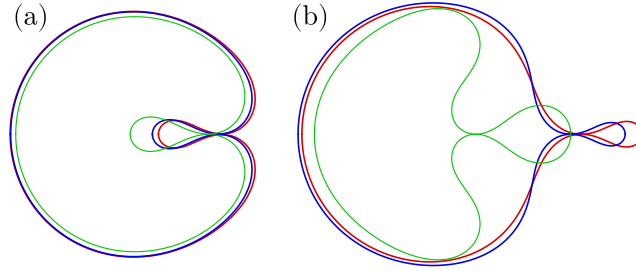
Figure 6.9: Secondary fold states for $\alpha_n = 576$ and $R_1 = 1$ at the point of self-contact bifurcating from the first primary branch in each case: $n = 2$ (red, bifurcates from $m = 5$), $n = 4$ (blue, bifurcates from $m = 6$), and $n = 6$ (green, bifurcates from $m = 7$). (a) Fold states with intrusion. (b) Fold states with extrusion. The profiles are strongly dependent on the exponent n.

n.

Although no theory has been developed for odd values of n, the bifurcation diagrams for $n = 3, 5$ are qualitatively comparable to $n = 2$ and $n = 4$, comprised of branches of primary, single wavenumber solutions and secondary branches of fold or mixed mode solutions. The solution profiles of these states are also comparable, although not identical, to any of the exact analytical results obtained.

Despite the existence of an intrinsic length scale when $\alpha_n > 0$, $n \geq 2$, equations of the form (6.1) possess *identical* closed-form solutions when $n = 0, 2$ and *near-identical* closed-form solutions when $n = 4, 6$. In both cases, these solutions occur at different locations in parameter space. This remarkable result for $n = 0, 2$ is consistent with the perturbation theory result that ϕ is independent of α_2 to all orders (cf. Eq. (4.27)), while T, P do depend on α_2 but only linearly (cf. Eqs. (4.28) and (4.29)). These facts suggest that we may differentiate Eq. (6.1) with respect to α_2, yielding

$$T_{\alpha_2}\kappa + P_{\alpha_2} + \frac{1}{2}r^2 = 0\,, \tag{6.26}$$

where $T_{\alpha_2}, P_{\alpha_2}$ are *constants*, an equation that is equivalent to the geometric identity (6.16c). Thus the mapping of (6.1) onto the free-ring problem applies to the primary wrinkle solutions for which ϕ is independent of α_2 but not to secondary states where this condition no longer holds. The supported ring problem (6.1) is therefore integrable in this limited sense as a consequence of the geometric constraints on in-plane deformations of closed elastica.

Chapter 7

Structure of primary equation: $n = 2$

7.1 Spatial dynamics: reversibility

The primary system may be defined as a five dimensional vector field in the variables $(\phi, \kappa, \partial_s \kappa, x, y)$ and has several noticeable symmetries which have been previously discussed. A more subtle feature of this system for $n = 2$ is its reversibility. This property and its implications are described below.

We consider the steady state form of our system expressed in a system of first order differential equations:

$$\frac{d\boldsymbol{u}}{ds} = \boldsymbol{f}(\boldsymbol{u}) \tag{7.1}$$

and seek a C^r map $G : \mathbb{R}^n \to \mathbb{R}^n$ where G is an involution: $G \circ G = I$ (identity). Taking the arclength parametrization s as our 'time', if G also satisfies

$$\frac{d}{ds}(G(\boldsymbol{u})) = -\boldsymbol{f}(G(\boldsymbol{u})) \tag{7.2}$$

then the vector field $\boldsymbol{f}$ is reversible [85]. Reversibility of the vector field implies the spatial spectrum of the Jacobian of the system is symmetric about the real and imaginary axes, a strong constraint.

For $s \in [0, 2\pi]$, our vector field takes the five dimensional form

$$\frac{du_1}{ds} = u_2 \tag{7.3}$$

$$\frac{du_2}{ds} = u_3 \tag{7.4}$$

$$\frac{du_3}{ds} = -\frac{1}{2}u_2^3 + Tu_2 + P + \frac{l^5}{2}\left(u_4^2 + u_5^2\right) \tag{7.5}$$

$$\frac{du_4}{ds} = \cos(u_1) \tag{7.6}$$

$$\frac{du_5}{ds} = \sin(u_1). \tag{7.7}$$

We construct an involution that satisfies the reversibility condition. If we assume that our map includes the property $G : u_1 \to -u_1$, this immediately implies it cannot also have the property $G : u_2 \to -u_2$. We can see this by considering Eqs. (7.2, 7.3).

$$\frac{d}{ds}(-u_1) = -G(u_2) \tag{7.8}$$

This is only satisfied if G acts as the identity to u_2. This then implies $G : u_3 \to -u_3$ since, from Eq. 7.4 we need

$$\frac{d}{ds}(u_2) = -G(u_3) \tag{7.9}$$

Finally, our differential equation becomes

$$\frac{d}{ds}(-u_3) = -\left(-\frac{1}{2}(u_2)^3 + Tu_2 + P + \frac{l^5}{2}(u_4^2 + u_5^2)\right) \tag{7.10}$$

We can see the equation is left unchanged. Lastly, for completeness we note that we need $G : u_4 \to -u_4$ and $G : u_5 \to u_5$ since $\cos(\phi)$ is even in ϕ and $\sin(\phi)$ is odd. Thus, our operator is given by $G(u_1, u_2, u_3, u_4, u_5) = (-u_1, u_2, -u_3, -u_4, u_5)$. Since $G \circ G = I$, we've proven our vector field is reversible. This result implies the spatial spectrum of the Jacobian of our system is symmetric about the real and imaginary axes. The spectrum without any phase conditions is shown in Fig. 7.1. Many eigenvalues occur at the origin in the complex plane as a consequence of the symmetries.
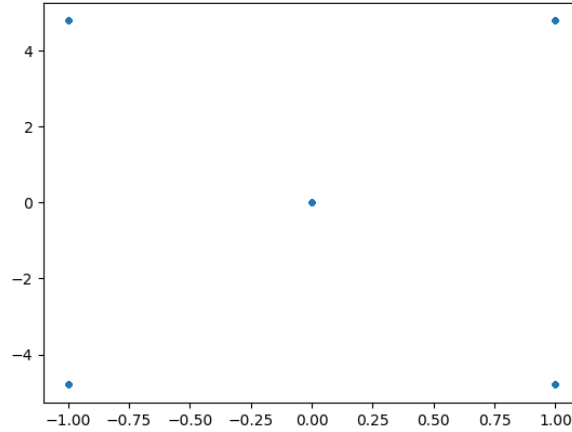
Figure 7.1: Complex spatial spectrum of the Jacobian of the spatial system evaluated about the circle state: Eqs. (7.3–7.7).

It is the presence of these zero eigenvalues which creates substantial challenges for numerical continuation and bifurcation detection.

7.2 Normal form of the bifurcation to wrinkle solutions

We will now show that the normal form of the primary wrinkling bifurcation is given by a pitchfork of revolution. This result may be determined purely from symmetry considerations. Near onset, we write a solution of wavenumber m as $\kappa = Re[a_m e^{im\theta}] + \dots$ for a complex amplitude a_m. The physical nature of the problem suggests rotation and reflection symmetries must commute with any equation which a_m satisfies. Indeed, these symmetries were exploited when implementing the numerical continuation in previous sections. Physically, a wrinkled state may be rotated and continue to satisfy the governing equation. Therefore, κ has the symmetry $\theta \to \theta + \theta_0$. This implies that

$$a_m \to a_m e^{im\theta_0} \tag{7.11}$$

must not violate the equation. Similarly, a wrinkled state may be reflected about a bisecting axis, which is equivalent to $\theta \to -\theta$. This implies that

$$a_m \to \bar{a}_m \tag{7.12}$$

must not violate the equation. Following [114], these constraints on a_m require

$$\dot{a}_m = f(|a_m|^2, P - P_c)a_m \, , \tag{7.13}$$

where f must be real and its argument phase invariant due to reflection symmetry and the overall factor a_m is required to match the phase of $\dot{a}_m$ due to rotation symmetry. The parameter $P - P_c$ encodes the distance from onset (P_c) of the wrinkle state instability. We Taylor expand $f(|a_m|^2, P - P_c)$ in the near onset limit $P - P_c \ll 1$, and take only the leading order terms to obtain:

$$\dot{a}_m = (P - P_c)a_m + c_1|a_m|^2 a_m + ... \tag{7.14}$$

Lastly, we write the complex a_m in terms of a real amplitude ρ and a phase ϕ: $a_m = \rho e^{i\phi}$, yielding

$$\dot{\rho}e^{i\phi} + i\rho\dot{\phi}e^{i\phi} = (P - P_c)\rho e^{i\phi} + c_1\rho^3 e^{i\phi}, \tag{7.15}$$

such that the steady-state instability is given by

$$\dot{\rho} = (P - P_c)\rho + c_1\rho^3 \tag{7.16}$$

$$\dot{\phi} = 0. \tag{7.17}$$

Equation 7.16 defines a subcritical pitchfork bifurcation for $c_1 > 0$ and a supercritical pitchfork bifurcation for $c_1 < 0$. Equation 7.16 indicates that the phase $\phi = \phi_0$, an arbitrary constant corresponding to the (arbitrary) rotation of the solution. For this reason, the pitchfork branch may be rotated arbitrarily, and the bifurcation is a pitchfork of revolution (cf. Fig. 2.2b). The steady state solutions are given by $(\dot{\rho}, \dot{\phi}) = (0, 0)$:

$$\rho^2 = \frac{-(P - P_c)}{c_1}, \quad \phi = \phi_0 \tag{7.18}$$

such that the solution is given by

$$\kappa = Re\left[\sqrt{\frac{-(P - P_c)}{c_1}}e^{im\theta + \phi_0}\right]. \tag{7.19}$$

where we note that the values of P_c and c_1 are both functions of the wavenumber m.

The sign of c_1 may be understood by comparison of the pitchfork bifurcation with results obtained by numerical continuation. Specifically, considering the steady solution in Eq. 7.18, we have

$$\frac{dP}{d\rho^2}\Big|_{\rho^2=0} = -2c_1. \tag{7.20}$$

As a primary wrinkled state with $m > 2$ bifurcates from the circle state, the pressure difference increases with increasing amplitude of the wrinkled state as shown in Fig. 4.2. Therefore, we require $c_1 < 0$, and the bifurcation is supercritical. However, for $m = 2$ and $\ell^5 \geq 81$, P decreases with increasing pattern amplitude, and c_1 must be positive, implying a subcritical bifurcation. These results are consistent with our observations of buckling and wrinkling bifurcations throughout the course of this thesis as well as prior results (see Fig. 9 of [115] for a supercritical bifurcation of a comparable tubular system).

Chapter 8

Temporal stability: $n = 2$

We consider the overdamped time-dependent version of our problem in the limit that the density and moment of inertia of the elastica are sufficiently small relative to the damping coefficient that the acceleration term in Kirchhoff's laws may be disregarded, yielding:

$$\partial_s \vec{F} + (P - \frac{1}{2}K_2 r^2)\hat{n} = \Gamma \frac{\partial \vec{r}}{\partial t} \tag{8.1}$$

$$\partial_s M + \hat{t} \times \vec{F} = 0 \tag{8.2}$$

$$M = \mathcal{B}\kappa \hat{k} . \tag{8.3}$$

Rescaling the system in space and time, via

$$s = \tilde{s}R , \quad \kappa = R^{-1}\tilde{\kappa} , \quad r = R\tilde{r} , \quad P = \frac{\mathcal{B}}{R^3}\tilde{P} , \quad \phi = \tilde{\phi} , \quad F = \frac{B}{R^2}\tilde{F} , \quad t = \frac{\mathcal{B}}{\Gamma R^4}\tilde{t} , \tag{8.4}$$

and dropping tildes, we arrive at the time-dependent form of our problem:

$$0 = \partial_s \phi - \kappa \tag{8.5}$$

$$0 = \partial_s x - \cos(\phi) \tag{8.6}$$

$$0 = \partial_s y - \sin(\phi) \tag{8.7}$$

$$0 = \partial_s^2 \phi + (F_y \cos(\phi) - F_x \sin(\phi)) \tag{8.8}$$

$$\partial_t x = \partial_s F_x - \left(P - \frac{1}{2}\ell^5 r^2 \right) \sin(\phi) \tag{8.9}$$

$$\partial_t y = \partial_s F_y + \left(P - \frac{1}{2}\ell^5 r^2 \right) \cos(\phi) \tag{8.10}$$

We expand around the circle solution with a perturbation of amplitude $\epsilon \ll 1$, given by:

$$\phi = s + \epsilon\phi_v , \quad x = \sin(s) + \epsilon x_v , \quad y = -\cos(s) + \epsilon y_v ,$$

$$F_x = -\left(P - \frac{1}{2}\ell^5 \right)\cos(s) + \epsilon F_{x_v} , \quad F_y = -\left(P - \frac{1}{2}\ell^5 \right)\sin(s) + \epsilon F_{y_v} . \tag{8.11}$$

Collecting terms of $\mathcal{O}(\epsilon)$, the linearized equations are given by:

$$0 = \partial_s x_v + \sin(s)\phi_v \tag{8.12}$$

$$0 = \partial_s y_v - \cos(s)\phi_v \tag{8.13}$$

$$0 = \partial_s^2 \phi_v + \left(p - \frac{1}{2}\ell^5\right)\phi_v + \cos(s)F_{y_v} - \sin(s)F_{x_v} \tag{8.14}$$

$$\partial_t x_v = \partial_s F_{x_v} - \left(p - \frac{1}{2}\ell^5\right)\cos(s)\phi_v + \ell^5\left(\sin^2(s)x_v - \sin(s)\cos(s)y_v\right) \tag{8.15}$$

$$\partial_t y_v = \partial_s F_{y_v} - \left(p - \frac{1}{2}\ell^5\right)\sin(s)\phi_v - \ell^5\left(\sin(s)\cos(s)x_v - \cos^2(s)y_v\right) \tag{8.16}$$

Organized into matrix form, this defines the generalized eigenvalue problem:

$$
\begin{pmatrix} 0 & 0 & 0 & 0 & 0 \\ 0 & 0 & 0 & 0 & 0 \\ 0 & 0 & 0 & 0 & 0 \\ 0 & 1 & 0 & 0 & 0 \\ 0 & 0 & 1 & 0 & 0 \end{pmatrix} \partial_t \begin{pmatrix} \phi_v \\ x_v \\ y_v \\ F_{x_v} \\ F_{y_v} \end{pmatrix} = \begin{pmatrix} \sin(s) & \partial_s & 0 & 0 & 0 \\ -\cos(s) & 0 & \partial_s & 0 & 0 \\ \partial_s^2 + (p - \frac{1}{2}\ell^5) & 0 & 0 & -\sin(s) & \cos(s) \\ -(p - \frac{1}{2}\ell^5)\cos(s) & \ell^5\sin^2(s) & -\ell^5\sin(s)\cos(s) & \partial_s & 0 \\ -(p - \frac{1}{2}\ell^5)\sin(s) & -\ell^5\sin(s)\cos(s) & \ell^5\cos^2(s) & 0 & \partial_s \end{pmatrix} \begin{pmatrix} \phi_v \\ x_v \\ y_v \\ F_{x_v} \\ F_{y_v} \end{pmatrix},
$$
$$\tag{8.17}$$

where the bottom two rows define the time-dependent equations. We discretize Eq. (8.17) with all derivatives constructed with centered finite differences of fourth order accuracy and $N = 2000$. Seeking the eigenfunctions $(\phi_v, x_v, y_v, F_{x_v}, F_{y_v})$ of this system and assuming their time dependence is captured by $\exp(\sigma t)$ such that the system has eigenvalues σ, then the base circle solution is temporally unstable to eigenfunctions with corresponding eigenvalues σ possessing a nonnegative real component. The results are shown for varying ℓ^5 and P in Figs. 8.1,8.2.

Figure 8.1 shows that all eigenvalues fall along the real axis, and as the pressure difference P increases for fixed ℓ^5, the primary mode eigenvalues cross the imaginary axis sequentially. The first primary mode for the circle to become temporally unstable to is $m = 2$, regardless of ℓ^5. However, at higher P, larger m values (i.e. $m = 3, 4$ in this case) are more unstable than $m = 2$. A neutral mode, shown in black, persists across all P and consists of a superposition of $m = 1$ and the mode which most recently crossed the imaginary axis. At $P = 3$, the $m = 2$ mode crosses; at $P = 8$, the $m = 3$ mode crosses; and at $P = 15$, the $m = 4$ mode crosses. The initial instability of the substrate-free system to the $m = 2$ mode and the subsequent shift to higher modes at higher P is consistent with prior results on buckling rings [115, 116].

The overall effect of the inclusion of a substrate is captured in Fig. 8.2 and shows that the pressure difference required for the circle state to become temporally unstable to primary modes $m \geq 2$ increases with ℓ^5, as the eigenvalues of the primary modes shift left along the real axis with increasing ℓ^5. However, as ℓ^5 increases from zero, additional modes separate from the degenerate $m = 1$ neutral mode. These modes (shown in gray) have eigenvalues which are immediately positive for positive ℓ^5. In this way, although the inclusion of a substrate makes the circle state more temporally

89
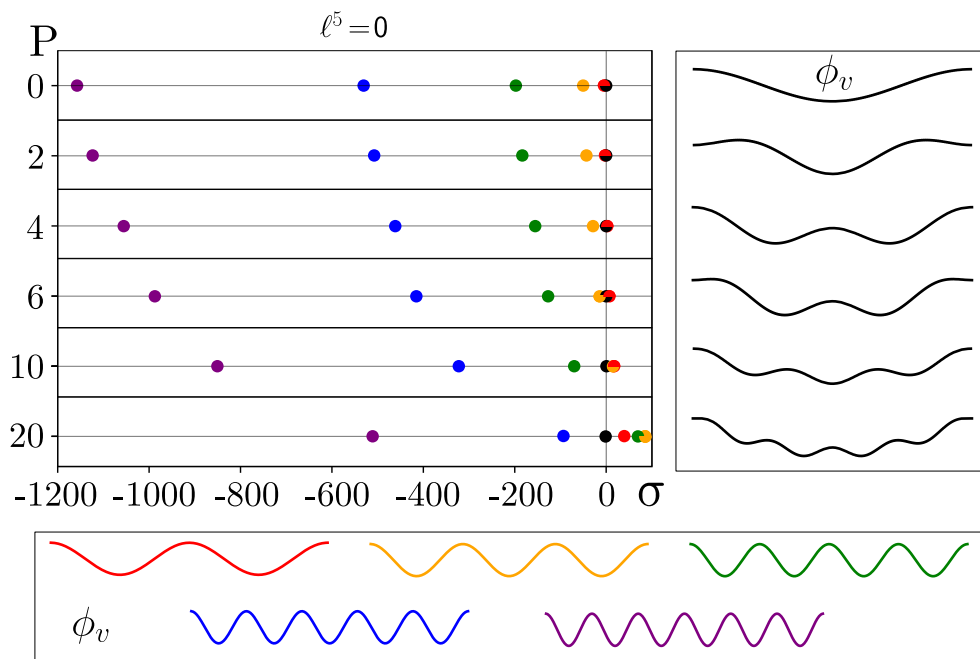
Figure 8.1: A series of panels of eigenvalues σ (left) and correspondingly colored eigenfunctions ϕ_v (bottom, right) for $\ell^5 = 0$ and varying P identifying the temporal stability obtained by solving (8.17). Due to the periodic boundary conditions imposed, modes come in pairs of eigenfunctions of different phase (only one is shown for clarity in each case). All primary modes with $m \geq 2$ are consistent across P and are shown only once (bottom). The neutral mode fixed at $\sigma = 0$ changes with P and is shown separately for each P (right).
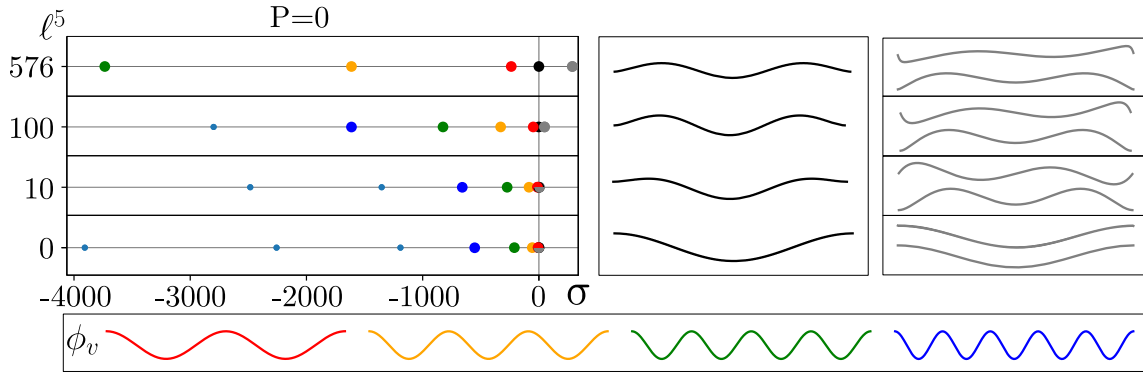
Figure 8.2: A series of panels of eigenvalues σ (left) and correspondingly colored eigenfunctions ϕ_v (bottom, right) for varying ℓ^5 and $P = 0$ identifying the temporal stability obtained by solving (8.17). Due to the periodic boundary conditions imposed, modes come in pairs of eigenfunctions of different phase (only one is shown for clarity in each case). All primary modes with $m \geq 2$ are consistent across P and are shown only once (bottom). The neutral mode fixed at $\sigma = 0$ changes with P and is shown separately for each ℓ^5 in black, with additional modes shown in gray (right).

stable to primary modes for a fixed pressure difference, it makes the circle state temporally unstable to these secondary modes.

Chapter 9

Conclusion

9.1   Summary

In this thesis a unified description has been provided of the wrinkling, buckling, and folding of elastic rings across a family of models characterized by different nonlinear solid and liquid substrate forces. These findings are relevant to applications ranging across biological, fluid, and elastic systems.

In solid-substrate systems, the elastic properties of a springy support either exterior or interior to the membrane dictate the force it exerts. In the fluid supported variant of the problem, situated in a rotating Hele-Shaw cell, where the role of the substrate is played by fluids both exterior and interior to the membrane, the density difference and rotation rate of the fluids dictate the strength of the force. The resulting force is nonlinear in both cases and may be taken to scale with the radius squared (in both cases) or with higher even powers of the radius (in the solid-substrate case). The governing equations for steady state solutions for the membrane shape are therefore the same or similar, and the steady state solutions are therefore also the same or similar between the two systems depending on the choice of forcing.

Within this family of related governing equations, the shape and organization of wrinkling, buckling, and folding solutions in parameter space has been determined in this work, a formerly open question in the Hele-Shaw context of the problem [117]. The model developed predicts the critical pressure for the onset of wrinkling in terms of the mechanical properties of the ring and predicts secondary bifurcations that limit the wrinkling process and initiate folding. This steady state wrinkling is generated through a competition between substrate forces, imposed pressure difference, and membrane bending properties. The limiting behavior of the model is explored, and when the strength of the substrate support is decreased to zero, wrinkling is replaced by buckling, recovering well known prior results [70, 69, 118, 110]. In the opposite limit, i.e. for sufficiently strong substrate support, increasing the applied pressure leads not only to a wrinkle-to-fold transition, but also to mixed states. These fold states mirror the change in the natural length scale and shrink relative to the domain

as the substrate support increases. Further, these folds occur progressively closer to the circle branch in parameter space as ℓ^5 increases.

The case where the interface was taken to be inextensible (the length constrained case) and the case where the interface was permitted to stretch freely (the length unconstrained case) were separately considered in this thesis. In the inextensible limit, a prediction via linear theory for the critical rotation rate as a function of the membrane bending modulus, the difference in fluid densities, and the applied pressure was obtained 5.5. Additionally, a weakly nonlinear analysis was performed about the circle state, yielding the solution and parameter values out to high order in the perturbation amplitude ϵ. Surprisingly, these results remain accurate even for strongly nonlinear solutions. Lastly, numerical continuation was used to organize the solution states into bifurcation diagrams detailing the system response according to the metrics of tension T, maximum curvature κ_{max}, energy E, and compression Δ to the imposed pressure difference P.

The unconstrained or tension-free case is of particular interest. Here, following a linear analysis, the primary finger states were found to be disconnected from the circle states, in contrast to the constrained case. However, as in the constrained case, the finger states exhibit instabilities to both mixed mode states and to fold states, observed via numerical continuation. The latter take the form of symmetric intrusions or protrusions or antisymmetric folds that come in pairs to maintain the overall reflection symmetry imposed by our numerical continuation scheme. In particular, it was demonstrated in this thesis that the first bifurcation of a finger state with wavenumber m generates a fold state with $m-1$ folds of various types. States with the same number of folds but different orientation or shape are created in bifurcations from other finger states with different but smaller wavenumber but these bifurcations are necessarily subsequent bifurcations and not the first. For example, the first bifurcation of the $m=3$ finger states creates a state with two folds, and so does the second bifurcation of the $m=2$ finger state (Fig. 5.11). The folds localize away from these bifurcations as P becomes more and more negative and the interface length grows, resulting in asymptotic degeneracy of all branches with the same number of folds, regardless of type and origin. This is a consequence of the fact that in this regime the folds take up an increasingly small fraction of the overall length L. The unconstrained system thus recapitulates similar behavior found earlier in a floating elastic sheet under compression [21, 23], a system described by an equation similar to Eq. (5.2).

Moreover, the finger states can be either symmetric m-finger states, or break this symmetry, forming an m-finger chiral state of definite handedness. However, these chiral states appear via secondary bifurcations from an already existing finger state, at the same bifurcation as the symmetric folds, and cannot form in a primary bifurcation of the circle state. Together these results help explain the origin and organization of the states reported previously in the unconstrained case with zero pressure difference across the interface [65].

Progressive localization of folds is found to be a consistent feature of both the length constrained and unconstrained systems, as the parameter ℓ (encoding either the substrate stiffness or the rotation rate) increases (cf. Fig. 5.11 for the length unconstrained case and Fig. 5.6 for the length constrained case). This results from the fact that the folds bifurcate subcritically, comparable to the Swift-Hohenberg equation with a bistable nonlinearity [119]. This subcritical bifurcation structure is a staple of buckling and wrinkling systems due to the reflection and translation symmetries discussed in section 7.2.

In addition to constructing and organizing approximate analytical and numerical solutions, the model allowed us to construct exact relations between the primary wrinkled states to the buckled states of the substrate-free case, writing down exact solutions for the family of substrate forcings we considered and parameter mappings between each case. These results suggest an underlying explanation for the striking structural similarities across many wrinkling phenomena as discussed in the introduction, an open question in wrinkling of elastic structures. For systems where the substrate force is dominated by low even powers of its extension, the wrinkle profiles may be expected to be highly similar due to the universality highlighted. This is expected to be highly relevant to systems where the substrate force can be largely recapitulated by the even powers of its Taylor expansion, a potentially broad sector of phenomena.

Lastly, the stability of the $n = 2$ system was considered from an energy-based (global) perspective and with a linear temporal stability (local) analysis. The energies of all symmetric stationary states were calculated by numerical continuation for strongly nonlinear solutions. The wrinkle state with wavelength closest to natural is initially the state with the least energy and is thus globally stable in this sense until a single-fold state bifurcates from it. The energies of asymmetric states were not considered. The linear temporal stability analysis provided a local view of the stability of the unperturbed circular state in a system with first order time dependence. This analysis indicates that the circle state becomes unstable to primary states as P increases, and it does so in sequential order with increasing P regardless of ℓ^5. However, for sufficiently large pressure differences, the circle state may be more unstable to the development of higher wavenumber modes. Further, for nonzero substrate support, the circle state is immediately unstable to secondary states.

9.2   Future work

These results provide a useful basis from which to understand wrinkling of rings and tubes and introduces many new possible directions of study.

Asymptotic secondary states   The exact solutions for the wrinkled states identified in this thesis provide a useful stepping stone for the construction of asymptotic

expressions for the mixed mode and fold states. Using the exact solution for a wrinkled state along a primary branch at the point where a secondary branch of fold solutions bifurcates from it, a weakly nonlinear analysis could be performed about this wrinkled solution. Doing so even to low order would immediately provide a better quantitative understanding of the influence of the parameter ℓ^5 on the profiles of secondary states and their onset, in particular the direction of branching. The asymptotic expressions obtained for wrinkled solutions prompted the discovery of exact analytical solutions for these wrinkled states, and finding analogous exact solutions for the fold states would provide a more complete understanding of the zoo of shapes found (cf. [21, 22]).

Chiral states The nature of the chiral states, which we hypothesize to be localized states of varying degrees of asymmetry, also warrants further study in future. We observed that, in the (T, P) plane, states with equal numbers of intrusions or extrusions coincide exactly regardless of whether they are chiral states or symmetric ones and regardless of whether their folds intrude or extrude. The reason for this significant coincidence is not understood but is intriguing in light of past results for the folding of a planar sheet on the surface of a fluid, where a family of exact solutions was identified which ranged continuously from exact symmetric to exact antisymmetric states [22]. The chiral states also varied in their degree of asymmetry, and it is unclear what determines the degree of asymmetry selected and whether additional states with different degrees of asymmetry ranging from perfectly symmetric to perfectly antisymmetric are available but not selected by numerical continuation. Numerical shooting provided a range of asymmetric solutions, but it was not possible to seek specific states of prescribed asymmetry. This topic remains to be studied, using either a weakly nonlinear analysis centered around the primary states or via numerical continuation with boundary or phase conditions to more precisely search for specific degrees of asymmetry.

Physical realism The model used for this paper is intentionally physically minimal but could be easily modified to become more realistic in several ways. Contact forces could be incorporated to prevent self-intersection of the membrane such that physical solutions could be obtained beyond the first point of self-contact. This has been done for a very similar buckling membrane system in the past, but the influence of nonzero substrate forcing strength on strongly nonlinear self-contacting profiles has not previously been considered [70]. These contact points could feature purely normal forces resulting from a smooth elastica, or friction could be included such that contact forces include a nonzero tangent component.

In addition to including membrane contact forces, the lateral stresses on the membrane by the solid substrate and the extension response within the membrane could be made more realistic. The assumption of a purely radial substrate force for a chiral state is not physically realistic for strongly nonlinear solutions, and more accurate

substrate forces would extend the validity of the results on chiral solutions from the Hele-Shaw system, where it is physically realistic, to the elastic substrate system, where it is not.

In addition to a more physically realistic substrate, the elastica model could be augmented to better capture the stretching and bending behaviors of physical materials. In the Hele-Shaw formulation of the model, the tension limits of a perfectly inextensible and perfectly extensible membrane were considered, while in the solid-substrate model only a perfectly inextensible membrane was considered, but these are both limiting cases of the more physically realistic scenario of a partially extensible membrane in which nonzero tension occurs to resist a change in membrane length but not prevent it entirely. A more physically realistic model could model the membrane as a springy material in which the tension is locally determined by the extension or contraction of an infinitesimal element of the membrane. Further, tangential stretching of the substrate could incur an energetic cost or otherwise be resisted by a more realistic model of the substrate force. Such a model would require a different implementation from the low-dimensional approach taken here and could follow other numerics-based studies of spring-like materials [29, 30]. Additionally, the constitutive equation used for the moment of the elastica assumes the simplest possible dependence on the curvature, but constitutive equations defining a more complex relation between bending moment and curvature have been applied in related systems [63]. Similarly complications could be introduced to our model to make the system more physically realistic.

Time dependence   Lastly, non-steady solutions could be considered by introducing second order time dependence to the model. This could be accomplished by including the acceleration term in Kirchhoff's force equation and computing the time evolution of the resulting PDE as performed in other works [116]. This project is currently in-progress.

9.3   Applications

The approach taken in this thesis explains how the wavelength and amplitude of the wrinkles are selected as a function of parameters in pressure-driven wrinkling systems. This is in turn key to understanding and optimizing many systems

Arterial wrinkling   The self-cleaning wrinkling process in arteries relies on cycles of wrinkling and unwrinkling triggered by the cycle between systolic and diastolic blood pressure ranges as the heart beats [13, 120]. Models of arteries as wrinkling tubes such as this thesis provide a good starting point for understanding the profiles available to the inner-lining of an artery as a function of blood pressure and biological factors which impact arterial stiffness such as age and fitness. The minimal model

considered in this thesis provides a starting point for more refined models that include adhesion of plaque and foulants to the artery walls or a feedback cycle between the artery shape and the blood flow inside it. With a better understanding of the wrinkling and folding profiles available, a natural question that arises is how the bending modulus, the size of the system and the substrate properties may be optimised to maximise in-plane curvature, thereby likely optimising the self-cleaning properties for a given pressure jump, while avoiding the wrinkle-to-fold transition. Specifically, higher curvature states are expected to be more successful at detaching plaque buildups of higher rigidity when they are smaller, a biologically desirable outcome [13]. Further, this wrinkling process is time-dependent and, in arteries, specifically features a time-periodic ramped pressure driven by the heartbeat. Future work could consider temporal simulations with time-varying imposed pressure to better understand the effect of the cyclic parameter variation on the wrinkling cycle in arteries. To study the effect of heartbeats on arterial wrinkling, the range of the pressure cycle could be expanded, contracted, or shifted as a stand-in for varying levels of fitness and health.

Rayleigh-Taylor instability The Hele-Shaw formulation of the problem discussed in this paper provides an experimental testbed for the Rayleigh-Taylor instability on a finite domain under periodic boundary conditions. In the planar Rayleigh-Taylor instability, progressively longer wavelengths enter into the problem in a constantly time-evolving manner and do not saturate, making experimental measurements challenging. Mechanisms that arrest this instability, such as vertical vibration to suppress dripping [121], have been a point of interest for many years. In our formulation, this is achieved via the finite length and nonzero bending modulus of the interface which prohibit these long modes from entering and saturate the instability, allowing for time-independent solutions. Further, the closure requirements force the modes to enter only with discrete wavenumbers, making the system response much more stable with respect to small initial perturbations. Therefore, the Hele-Shaw formulation described in this paper provides a valuable model for experimental study of the Rayleigh-Taylor instability.

Material property measurements Measurement of material elastic properties is important for engineering materials with well-understood system response. For thin elastic membranes, this can be mechanically challenging, but our model may provide a new method for doing so via a variation on the Strain-Induced Elastic Buckling Instability for Mechanical Measurements (SIEBIMM) technique [39]. In this technique, a thin material's elastic modulus is measured by its wrinkling response to prescribed substrate properties and forcing. This could be recast in our system by placing an unknown material at the interface of the Hele-Shaw formulation of the system, quasistatically varying the rotation rate, and observing the critical rotation rate for the onset of instability. This approach provides an easily tuned parameter (the rotation rate) under prescribed pressure and density differences, and would yield an

easily observed instability wavenumber (due to the discrete wavenumber availability), to deduce the unknown bending modulus of a thin elastic material.

Pipe flow defouling   This work could additionally be applied to drip irrigation defouling. In modern water-efficient farming, drip irrigation lines use many small holes along the length of the irrigation line to provide a low-level dripping flow to individual trees or crops. This method is water efficient but often labor intensive to maintain due to the frequent clogging of the holes by aggregated clumps of mud or other foulants which build up inside the tubes out of inflowing silt. The work of this thesis could be applied to design multi-layer irrigation tubes with an interior lining engineered to wrinkle with a specific wavelength and maximum curvature. With a water intake suitably designed to generate periodic fluid pressure variations downstream (via the creation of von Karman vortex streets or similar periodic flow structures), the interior lining could be induced to periodically change its topography and break up foulants before they aggregate to a sufficiently large size to obstruct the outflow holes.

Snap-through instabilities   Euler beam buckling and more general snap-through rapid shape transitions are critical for many biological processes where elastic energy must be stored and rapidly released such as in the beaks of hummingbirds and the leaves of Venus flytraps [122, 123]. Snap-through instabilities are governed by the bifurcation structure of the system, and therefore knowledge of the bifurcation diagrams is crucial for control of the shape transitions of initially unbuckled shapes or for post-buckling transitions under parameter or boundary condition variation. The normal form of a planar Euler beam system and the resulting snap-through instabilities have been detailed by others [124]. However, many biological systems utilize snap-through transitions in non-planar geometries which are not well described by planar beam buckling such as growth instabilities of varicose arteries or radially indented microtubules, and a tubular base geometry may provide a more natural physical model [125, 126]. In the closed elastica system considered in this thesis, a snap-through instability has also been identified. By parametrizing the curve in terms of the local angle rather than the arc-length, composite asymptotic solutions may be constructed using fewer special functions. As a result of this simpler form, a snap-through instability was identified, resulting from a critical angle at which a pair of pinching point forces exceed the tension of the ring [127].

These beam instabilities have been applied in an engineering context for rapid and precisely predetermined actuation in robotics [128]. In all of these systems, optimizing the instability to accomplish a specific transition requires a complete picture of the landscape of metastable states. Application of the bifurcation diagrams described in this thesis are therefore valuable for control and optimization of elastic buckling and rapid shape change in tubular systems.

Chapter 10

Bibliography

[1] M. Wolf and M. Scarbrough. Vascular system, 1996.

[2] M. Lévy. Mémoire sur un nouveau cas intégrable du probleme de l'élastique et l'une des ses applications. *Journal de Mathématiques Pures et Appliquées*, **10**:5–42, 1884.

[3] G. F. Carrier. On the buckling of elastic rings. *Journal of Mathematics and Physics*, **26**(1-4):94–103, 1947.

[4] D. W. Thompson. *On Growth and Form*. Canto. Cambridge University Press, 1992.

[5] E. Cerda and L. Mahadevan. Geometry and physics of wrinkling. *Phys. Rev. Lett.*, **90**:074302, Feb 2003.

[6] C. J. Pournaras, G. Donati, P. D. Brazitikos, A. D. Kapetanios, D. L. Dereklis, and N. Tr. Stangos. Macular Epiretinal Membranes. *Seminars in Ophthalmology*, **15**(2):100–107, January 2000.

[7] K. D. Neff. *Ocular Surface Disease: Cornea, Conjunctiva and Tear Film*. W.B. Saunders, London, January 2013.

[8] Y. Kai. Mechanical regulation of tissues that reproduces wrinkle patterns of gastrointestinal tracts. *Phys. Biol.*, **19**(3):036006, April 2022.

[9] P. Ciarletta, V. Balbi, and E. Kuhl. Pattern selection in growing tubular tissues. *Phys. Rev. Lett.*, **113**:248101, Dec 2014.

[10] M. Heil and J. P. White. Airway closure: surface-tension-driven non-axisymmetric instabilities of liquid-lined elastic rings. *Journal of Fluid Mechanics*, **462**:79–109, July 2002.

[11] A. L. Hazel and M. Heil. Surface-tension-induced buckling of liquid-lined elastic tubes: a model for pulmonary airway closure. *Proc. R. Soc. A*, **461**(2058):1847–1868, June 2005.

[12] D. E. Moulton and A. Goriely. Circumferential buckling instability of a growing cylindrical tube. *Journal of the Mechanics and Physics of Solids*, **59**(3):525–537, March 2011.

[13] L. Pocivavsek, J. Pugar, R. O'Dea, S.-H. Ye, W. Wagner, E. Tzeng, S. Velankar, and E. Cerda. Topography-driven surface renewal. *Nature Phys.*, **14**:948–953, 2018.

[14] S. P. Timoshenko and J. M. Gere. *Theory of Elastic Stability (2nd Edition)*. Dover Publications, 1989.

[15] S. Geisel, E. Secchi, and J. Vermant. The role of surface adhesion on the macroscopic wrinkling of biofilms. *eLife*, **11**:e76027, 2022.

[16] T. J. W. Wagner and D. Vella. Floating carpets and the delamination of elastic sheets. *Phys. Rev. Lett.*, **107**:044301, Jul 2011.

[17] J. M. Kolinski, P. Aussillous, and L. Mahadevan. Shape and motion of a ruck in a rug. *Phys. Rev. Lett.*, **103**:174302, Oct 2009.

[18] J. Huang, M. Juszkiewicz, W. H. de Jeu, E. Cerda, T. Emrick, N. Menon, and T. P. Russell. Capillary Wrinkling of Floating Thin Polymer Films. *Science*, **317**(5838):650–653, August 2007.

[19] B. Roman and J. Bico. Elasto-capillarity: deforming an elastic structure with a liquid droplet. *J. Phys.: Condens. Matter*, **22**:493101, 2010.

[20] H. King, R. D. Schroll, B. Davidovitch, and N. Menon. Elastic sheet on a liquid drop reveals wrinkling and crumpling as distinct symmetry-breaking instabilities. *Proc. Natl. Acad. Sci. USA*, **109**:9716–9720, 2012.

[21] H. Diamant and T. A. Witten. Compression induced folding of a sheet: An integrable system. *Phys. Rev. Lett.*, **107**:164302, 2011.

[22] M. Rivetti. Non-symmetric localized fold of a floating sheet. *Comptes Rendus Mécanique*, **341**:333–338, 2013.

[23] L. Gordillo and E. Knobloch. Fluid-supported elastic sheet under compression: Multifold solutions. *Phys. Rev. E*, **99**:043001, 2019.

[24] L. Pocivavsek, R. Dellsy, A. Kern, S. Johnson, B. Lin, K. Y. C. Lee, and E. Cerda. Stress and fold localization in thin elastic membranes. *Science*, **320**:912–916, 2008.

[25] F. Brau, P. Damman, H. Diamant, and T. A. Witten. Wrinkle to fold transition: influence of the substrate response. *Soft Matter*, **9**:8177, 2013.

[26] N. Stoop, R. Lagrange, D. Terwagne, P. M. Reis, and J. Dunkel. Curvature-induced symmetry breaking determines elastic surface patterns. *Nature Materials*, **14**:337–342, 2015.

[27] H.-H. Dai and Y. Liu. Critical thickness ratio for buckled and wrinkled fruits and vegetables. *EPL*, **108**(4):44003, November 2014.

[28] R. Brown and L. Scriven. The shape and stability of rotating liquid drops. *Proc. R. Soc. A*, **371**(1746):27, June 1980.

[29] T. C. T. Michaels, R. Kusters, A. J. Dear, C. Storm, J. C. Weaver, and L. Mahadevan. Geometric localization in supported elastic struts. *Proc. R. Soc. A.*, **475**(2229):20190370, September 2019.

[30] T. C. T. Michaels, R. Kusters, and L. Mahadevan. Puckering and wrinkling in a growing composite ring. *Proc. R. Soc. A.*, **477**(2248):rspa.2020.0999, April 2021.

[31] G. A. Vliegenthart and G. Gompper. Compression, crumpling and collapse of spherical shells and capsules. *New J. Phys.*, **13**:045020, 2011.

[32] J. Marthelot, P.-T. Brun, F. López Jiménez, and P. M. Reis. Reversible patterning of spherical shells through constrained buckling. *Phys. Rev. Materials*, **1**:025601, 2017.

[33] E. Katifori, S. Alben, and D. R. Nelson. Collapse and folding of pressurized rings in two dimensions. *Phys. Rev. E*, **79**:056604, 2009.

[34] F. Box, O. Kodio, D. O'Kiely, V. Cantelli, A. Goriely, and D. Vella. Dynamic buckling of an elastic ring in a soap film. *Phys. Rev. Lett.*, **124**:198003, 2020.

[35] O. Kodio, A. Goriely, and D. Vella. Dynamic buckling of an inextensible elastic ring: Linear and nonlinear analyses. *Phys. Rev. E*, **101**:053002, 2020.

[36] L. Giomi and L. Mahadevan. Minimal surfaces bounded by elastic lines. *Proc. R. Soc. A*, **468**:1851–1864, 2012.

[37] A. L. Hazel and T. Mullin. On the buckling of elastic rings by external confinement. *Phil. Trans. R. Soc. A*, **375**:20160227, 2017.

[38] R. G. Bettiol and P. Piccione. Instability and bifurcation. *Not. Am. Math. Soc.*, **67**(11):1679–1691, December 2020.

[39] J. Genzer and J. Groenewold. Soft matter with hard skin: From skin wrinkles to templating and material characterization. *Soft Matter*, **2**:310–323, 2006.

[40] S. Hill and F. Inst. P. Channeling in packed columns. *Chemical Engineering Science*, **1**(6):247–253, January 1952.

[41] G. I. Taylor and P. G. Saffman. The penetration of a fluid into a porous medium or Hele-Shaw cell containing a more viscous liquid. *Proc. R. Soc. A*, **245**:312–329, June 1958.

[42] L. Paterson. Radial fingering in a Hele Shaw cell. *Journal of Fluid Mechanics*, **113**:513–529, December 1981.

[43] J. F. Nye, H. W. Lean, and A. N. Wright. Interfaces and falling drops in a Hele-Shaw cell. *Eur. J. Phys.*, **5**(2):73–80, April 1984.

[44] J. D. Chen. Radial viscous fingering patterns in Hele-Shaw cells. *Experiments in Fluids*, **5**(6):363–371, November 1987.

[45] H. Zhao, J. Casademunt, C. Yeung, and J. V. Maher. Perturbing Hele-Shaw flow with a small gap gradient. *Phys. Rev. A*, **45**(4):2455–2460, February 1992.

[46] T. T. Al-Housseiny, P. A. Tsai, and H. A. Stone. Control of interfacial instabilities using flow geometry. *Nature Phys*, **8**(10):747–750, October 2012.

[47] T. T. Al-Housseiny and H. A. Stone. Controlling viscous fingering in tapered Hele-Shaw cells. *Physics of Fluids*, **25**(9):092102, September 2013.

[48] H. Guo, D. C. Hong, and D. A. Kurtze. Surface-tension-driven nonlinear instability in viscous fingers. *Phys. Rev. Lett.*, **69**(10):1520–1523, September 1992.

[49] H. Guo, D. C. Hong, and D. A. Kurtze. Dynamics of viscous fingers and threshold instability. *Phys. Rev. E*, **51**(5):4469–4478, May 1995.

[50] C. K. Chan and N. Y. Liang. Observations of Surfactant Driven Instability in a Hele-Shaw Cell. *Phys. Rev. Lett.*, **79**(22):4381–4384, December 1997.

[51] C. K. Chan. Surfactant wetting layer driven instability in a Hele-Shaw cell. *Physica A: Statistical Mechanics and its Applications*, **288**(1):315–325, December 2000.

[52] R. Krechetnikov and G. M. Homsy. On a new surfactant-driven fingering phenomenon in a Hele-Shaw cell. *J. Fluid Mech.*, **509**:103–124, June 2004.

[53] J. Fernandez, R. Krechetnikov, and G. M. Homsy. Experimental study of a surfactant-driven fingering phenomenon in a Hele-Shaw cell. *J. Fluid Mech.*, **527**:197–216, March 2005.

102

[54] F. M. Rocha and J. A. Miranda. Manipulation of the Saffman-Taylor instability: A curvature-dependent surface tension approach. *Phys. Rev. E*, **87**(1):013017, January 2013.

[55] C. Almarcha, P. M. J. Trevelyan, P. Grosfils, and A. De Wit. Chemically Driven Hydrodynamic Instabilities. *Phys. Rev. Lett.*, **104**(4):044501, January 2010.

[56] M. Mishra, P. M. J. Trevelyan, C. Almarcha, and A. De Wit. Influence of Double Diffusive Effects on Miscible Viscous Fingering. *Phys. Rev. Lett.*, **105**(20):204501, November 2010.

[57] L. A. Riolfo, Y. Nagatsu, S. Iwata, R. Maes, P. M. J. Trevelyan, and A. De Wit. Experimental evidence of reaction-driven miscible viscous fingering. *Phys. Rev. E*, **85**(1):015304, January 2012.

[58] Ll. Carrillo, F. X. Magdaleno, J. Casademunt, and J. Ortín. Experiments in a rotating Hele-Shaw cell. *Phys. Rev. E*, **54**:6260–6267, 1996.

[59] G. D. Carvalho, H. Gadêlha, and J. A. Miranda. Elastic fingering in rotating Hele-Shaw flows. *Phys. Rev. E*, **89**:053019, 2014.

[60] E. Alvarez-Lacalle, J. Ortín, and J. Casademunt. Nonlinear Saffman-Taylor Instability. *Phys. Rev. Lett.*, **92**(5):054501, February 2004.

[61] L. W. Schwartz. Instability and fingering in a rotating Hele-Shaw cell or porous medium. *Phys. Fluids A*, **1**(2):167–169, February 1989.

[62] E. Alvarez-Lacalle, J. Ortín, and J. Casademunt. Low viscosity contrast fingering in a rotating Hele-Shaw cell. *Physics of Fluids*, **16**(4):908–924, April 2004.

[63] A. He, J. Lowengrub, and A. Belmonte. Modeling an Elastic Fingering Instability in a Reactive Hele-Shaw Flow. *SIAM J. Appl. Math.*, **72**(3):842–856, January 2012.

[64] G. D. Carvalho, J. A. Miranda, and H. Gadêlha. Interfacial elastic fingering in Hele-Shaw cells: A weakly nonlinear study. *Phys. Rev. E*, **88**:053006, Nov 2013.

[65] G. D. Carvalho, H. Gadêlha, and J. A. Miranda. Stationary patterns in centrifugally driven interfacial elastic fingering. *Phys. Rev. E*, **90**:063009, 2014.

[66] B. Foster, N. Verschueren, E. Knobloch, and L. Gordillo. Pressure-driven wrinkling of soft inner-lined tubes. *New J. Phys.*, **24**(1):013026, January 2022.

[67] B. Audoly. Localized buckling of a floating elastica. *Phys. Rev. E*, **84**:011605, 2011.

103

[68] O. Oshri, F. Brau, and H. Diamant. Wrinkles and folds in a fluid-supported sheet of finite size. *Phys. Rev. E*, **91**:052408, 2015.

[69] I. Tadjbakhsh and F. Odeh. Equilibrium states of elastic rings. *Journal of Mathematical Analysis and Applications*, **18**(1):59–74, April 1967.

[70] J. E. Flaherty, J. B. Keller, and S. I. Rubinow. Post buckling behavior of elastic tubes and rings with opposite sides in contact. *SIAM J. Appl. Math.*, **23**:446–455, 1972.

[71] J. E. Flaherty and J. B. Keller. Contact problems involving a buckled elastica. *SIAM J. Appl. Math.*, **24**:215–225, 1973.

[72] G. Arreaga, R. Capovilla, C. Chryssomalakos, and J. Guven. Area-constrained planar elastica. *Phys. Rev. E*, **65**:031801, 2002.

[73] P. A. Djondjorov, V. M. Vassilev, and I. M. Mladenov. Analytic description and explicit parametrisation of the equilibrium shapes of elastic rings and tubes under uniform hydrostatic pressure. *International Journal of Mechanical Sciences*, **53**(5):355–364, 2011.

[74] P. Djondjorov, V. Vassilev, M. Hadzhilazova, and I. Mladenov. Thirteenth International Conference on Geometry, Integrability and Quantization, pages 107–114. Avangard Prima, Sofia, 2012.

[75] G. R. Marple, P. K. Purohit, and S. Veerapaneni. Equilibrium shapes of planar elastic membranes. *Phys. Rev. E*, **92**:012405, Jul 2015.

[76] G. Napoli and A. Goriely. A tale of two nested elastic rings. *Proc. R. Soc. A.*, **473**(2204):20170340, August 2017.

[77] P. O. S. Livera and J. A. Miranda. Magnetoelastic pattern formation in field-responsive fluids. *Phys. Rev. Fluids*, **5**:014006, Jan 2020.

[78] W. Harbich, H.J. Deuling, and W. Helfrich. Optical observation of rotationally symmetric lecithin vesicle shapes. *Journal de Physique*, **38**(6):727–729, 1977.

[79] W. Harbich and W. Helfrich. The swelling of egg lecithin in water. *Chemistry and Physics of Lipids*, **36**(1):39–63, November 1984.

[80] F. Box, D. O'Kiely, O. Kodio, M. Inizan, A. A. Castrejón-Pita, and D. Vella. Dynamics of wrinkling in ultrathin elastic sheets. *Proc. Natl. Acad. Sci. USA*, **116**:20875–20880, 2019.

[81] T. Rémond, V. Dolique, F. Vittoz, S. Antony, R. G. Rinaldi, L. Manin, and J.-C. Géminard. Dynamical buckling of a table-tennis ball impinging normally on a rigid target: Experimental and numerical studies. *Phys. Rev. E*, **106**(1):014207, July 2022.

[82] S. K. Veerapaneni, R. Raj, G. Biros, and P. K. Purohit. Analytical and numerical solutions for shapes of quiescent two-dimensional vesicles. *International Journal of Non-Linear Mechanics*, **44**(3):257–262, 2009.

[83] B. Foster, N. Verschueren, E. Knobloch, and L. Gordillo. Universal Wrinkling of Supported Elastic Rings. *Phys. Rev. Lett.*, **129**:164301, Oct 2022.

[84] B. Foster and E. Knobloch. Elastic fingering in a rotating Hele-Shaw cell. *Phys. Rev. E*, **107**(6):065104, June 2023.

[85] S. Wiggins. *Introduction to Applied Nonlinear Dynamical Systems and Chaos*, volume 2 of *Texts in Applied Mathematics*. Springer New York, New York, NY, 1990.

[86] S. Sastry. *Nonlinear Systems*, volume 10 of *Interdisciplinary Applied Mathematics*. Springer, New York, NY, 1999.

[87] S. Chandrasekhar. *Hydrodynamic and Hydromagnetic Stability*. Dover, New York, 1981.

[88] G. Ahlers, S. Grossmann, and D. Lohse. Heat transfer and large scale dynamics in turbulent Rayleigh-Bénard convection. *Rev. Mod. Phys.*, **81**(2):503–537, April 2009.

[89] P. G. Drazin. *Nonlinear Systems*. Cambridge University Press, 1992.

[90] F. C. Hoppensteadt and E. M. Izhikevich. *Weakly connected neural networks*. Springer New York, NY, 1997.

[91] J. H. P. Dawes. Modulated and localized states in a finite domain. *SIAM Journal on Applied Dynamical Systems*, **8**(3):909–930, 2009.

[92] M. Cross and H. Greenside. *Pattern Formation and Dynamics in Nonequilibrium Systems*. Cambridge University Press, 2009.

[93] R. Haberman. *Applied Partial Differential Equations: with Fourier Series and Boundary Value Problems*. Pearson Prentice Hall, Upper Saddle River, N.J, 2004.

[94] E. J. Doedel. Lecture Notes on Numerical Analysis of Nonlinear Equations. In B. Krauskopf, H. M. Osinga, and J. Galán-Vioque, editors, *Numerical Continuation Methods for Dynamical Systems: Path following and boundary value problems*, pages 1–49. Springer Netherlands, Dordrecht, 2007.

[95] Eusebius J Doedel, Alan R Champneys, Fabio Dercole, Thomas Fairgrieve, Yuri Kuznetsov, Bart Oldeman, Randy Paffenroth, Bjorn Sandstede, Xianjun Wang, and Chenghai Zhang. *AUTO-07P: Continuation and Bifurcation Software for Ordinary Differential Equations*, 2012.

[96] W. H. Press, S. A. Teukolsky, W. T. Vetterling, and B. P. Flannery. *Numerical recipes: the art of scientific computing, 3rd Edition*. Cambridge University Press, 2007.

[97] E. Doedel, H. B. Keller, and J. P. Kernevez. Numerical analysis and control of bifurcation problems (I): Bifurcation in finite dimensions. *International Journal of Bifurcation and Chaos*, **1**:493–520, 1991.

[98] J. Stoer and R. Bulirsch. *Introduction to Numerical Analysis*, volume 12 of *Texts in Applied Mathematics*. Springer, New York, NY, 2002.

[99] J. R. Burke. *Localized states in driven dissipative systems*. Ph.D., University of California, Berkeley, United States – California, 2008.

[100] A. Goriely. *The Mathematics and Mechanics of Biological Growth*, volume 45 of *Interdisciplinary Applied Mathematics*. Springer New York, New York, NY, 2017.

[101] G. A. Holzapfel, T. C. Gasser, and R. W. Ogden. A New Constitutive Framework for Arterial Wall Mechanics and a Comparative Study of Material Models. *Journal of Elasticity*, **61**(1):1–48, July 2000.

[102] E. Winkler. *Die Lehre von der Elastizität und Festigkeit*. Dominicus, 1867.

[103] D. A. Dillard, B. Mukherjee, P. Karnal, R. C. Batra, and J. Frechette. A review of Winkler's foundation and its profound influence on adhesion and soft matter applications. *Soft Matter*, **14**(19):3669–3683, 2018.

[104] N. Nguyen, N. Nath, L. Deseri, E. Tzeng, S. S. Velankar, and L. Pocivavsek. Wrinkling instabilities for biologically relevant fiber-reinforced composite materials with a case study of Neo-Hookean/Ogden-Gasser-Holzapfel bilayer. *Biomech. Model. Mechanobiol.*, **19**(6):2375–2395, December 2020.

[105] G. W. Hunt, H. M. Bold, and J. M. T. Thompson. Structural localization phenomena and the dynamical phase-space analogy. *Proc. R. Soc. Lond. A*, **425**:245–267, 1989.

[106] P. Kumar, C. Hajdu, Á. Tóth, and D. Horváth. Flow-driven surface instabilities of tubular chitosan hydrogel. *ChemPhysChem*, **22**:488–492, 2021.

[107] E. J. Doedel, H. B. Keller, and J. P. Kernevez. Numerical analysis and control of bifurcation problems. (II) Bifurcations in infinite dimensions. *International Journal of Bifurcation and Chaos*, **1**:745–772, 1991.

[108] A. Pocheau and B. Roman. Uniqueness of solutions for constrained elastica. *Physica D*, **192**:161–186, 2004.

[109] J. Burke and E. Knobloch. Localized states in the generalized Swift-Hohenberg equation. *Phys. Rev. E*, **73**:056211, 2006.

[110] V. M. Vassilev, P. A. Djondjorov, and I. M. Mladenov. Cylindrical equilibrium shapes of fluid membranes. *J. Phys. A: Math. Theor.*, **41**(43):435201, September 2008.

[111] A. Guckenberger and S. Gekle. Theory and algorithms to compute Helfrich bending forces: a review. *J. Phys.: Condensed Matter*, **29**:203001, 2017.

[112] G. Dangelmayr. Steady-state mode interactions in the presence of O(2) symmetry. *Dynamics and Stability of Systems*, **1**:159–185, 1986.

[113] J. D. Crawford and E. Knobloch. Symmetry and symmetry-breaking bifurcations in fluid dynamics. *Annual Review of Fluid Mechanics*, **23**(1):341–387, 1991.

[114] R. E. Ecke, F. Zhong, and E. Knobloch. Hopf bifurcation with broken reflection symmetry in rotating rayleigh-bénard convection. *EPL*, **19**(3):177, June 1992.

[115] E. Katifori, S. Alben, and D. R. Nelson. Collapse and folding of pressurized rings in two dimensions. *Phys. Rev. E*, **79**(5):056604, May 2009.

[116] O. Kodio, A. Goriely, and D. Vella. Dynamic buckling of an inextensible elastic ring: Linear and nonlinear analyses. *Phys. Rev. E*, **101**(5):053002, May 2020.

[117] G. D. Carvalho, H. Gadêlha, and J. A. Miranda. Stationary patterns in centrifugally driven interfacial elastic fingering. *Phys. Rev. E*, **90**(6):063009, 2014.

[118] G. Arreaga, R. Capovilla, C. Chryssomalakos, and J. Guven. Area-constrained planar elastica. *Phys. Rev. E*, **65**(3):031801, February 2002.

[119] E. Knobloch. Spatial localization in dissipative systems. *Annual Review of Condensed Matter Physics*, **6**:325–359, 2015.

[120] L. Pocivavsek, S.-H. Ye, J. Pugar, E. Tzeng, E. Cerda, S. Velankar, and W. R. Wagner. Active wrinkles to drive self-cleaning: A strategy for anti-thrombotic surfaces for vascular grafts. *Biomaterials*, **192**:226–234, 2019.

[121] J. M. Burgess, A. Juel, W. D. McCormick, J. B. Swift, and H. L. Swinney. Suppression of Dripping from a Ceiling. *Phys. Rev. Lett.*, **86**(7):1203–1206, February 2001.

[122] M. L. Smith, G. M. Yanega, and A. Ruina. Elastic instability model of rapid beak closure in hummingbirds. *Journal of Theoretical Biology*, **282**(1):41–51, August 2011.

[123] Y. Forterre, J. M. Skotheim, J. Dumais, and L. Mahadevan. How the Venus flytrap snaps. *Nature*, **433**(7024):421–425, January 2005.

[124] B. Radisson and E. Kanso. Elastic Snap-Through Instabilities Are Governed by Geometric Symmetries. *Phys. Rev. Lett.*, **130**(23):236102, June 2023.

[125] E. Hannezo, J. Prost, and J.-F. Joanny. Mechanical Instabilities of Biological Tubes. *Phys. Rev. Lett.*, **109**(1):018101, July 2012.

[126] I. A. T. Schaap, C. Carrasco, P. J. de Pablo, F. C. MacKintosh, and C. F. Schmidt. Elastic Response, Buckling, and Instability of Microtubules under Radial Indentation. *Biophysical Journal*, **91**(4):1521–1531, August 2006.

[127] G. Kozyreff, E. Siéfert, B. Radisson, and F. Brau. The θ-formulation of the two-dimensional elastica: buckling and boundary layer theory. *Proc. R. Soc. A*, **479**(2275):20230087, 2023.

[128] X. Zhang, Y. Wang, Z. Tian, M. Samri, K. Moh, R. M. McMeeking, R. Hensel, and E. Arzt. A bioinspired snap-through metastructure for manipulating micro-objects. *Science Advances*, **8**(46):eadd4768, November 2022.

Chapter 11

Appendix A: Weakly nonlinear analysis for $n = 4, 6$

An analogous procedure may be performed for higher order substrate forcing with even powers such as the cases where the exponent of r is 4 or 6. In the cases $n = 4$ and $n = 6$, ϕ is no longer independent of α_4 or α_6, respectively. Similarly, the expressions for T, P contain nonlinear dependence on α_4, α_6.

For $n = 4$, the results are:

$$\phi(s) = s + \epsilon \sin(ms) + \epsilon^2 \frac{\left(12m^6 - 27m^4 + 22\alpha_4\, m^2 + 18m^2 - 10\alpha_4 - 3\right)\sin(2ms)}{24m(m-1)(m+1)(4m^4 - 5m^2 + 2\alpha_4 + 1)} + O(\epsilon^3), \qquad (11.1)$$

$$
\begin{aligned}
T =\ & \frac{2\alpha_4}{(m-1)(m+1)} - m^2 + \frac{3}{2} \\
& - \epsilon^2 \frac{\left(84m^4 - 280m^2 + 100\right)\alpha_4^2 + 6(m-1)(m+1)\left(25m^6 - 92m^4 + 53m^2 - 10\right)\alpha_4}{24(m-1)^3(m+1)^3\left(2\alpha_4 + (m-1)(m+1)(2m-1)(2m+1)\right)} \\
& + \epsilon^2 \frac{9(2m+1)(2m-1)\left(m^2+1\right)(m-1)^4(m+1)^4}{24(m-1)^3(m+1)^3\left(2\alpha_4 + (m-1)(m+1)(2m-1)(2m+1)\right)} \\
& + O(\epsilon^4), \hspace{9cm} (11.2)
\end{aligned}
$$

$$
\begin{aligned}
P =\ & \frac{\left(m^2 - 5\right)\alpha_4}{2(m-1)(m+1)} + (m-1)(m+1) \\
& - \epsilon^2 \frac{4\left(6m^6 - 57m^4 + 100m^2 - 25\right)\alpha_4^2 + 6(m-1)(m+1)\left(8m^8 - 81m^6 + 156m^4 - 69m^2 + 10\right)\alpha_4}{24\left(2(m-1)^3(m+1)^3\alpha_4 + (2m-1)(2m+1)(m-1)^4(m+1)^4\right)} \\
& + \epsilon^2 \frac{9(2m+1)(2m-1)(m-1)^5(m+1)^5}{24\left(2(m-1)^3(m+1)^3\alpha_4 + (2m-1)(2m+1)(m-1)^4(m+1)^4\right)} \\
& + O(\epsilon^4). \hspace{9.5cm} (11.3)
\end{aligned}
$$

The dependence of ϕ and (T, P) on α_4 is nonlinear beyond $\mathcal{O}(\epsilon)$ at the orders computed, consistent with the α_4 dependent translation and mapping obtained in section 6.3.1.

For $n = 6$, the results are:

$$\phi(s) = s + \epsilon \sin(ms) + \epsilon^2 \frac{4m^6 - 9m^4 + 19\alpha_6 m^2 + 6m^2 - 7\alpha_6 - 1}{8m(m-1)(m+1)(4m^4 - 5m^2 + 3\alpha_6 + 1)} \sin(2ms) + O(\epsilon^3), \tag{11.4}$$

$$\begin{aligned}
T = {} & \frac{3}{2} - m^2 + \frac{3\alpha_6}{(m-1)(m+1)} \\
& - \epsilon^2 \frac{3((33m^4 - 154m^2 + 49)\alpha_6^2 + (m-1)(m+1)(41m^6 - 192m^4 + 93m^2 - 14)\alpha_6)}{8(m-1)^3(3\alpha_6 + (m-1)(m+1)(2m-1)(2m+1))(m+1)^3} \\
& + \epsilon^2 \frac{3(2m+1)(2m-1)(m^2+1)(m-1)^4(m+1)^4}{8(m-1)^3(3\alpha_6 + (m-1)(m+1)(2m-1)(2m+1))(m+1)^3} \\
& + O(\epsilon^4),
\end{aligned} \tag{11.5}$$

$$\begin{aligned}
P = {} & (m-1)(m+1) + \frac{(m^2 - 7)\alpha_6}{2(m-1)(m+1)} \\
& - \epsilon^2 \frac{3((6m^6 - 81m^4 + 196m^2 - 49)\alpha_6^2 + (m-1)(m+1)(8m^8 - 113m^6 + 276m^4 - 113m^2 + 14)\alpha_6}{8(3(m-1)^3(m+1)^3\alpha_6 + (2m+1)(2m-1)(m-1)^4(m+1)^4)} \\
& + \epsilon^2 \frac{3(2m+1)(2m-1)(m-1)^5(m+1)^5}{8(3(m-1)^3(m+1)^3\alpha_6 + (2m+1)(2m-1)(m-1)^4(m+1)^4)} \\
& + O(\epsilon^4).
\end{aligned} \tag{11.6}$$

The dependence of ϕ and (T, P) on α_6 is similarly nonlinear beyond $\mathcal{O}(\epsilon)$ at the orders computed, consistent with the α_6 dependent translation and mapping obtained in section 6.3.2.